Wavelength-Modulated Differential Photoacoustic Spectroscopy for Early Detection of Breast Cancer and Hypoxia Monitoring

by

Sung Soo (Sean) Choi

A thesis submitted in conformity with the requirements
for the degree of Master of Applied Science

Graduate Department of Biomaterials and Biomedical Engineering

University of Toronto

Wavelength-Modulated Differential Photoacoustic Spectroscopy for Early Detection of Breast Cancer and Hypoxia Monitoring

Sung Soo (Sean) Choi

Master of Applied Science

Institute of Biomaterials and Biomedical Engineering (IBBME)
University of Toronto

2015

Abstract

In the field of medical diagnostics, biomedical photoacoustic (PA) imaging is a non-invasive hybrid optical-ultrasonic imaging modality. Due to the unique hybrid capability of optical and acoustic imaging, PA imaging has risen to the frontiers of medical diagnostic procedures such as human breast cancer detection. The current study introduces a novel PA spectroscopic modality for ultra-sensitive characterization of functional information for breast cancer imaging. Wavelength-modulated differential Photoacoustic spectroscopy (WM-DPAS) detection has been developed to address angiogenesis and hypoxia monitoring, two well-known benchmarks of breast tumor formation. Based on the WM-DPAS theory, this modality efficiently suppresses background absorptions while amplifying the small PA signal, thereby optically identifying pre-malignant tumors before they are anatomically apparent. The potential of the WM-DPAS to sensitively detect human breast pre-malignancy and quantify the corresponding breast carcinogenesis benchmarks was studied using an *in-vitro* blood circulation system. The experimental results were compared to the developed theoretical formalism.

Acknowledgments

I am using this opportunity to express my deepest appreciation for my supervisor, Professor Andreas Mandelis, for his guidance, invaluable comments and engagement through the learning process of this Master's thesis. He introduced me to Photoacoustics and this dissertation would not have been possible without his genuine supervision and constant support.

I would also like to express my warm thanks to my committee members, Professor Craig A. Simmons and Professor Richard Cobbold. I am sincerely grateful to them for sharing their brilliant advice and truthful views in the course of this study.

I am especially thankful to Dr. Bahman Lashkari for sharing his knowledge and technique in Photoacoustics. He had contributed much to this study from instrumentation to data analysis. In addition, I would like to acknowledge Dr. Xinxin Guo for her friendly comments and encouragement in preparing the theoretical parts of this thesis. She also designed and ran a great part of the computer simulation presented in this thesis.

I am thankful to Dr. Willa Shi and Dr. Alex Vitkin from the Princess Margaret Hospital for tumor cell preparation and knowledge.

I am also thankful to all of my colleagues in the CADIFT, Dr. Alexander Melnikov, Dr. Koneswaran Sivagurunathan, Dr. Jordan Tolev, Dr. Mohammad E. Khosroshahi, Mr. Wei Wang, and Ms. Edem Dovlo, for their kindness and support they have shown during the past two years.

Importantly, despite being mentioned after everyone else, I would like to sincerely thank my loved ones: my parents, brother, and friends. This work was not possible without their unreserved love and the sacrifices they have made on my behalf. I will forever be grateful for your love.

Table of Contents

List of Tables

List of Figures

Chapter 1

Introduction

1.1 Historical background of Photoacoustics

The physics of photoacoustics (PA) involve acoustic wave generation followed by light energy absorption by a material [1-4]. This phenomenon is also commonly referred to as photothermoacoustics (PTA), a term coined to emphasize the involvement of heat in the chain of energy conversion. The idea of PA dates back to 1880; when Alexander Graham Bell first invented the "photophone", a device created based on his observation of the acoustic waves generated from sheets of paper upon the interaction with sunlight [5]. This device used human-voice vibration to modulate the intensity of the transmitted light, which was then converted back to sound waves at the receiving end of crystalline selenium cells [5]. A year after Bell's introduction to PA, several intrigued European scientists such as Tyndall and Rayleigh collectively joined together to pursue a more exhaustive investigation into the PA effect [6]. However, PA had unfortunately started to lose traction within the scientific community due to technical limitations of the time: lack of a sensitive detector, controllable light energy source, and other factors [6]. When the laser was invented in 1960 [7], the principle of PA started to be revisited by many eminent scientists including Kerr and Atwood who reported the application of laser generated PA which measured the low concentrations of air pollutants [8]. Over the past few decades, laser generated PA has been widely applied to numerous applications in fields of chemistry, biology, physics, medicine among others [1-3, 9-12].

1.2 PA in the field of biomedicine: early breast tumor detection

1.2.1 Introduction to the human breast and breast cancer

The adult human female breast is a bilateral organ located in the skin and subcutaneous tissues of the anterior chest (**Figure 1.1**) [13]. A woman's breast is a highly heterogeneous and dynamic

organ whose physiological characteristics change constantly over a lifetime based on one's weight, age, hormone level, habitus, and other factors [13-17]. Cancer developed therein is referred to as breast cancer in general and it is categorized into a few different types based on its location of origin, cell grade and tumor stage [14-23]. Cell grade is usually reported as a number from 1 to 3 based on their shape and division rate [18, 19] and tumor stage is usually expressed as a number from 0 to 4 based on the size and spreadness of the tumor [20-23]. Two most frequent locations where the human breast cancer originates are the breast lobules and ducts [24-26]. The lobules are the milk-producing cells of the breast and the ducts are the tubes where the produced milk travels through. When tumors originating from these locations are pre-malignant, which do not yet have an ability to invade or spread deeper into the breast or the other parts of the body, they are called lobular carcinoma *in situ* (LCIS) or ductal carcinoma *in situ* (DCIS) respectively [13, 24-26]. Since they do not have any invasiveness to surrounding areas, they are likely to be treated rather easily. However, it should be recognized that women with LCIS or DCIS have a higher chance of developing invasive lobular or invasive ductal carcinoma in the future [24, 26]. Once the pre-malignant cells develop into malignant cells, they start metastasizing onto surrounding parts of the body; and the existing treatment tools such as radiation or chemotherapy are less effective, leading to a significant increase in the mortality rate [27-28]. Malignant cells are self-sufficient in growth signals and unresponsive to growth-inhibitory signals or programmed apoptosis [29]. Consequently, they replicate limitlessly and metastasize to other tissues [29].

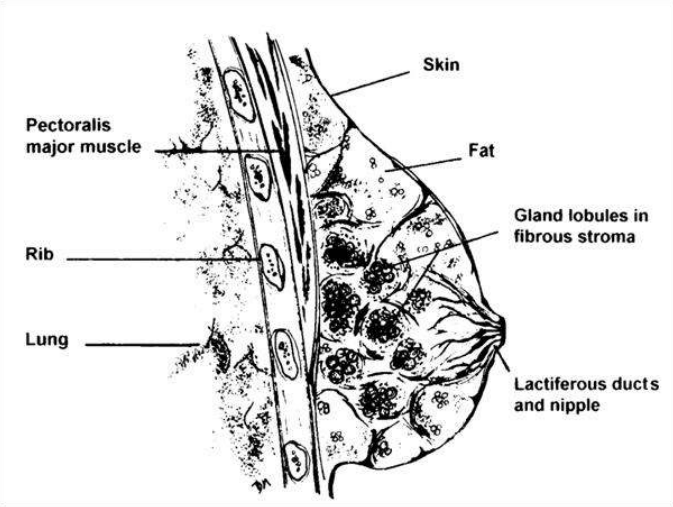

Figure 1.1 Anatomy of a premenopausal healthy adult human female breast [13].

Breast cancer in general is one of the most widespread non-skin malignancies among women within the United States and most European countries [30, 31]. Based on the United States cancer statistics 2014 in **Figure 1.2**, breast cancer accounted for about 29% of all new cancer cases among woman in the United States last year and showed the second highest mortality rate (~15%) after lung/bronchus cancers [31]. As the population ages, the probability of developing breast cancer continuously increases for women and it is well recognized that the risk becomes much greater from the fifth decade on [13].

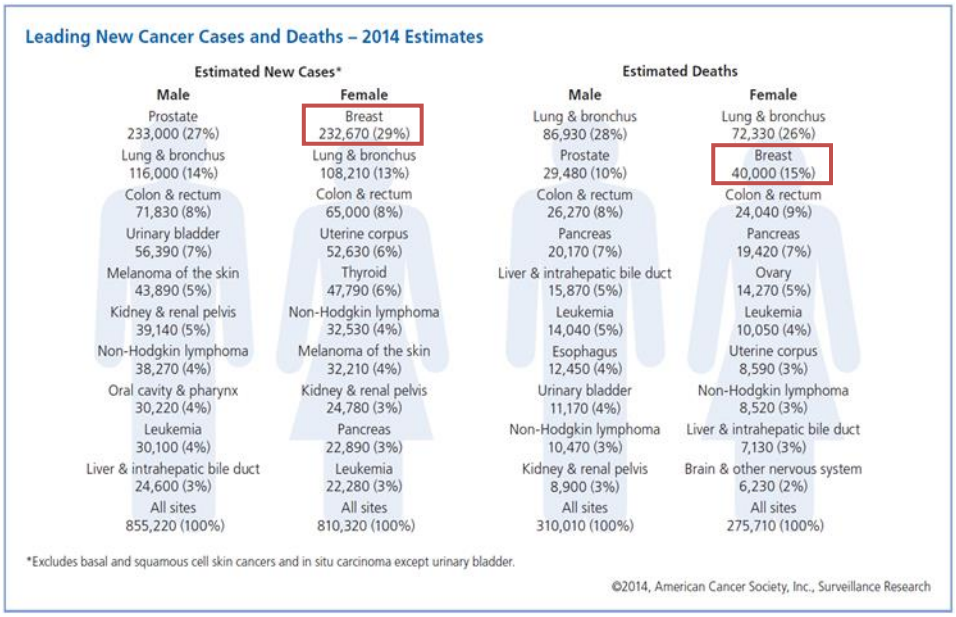

Figure 1.2 United States cancer statistics '14 [31]. It was indicated that breast cancer is prevalent and one of the leading causes of cancer-related deaths in women.

Kondepati *et al* estimated in their study that over 40% of all cancers could be prevented if they were detected and treated early [29]. Therefore, prevention through early detection of breast cancers, before they become fully cancerous and invade the surrounding regions, is becoming essential in reducing mortality, suffering of patients, and improving the quality of life for cancer survivors [32]. Some current detection methodologies for breast cancer include ultrasound imaging (US), magnetic resonance imaging (MRI), diffuse optical tomography (DOT), X-ray mammography, and biopsy [32-34]. Development of such technologies has contributed to statistically decreasing number of deaths by breast cancer over the past few years [32], but it is evident that the specificity and sensitivity of the current screening tools are still limited by many means. These modalities have different screening principles that give them distinctive

advantages and limitations. S**ection 1.2.2** describes the details of the four most common non-invasive imaging tests used to evaluate breast cancer today.

1.2.2 Current breast tumor screening technologies

Since pioneered by Wild and Reid in the 1950s [34], ultrasound (US), or ultrasonagraphy, has slowly become one of the most common screening tools for breast cancer diagnosis. This method utilizes an oscillating sound pressure wave with frequencies from 2-MHz up to 20-MHz to detect the mechanical discrepancy within the human breast tissue [34]. Since the acoustic wave attenuation in tissue is 2 to 3 times weaker than light scattering in tissue, breast US provides better spatial resolution than optical means at depths deeper than 1mm [35]. In addition to the resolution advantage in deep tissue, US is declared by the World Health Organization (WHO) as a safe screening tool for the public without any known short-term or long-term side effects [36]. However, breast US generally produces images with poor contrast as its main contrast source is the mechanical properties of tissues; it may not successfully differentiate the early stage breast tumors which still mechanically resemble surrounding healthy tissues [33, 34]. Furthermore, production and interpretation of the breast US images require personnel with high skill levels and experience [33, 34]. Such dependency on operators may further decrease the specificity and sensitivity of the methodology.

The physics of magnetic resonance imaging (MRI) involves radio-frequency signal generation from the magnetic moment response of water protons (^{1}H nucleus) in the human body to the external magnetic field of the scanner [34, 37-39]. The use of MRI in tumor detection was first reported by Damadian in 1971 [37]. In his study, Damadian studied *in-vitro* relaxation times of tumors and normal tissues with nuclear magnetic resonance [37]. It was only in the 1980s that the earliest *in-vivo* breast MRI was explored [39]. Since then, breast MRI has been widely used in a variety of clinical settings providing volumetric three-dimensional anatomical information along with physiological information with a high sensitivity of 0.9 [34, 40-42]. However, numerous clinical studies of breast MRI demonstrated such a low specificity (about 0.72) that the American Cancer Society refers to MRI only as an adjunct breast screening tool to optical mammography [34, 41, 42]. In addition, its complex operative environment makes the screening much more expensive and time-consuming comparing to other imaging modalities that this tool is not easily accessible by the general population [42]. Its imaging nature of employing a

magnetic field puts further restrictions on patients with ferromagnetic appliances implanted in their bodies.

Diffuse optical tomography (DOT) utilizes non-ionizing near-infrared (NIR) electromagnetic radiation to evaluate the functional information of the tissue of interest [43, 44]. As covered in more detail in **section 1.2.4**, the contrast of breast DOT depends on the optical property discrepancy of tumor tissues with surrounding healthy tissues. The optical properties of biological tissue involve wavelength-dependent absorption and scattering coefficients. Therefore, unlike other screening tools whose contrast source is the mechanical properties, breast DOT produces images with superior contrast even when the tumor region is not anatomically apparent [43, 44]. Moreover, quantifying the functional information such as total hemoglobin concentration (C_{Hb}) or oxygen-saturation level (StO_2), two benchmarks of breast carcinogenesis, allows for determining the instantaneous state of tumors [44, 45]. An intrinsic disadvantage of breast DOT is the strong light scattering within biological tissues which significantly deteriorates spatial resolution at depths greater than 10mm [46].

Among many screening methods, today's golden standard of breast screening is X-ray mammography [30, 34]. Even though the original discovery of X-rays by Röntgen dates back to 1895, Egan reported the application of X-ray mammography for the first time in 1960 [46]. X-ray mammography utilizes low-energy ionizing X-ray radiation to produce structural images of the suspicious area on photographic film [34, 48]. Compared to other screening tools, X-ray mammography achieves high spatial resolution and decent contrast, and was proved, by several large randomized clinical trials, to reduce the mortality rate of breast cancer [32, 49, 50]. Nonetheless, mammography may cause safety concerns among some patients or clinicians as it exploits ionizing X-ray radiation [30]. Furthermore, X-ray mammography may cause unnecessary psychological anxiety and uncertainty among patients due to its relatively high false-positive/negative rates [30, 51]. Breast compression is required during the examination to increase the clearness of the internal structure of the breast and to reduce the amount of X-ray radiation utilized, but this may impose an extra discomfort to patients during the operation.

Different screening modalities that have been developed over the past decades have greatly contributed to detection of breast cancer. However, there are still many limitations with these current technologies for the ideal early diagnosis of breast cancer, as regards invasiveness, safety,

inadequacy of depth penetration, imaging contrast, high cost and other factors. Due to these kinds of problems, the development of an alternative imaging technology for the early detection of breast cancer is necessary.

1.2.3 Biomedical PA

The development of biomedical PA imaging has been catching the attention of many prominent researchers; particularly as an alternative technology for early breast cancer detection [1, 2]. Biomedical PA is a non-invasive breast screening tool that uses non-ionizing NIR (near-infrared) radiation to generate the corresponding acoustic pressure response from a deep light-absorbing target, a tissue chromophore [1, 2]. Generated acoustic waves are detected by an ultrasound transducer with specific center frequency for further analysis. Not only the structural information but also functional information can be obtained by analyzing the laser-induced PA signals [3, 4].

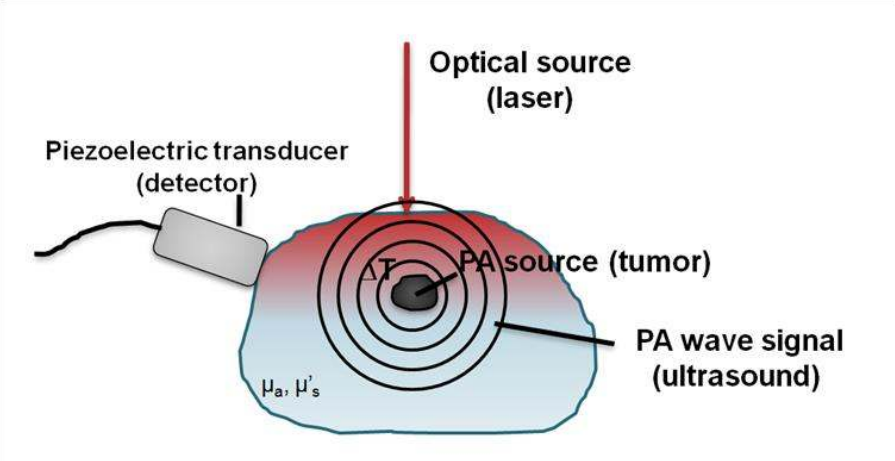

Figure 1.3 Illustration of the PA effect. Here, μ_a and μ_s' are the absorption coefficient and the reduced scattering coefficient of the absorber respectively.

A theory behind PA is the PA effect which was briefly described in **section 1.1**. The PA effect explains when the light-absorbing chromophore absorbs the photon energy of light, it experiences a local temperature rise followed by thermoelastic expansion, which leads to the corresponding pressure transient as an US wave [1]. A schematic diagram that describes the PA effect is shown in **Figure 1.3**. The contrast of PA imaging is based on the optical property difference between the target chromophore and the background; not on the acoustic (or mechanical) property difference as in US imaging. Thus, PA imaging is very unique as it

combines the high contrast of optical imaging with deep subsurface-penetration and high resolution of US imaging [3, 4]. Pure US imaging lacks good contrast while pure optical imaging lacks decent imaging depth (≤ 1mm) and spatial resolution [3, 4].

In general, there are two modes of sample excitation in PA signal generation; time-domain (TD) short (< 10ns) pulsed optical source and frequency-domain (FD) continuous wave (CW) optical source [4, 52]. The former pulsed optical source has high peak power and has been a standard mode of sample excitation in PA over the past years. Its high power improves the overall quality of the obtained PA images in terms of the spatial resolution, and several number of straightforward signal processing algorithms have been developed for subsurface chromophore imaging [53, 54]. The latter CW optical source has high modulation frequency with low peak power. The main mode of sample excitation that our PA system relies on is the latter one. A detailed comparison between these two modes is presented in **section 2.1**.

Understanding different levels of light-sound relationship, such as optical irradiance, photothermal energy conversion, heat conduction, and thermoelastic properties of biological tissue, enables the optical properties of tissue chromophores to be characterized. Regardless of the PA sample excitation mode, both pulsed and CW optical sources can provide anatomical and functional information of subsurface chromophores based on their optical properties.

1.2.4 Contrast sources of breast PA

Cancer tissues are distinctive from their healthy counterparts in their composition and physiology. A number of studies using optical spectroscopic technologies have characterized breast carcinogenesis using their physiological properties as an optical contrast source [13, 29, 30, 43, 44, 55-73].

In healthy human bodies, angiogenesis, the physiological process of forming new blood vessels from existing vasculature, is mainly observed in growth as well as wound healing. However, there is much clinical evidence that angiogenesis plays an important role in both tumor growth and distant metastasis in breast cancer [29, 73-76]. Deng *et al* observed that normal breast tissues adjacent to malignant breast tissues induced angiogenesis twice as frequently as other healthy tissues, suggesting that angiogenesis precedes morphological deformation [56, 74, 75]. Other independent studies showed that tissue with higher vascular density showed increased risk of

developing breast cancer [78]. As new vessels are formed at the irregularly fast rate due to a combination of multiple genetic factors, *the total hemoglobin concentration* (C_{Hb}) *of the local tissue increases*; two to four times higher than surrounding healthy breast tissue [43, 55-59, 65-75]. Cancer-related angiogenesis is unique in that the newly formed blood vessels are thin-walled, dilated, and porous [13]. Consequently, the leaky vessels, along with increased metabolism in tumors, disrupt microcirculation in the tissues, contributing to *a local decrease in oxygen saturation level* (StO_2), hypoxia [29, 30, 44, 59, 62, 68-75]. Therefore, normal and breast tumor tissues can be differentiated by their physiological property differences, especially by two most well-known benchmarks of breast tumor formation; an increase in C_{Hb} and a decrease in StO_2 [29, 30, 43, 44, 56, 59, 62, 68-73].

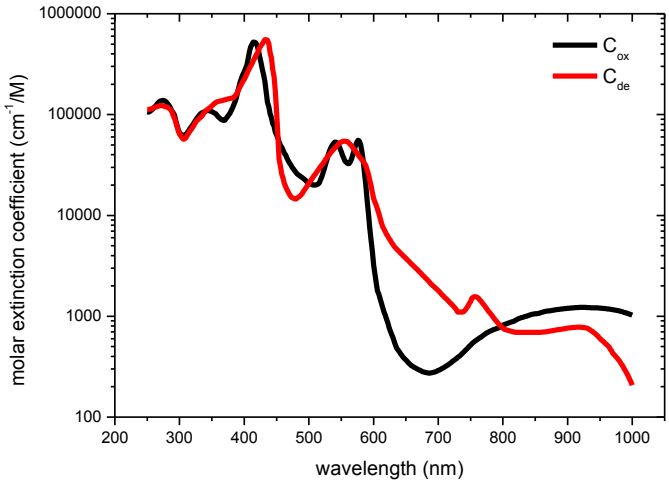

Figure 1.4 Deoxy- and oxy-hemoglobin extinction coefficient spectrum of human; re-plotted from data provided by [79].

These two physiological benchmarks of breast carcinogenesis work as great optical contrast sources when it comes to breast PA probing or imaging. Regarding breast PA, a considerable amount of effort has been made in the NIR spectrum region (700 to 1100-nm), which is known as the optical window in a biological tissue, over the last few decades. NIR spectrum is important for breast tumor detection purposes because NIR radiation is intrinsically sensitive to the important endogenous tissue chromophores such as oxy- and de-oxy hemoglobin [13, 29, 30, 43, 44, 55-73]. These chromophores possess unique absorption spectra in the NIR region as shown in **Figure 1.4**, and therefore can be quantified by optical means, creating functional contrast

between the healthy and tumor tissues. Both C_{Hb} and StO_2 were observed to exhibit monotonic trends during breast carcinogenesis and sensitive monitoring of these parameters may reflect the degree of tumor development [29, 30, 43, 44, 56, 59, 62, 68-72]. The use of NIR radiation is also attractive because it is non-ionizing and is weakly absorbed by tissues, allowing deep penetration of a few centimeters below the breast epithelium [1-4, 60].

1.3 Research Objectives

This thesis is part of the ongoing Frequency-Domain Photoacoustic Radar (FD-PAR) imager development project in the Center for Advanced Diffusion-wave Technologies (CADIFT). The FD-PAR is a new PA-based imaging modality that can be used in breast tumor detection. Recent work on the FD-PAR, introduced in detail in **chapter 2**, proved its competitiveness in the current imaging market for breast tumor diagnosis, but also suggested that it may not possess enough sensitivity especially for early-stage, pre-malignant, tumor detection. As described in **section 1.2**, differentiating tumors while they are still at the pre-malignant stage would increase the effectiveness of the existing treatments, reducing the mortality rate. Therefore, ***the research objective of this thesis is to develop and test a novel differential PA modality, Wavelength-modulated differential photoacoustic spectroscopy* (*WM-DPAS*)*, to further improve the sensitivity and specificity of the existing FD-PAR imager by means of ultra-sensitive imaging of the breast carcinogenesis benchmarks.***

1.4 Outline of Thesis

Chapter 1: A brief introduction to breast cancer and some current imaging modalities used for breast cancer diagnosis is provided. A general introduction to the PA mechanism and its advantages over other existing technologies are also given. The research objective of this thesis is stated at the end of the chapter.

Chapter 2: A detailed review on the FD-PAR development including its current imaging capability is presented. Applications of frequency modulation and matched filter cross-correlation processing of the FD-PAR are especially emphasized in this chapter.

Chapter 3: A developed theoretical formalism of the WM-DPAS system and the corresponding computer simulations are introduced. Throughout the simulation results, the capability of the WM-DPAS system to sensitively detect breast pre-malignancy and quantify carcinogenesis benchmarks is presented as well.

Chapter 4: Instrumentation of the newly-built WM-DPAS laser system and general WM-DPAS experimental set-up are described. Optical behavior of the assembled system is tested under various conditions and confirmed to be satisfactory.

Chapter 5: Single-ended PA behavior is investigated as a preliminary WM-DPAS experiment. An initial *in-vivo* mouse imaging experiment using a single-ended optical source is presented in this chapter as well.

Chapter 6: Experimental PA responses of the WM-DPAS system on an *in-vitro* blood circulating system are presented and compared with the corresponding theoretical predictions. The capability of the WM-DPAS system to sensitively detect pre-malignant breast tumors and quantify carcinogenesis benchmarks is experimentally demonstrated.

Chapter 7: An overall summary of the thesis and possible future directions are provided in the last chapter.

Chapter 2

Review: the Frequency-Domain Photoacoustic Radar (FD-PAR) imager

The Frequency-Domain Photoacoustic Radar (FD-PAR or PAR) imager is a new technology that has been recently developed in the CADIFT at the University of Toronto. The theoretical background and some experimental achievements of the FD-PAR imager are briefly reviewed in this chapter. At the end of the chapter, some of its limitations for which the Wavelength-Modulated Differential Photoacoustic Spectroscopy (WM-DPAS) study have been proposed will be specified.

2.1 Background on FD-PAR development

2.1.1 PA imaging using a continuous wave (CW) mode optical source

As briefly discussed in **section 1.2.3**, biomedical PA imaging is a non-invasive tumor screening method that can differentiate the target based on variation in its optical properties such as wavelength-dependent absorption and scattering coefficients [1-4]. Combining both the optical and acoustic imaging modalities, PA imaging enjoys advantages of each technique: high contrast of optical imaging and deep subsurface-penetration of highly resolved ultrasound imaging [3-4].

A nanosecond (ns) pulsed laser with high peak power has been widely used for subsurface chromophore excitation since its high emission power induces PA responses with large amplitude as expressed by the wave equation for pressure $p(\boldsymbol{r},t)$ in Eq. (1), compromising strong light scattering in tissues to some degree [52-54]. The pulsed laser excitation mode of PA also possesses a number of advanced image processing algorithms that provide a straightforward depth determination in time domain (TD) from time-of-flight measurements with great computational efficiency [2, 52-54].

$$\nabla^2 p(\boldsymbol{r},t) - \frac{1}{{v_a}^2}\frac{\partial^2}{\partial_t{}^2} p(\boldsymbol{r},t) = -\frac{\beta}{C_p}\frac{\partial}{\partial_t} q(\boldsymbol{r},t) \quad (1)$$

$$q(\boldsymbol{r}, t) = \mu_a(r)E(r)\delta(t) \quad (2)$$

where, β is the isobaric volume thermal expansivity, C_p is the specific heat capacity for constant volume, v_a is the speed of sound in the tissue, μ_a is the absorption coefficient of the tissue and $q(\boldsymbol{r},t)$, the source function (Eq. (2)), is the density of optical energy per unit time deposited at position $\boldsymbol{r}$ [52].

Despite all the aforementioned advantages of the pulsed mode PA, a few limitations that make it unsuitable for general biomedical applications should be recognized. First of all, the pulsed lasers do not fit in the clinical environment because they are in general bulky and expensive [80]. They could be 30 to 40 times more expensive (> US$60k) than their CW counterparts (~ US$2k), being about 1100 times larger in volume. Also, its high peak power may raise the safety concern of exceeding the laser MPE (Maximum Permissible Exposure) level [81], possibly damaging the exposed tissues. Moreover, the pulsed lasers have low pulse repetition frequency (PRF < 50-Hz), so the real-time imaging is not likely due to the limited imaging frame rate [82]. Lastly, laser jitter noise and bipolar shape of the pulsed PA transients due to photon-transducer interaction have an adverse effect on the spatial resolution and contrast which can eventually distort the images.

An alternative mode of chromophore excitation in PA imaging utilizes an intensity modulated relatively long (≥ 1ms) CW optical source with low peak power and this is the mode that the recently developed PAR system is based on [52, 83-92]. The development of a portable PA imager for the clinical environment is much more likely with the CW optical sources due to wide availability of compact and low-cost diode sources in the NIR spectrum. Also, the CW optical sources have high PRF (1 to 10-kHz), allowing rapid imaging acquisition, which, in turn, makes dynamic imaging practicable with reduced motion artifacts. Furthermore, its low peak power is advantageous for clinical use compared to its pulsed counterparts as tissues can be exposed to lower photon energy.

2.1.2 Frequency modulation and matched filter cross-correlation processing

Despite the safety advantage CW lasers have over pulsed lasers, the CW-based PA system suffers from particularly weak acoustic pressure wave response. The developed FD-PAR,

however, uses frequency modulation (chirped) waveforms and special frequency-domain signal processing algorithm called matched filter cross-correlation to compensate for its weak PA response by amplifying the signal-to-noise ratio (SNR) by several orders [85-89]. It was previously demonstrated that the FD-PAR modality can compete well with its pulsed counterpart in terms of SNR, resolution, contrast, and imaging depth [87, 90]. Coherent processing with this algorithm is originated from the military radar design, where the detection range is maximized while keeping the resolution and limiting the transmission power [93]. Accordingly, our system is referred to as the *FD-PA radar* that implemented such design to the biomedical field for the first time [52].

The CW modulator can customize the modulation patterns in the megahertz frequency range (0.5 to 10-MHz) based on its need for the subsequent signal processing [86-88]. PA that relies on the intensity modulated CW source has been conventionally limited to spectral applications due to its narrow band-width, and consequently, was deemed unsuitable for the depth detection [94]. However, it was demonstrated that it can be used for depth-resolved imaging if the optical waveform is frequency-swept (chirped) to increase the band-width Δf [86, 87]. The chirp modulation range and chirp duration can be arbitrarily selected based on the sensitivity of the ultrasonic transducer. The modulation chirp signal $f(t)$ can be written as:

$$f(t) = A\cos(\omega_0 t + \pi b t^2) \tag{3}$$

where, A is the amplitude, ω_0 is the starting frequency and b is the frequency sweep rate in Hz/s. This chirp has band-width $\Delta f = b \times T_c = 2f_d$ where T_c is the chirp duration and $f_d = \omega_d/2\pi$ is the frequency deviation from the central frequency [87]. Since the absorption of a modulated optical beam in chromophores generates acoustic waves with the same modulation pattern, when the input optical waveform is chirped modulated, a relatively long chirped acoustic pressure $p(r, \omega)$ is generated from the absorber as described in Eq. (4).

$$\nabla^2 \tilde{p}(\boldsymbol{r}, \omega) + k^2 \tilde{p}(\boldsymbol{r}, \omega) = -\frac{i\omega\beta}{C_p} \tilde{q}(\boldsymbol{r}, \omega) \tag{4}$$

where, ω is the angular modulation frequency, $k = \omega/v_a$ is the acoustic wave number while v_a is the speed of acoustic waves in the tissue, C_p is the specific heat at constant pressure, β is the coefficient of thermal expansion, and q is the spectrum of the spatially distributed photothermal

sources [87, 88]. The cross-correlation processing through the frequency-domain analysis then compresses the received chirped acoustic wave into a single narrow correlation peak with the temporal width ~1/Δ*f*, which determines the axial resolution of the system, at a certain delay time [87, 88]. In this way, the system SNR is increased by several orders of magnitude and the absorber depth can be resolved in a similar way to the pulsed-based PA system [85-92]. The SNR can be further improved by employing and averaging numerous chirps. **Figure 2.1** depicts the data flow in a matched filter cross-correlation algorithm.

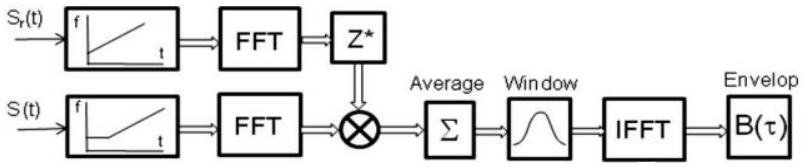

Figure 2.1 A block diagram of the matched filter cross-correlation processing algorithm [52]. $S_r(t)$ is the reference chirp input signal, $S(t)$ is the received acoustic chirp pressure, Z^* represents the complex conjugation, FFT stands for fast Fourier transformation and IFFT stands for inversed fast Fourier transformation [52]. The received PA signal in the time-domain is converted to the frequency-domain through high speed FFT for cross-correlation analysis, then returns back to the time-domain using IFFT [52, 85-92].

Using the frequency-domain representation, the generated cross-correlation signal $B(t-\tau)$ can be expressed as Eq. (5) where *, τ, $S(\omega)$, $S_r(\omega)$ represent complex conjugation, the delay time, the received PA signal and the reference modulation signal respectively [92].

$$B(t-\tau) = \frac{1}{2\pi}\int_{-\infty}^{+\infty} S_r^*(\omega)S(\omega)e^{i\omega(t-\tau)}d\omega \quad (5)$$

The magnitude of the cross-correlation signal reflects the total energy of the signal within the chirp duration which corresponds to the optical absorption of the chromophores. Similarly to the time-of-flight depth determination algorithm of the pulsed PA system, the depth information of the chromophores, d, can be deduced from the obtained delay time τ as $d = \tau$ X v_a. However, the principle difference between the developed FD-PAR and the conventional pulsed-based PA systems must be highlighted. The FD-PAR analyzes the entire record of a relatively long signal to identify the presence of signals with characteristics of the known reference signal while the pulsed-based PA performs a single-point time-resolved measurement [87]. The developed FD-

PAR system therefore allows depth-resolved PA imaging, enjoying the abovementioned benefits of the CW optical source.

2.2 FD-PAR experimental

2.2.1 Materials: PVCP

In previous studies, several different samples had been utilized for the FD-PAR development and optimization. However, in this review, much attention is given to the experiments performed with a non-toxic polyvinyl chloride-plastisol (PVCP) and *in-vivo* human blood vessels [92, 95]. The PVCP was developed as a tissue phantom that simulates human breast tissues in their optical properties. Tissue phantoms have been widely used in the development of numerous biomedical-related technologies because they allow one to test and optimize various parameters of new systems without taking a risk of possibly harming patients [96-98]. Since the optical properties of the PVCP sample can be arbitrarily controlled using a black paint color (BPC; for the absorption coefficient) and a Titanium dioxide (TiO_2) power (for the scattering coefficient), the PVCP can be made as shown in **Figure 2.2** so that it optically mimics the human breast bearing tumors. The details of the PVCP tissue phantom preparation procedure is shown in A**ppendix 1**.

Figure 2.2 Human-breast-simulating PVCP plastisol samples with a few inclusions of higher absorption coefficient. Breast-tumor-simulating inclusion can be made of any kind of material as long as it has higher absorption than the background.

2.2.2 FD-PAR imaging experimental set-up

The FD-PAR system utilized a 1-W power 1064-nm CW laser (IPG Photonics, MA, USA) as an optical source. The optical waveform was sinusoidal chirp modulated by an acousto-optic modulator (AOM; Neos Technologies, FL, USA). The AOM was driven by a function generator NI PXI-5442 (National Instrument, TX, USA) whose modulation was arbitrarily synthesized using a *Labview* software shown in **Figure 2.3**. As the generated beam propagated, two biconcave lenses collimated the beam diameter to 2mm. The imaging target was submerged in water for acoustic coupling with the ultrasonic transducer and its position was tightly controlled by a microscopic stage. The typical chirp modulation used in the experiments had a 1ms duration time and frequency-swept range of 1 to 5-MHz. Usually 100 to 1000 chirps were coherently averaged to increase the SNR of the received PA signals.

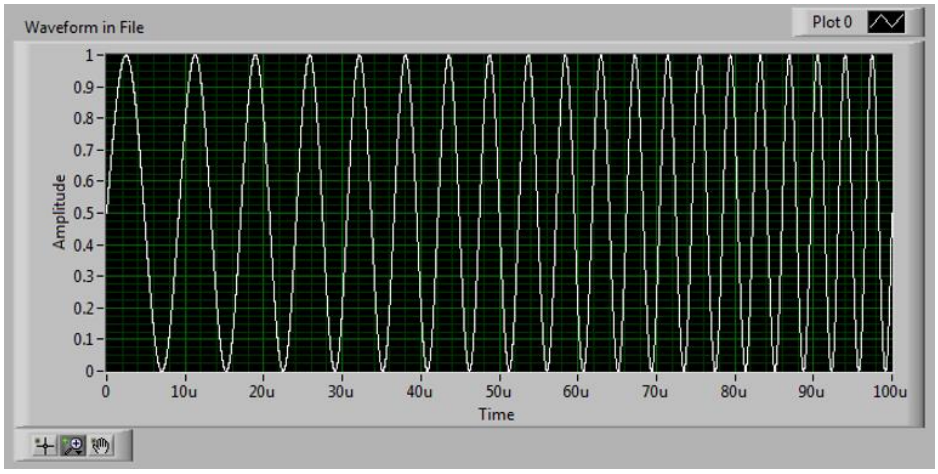

Figure 2.3 Example of sinusoidal chirp modulation driven by the internally developed *Labview* software. Frequency-swept range is 0.1 to 1-MHz and the chirp duration is 1ms.

In the case of using a single element transducer, a 3.5-MHz flat transducer C383 (Olympus Panametrics, CA, USA) with 0.375 inch diameter was mainly used as a receiver. The received PA signal was amplified using a pre-amplifier (5662; Olympus Panametrics, CA, USA) and digitized by an analog-to-digital converter NI PXI-5122 (National Instrument, TX, USA) with a maximum sampling rate of 100-MHz. A trigger was also sent from NI PXI-5442 to NI PXI-5122 for synchronization purposes. In the case of using a phased array transducer, a 64-element 3.5-MHz phased array transducer (GE Parallel Design Inc., AZ, USA) with 80% mean bandwidth at -6 dB and 0.254 mm pitch was mainly used as a receiver. The received signals were processed in

parallel into 8 groups of 8 channels through multiplexer NI PXI-2593 boards (National Instrument, TX, USA). The signals from 8 channels were then amplified through the sets of pre-amplifiers (ZFL-500LN+; Minicircuit, NY, USA) and digitized at an analog-to-digital converter NI PXI-5105 with a maximum sampling rate of 60-MHz. A trigger was also sent from NI PXI-5442 to NI PXI-5105 for synchronization purposes. For data acquisition and processing, numerous *Labview* software have been locally developed in the CADIFT. A schematic diagram of the FD-PAR experimental set-up with the PVCP sample is depicted in **Figure 2.4**.

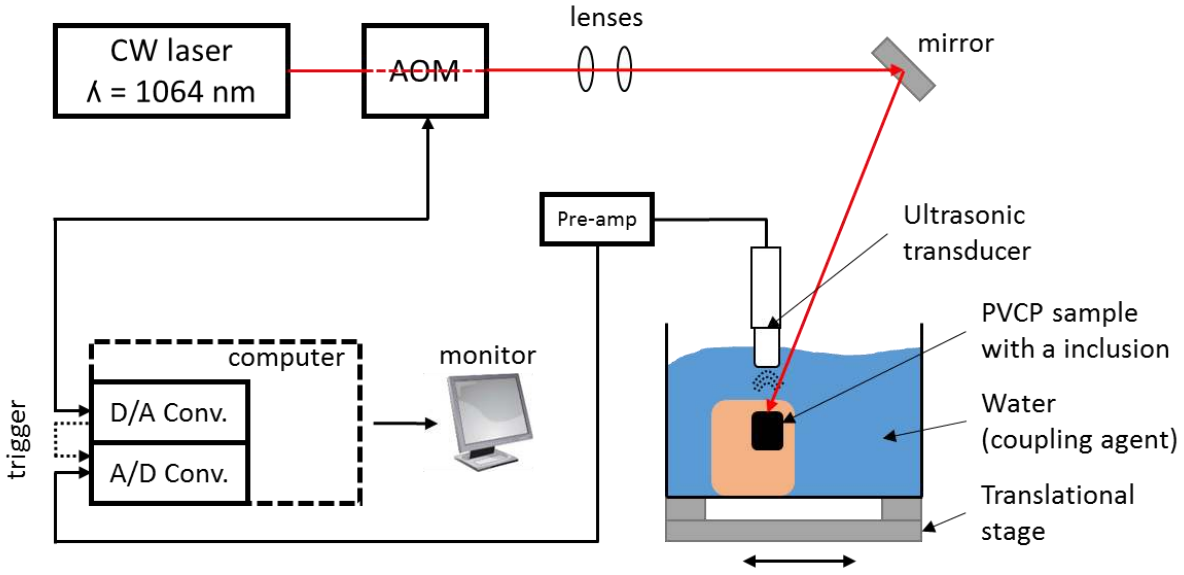

Figure 2.4 Schematic diagram of the FD-PAR experimental set-up

The system set-up for human wrist PA imaging was exactly the same as shown in **Figure 2.4** except for the laser beam size and the imaging target. **Figure 2.5(a)** depicts the schematic diagram of the human wrist PA imaging experiment. The laser beam with a 3mm diameter (0.1 to 1W) hit the sample at a 20^0 angle from Z-axis. As shown in **Figure 2.5(b)**, the coupling water acted as a medium for acoustic wave propagation between the source and the receiver. The water was in contact with the skin through a thin transparent plastic film.

Lastly, to evaluate the imaging potential and capability of the developed FD-PAR imager, a commercial ultrasound imager (SonixTOUCH Ultrasound system; Ultrasonix, BC, CA) was employed for comparison.

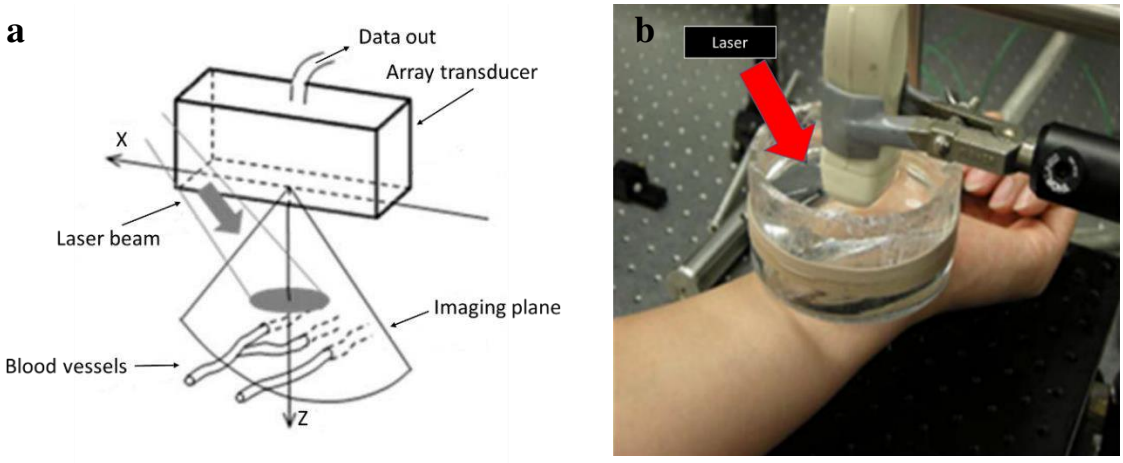

Figure 2.5 **(a)** Schematic diagram and **(b)** actual experimental set-up for the human wrist PA imaging [92].

2.2.3 FD-PAR experimental results and discussion

Before performing any *in-vivo* PAR screening, a clear PVCP phantom with five black threads was prepared as shown in **Figure 2.6**. Each thread, with a diameter of about 0.5mm, was embedded at various depths from 10 up to 32mm below the top surface. During sample preparation, air pocket formation was inevitable as seen in **Figure 2.6**. The effect of these air pockets on imaging is explained in detail below. Such a PVCP model was useful since both the resolution and contrast, two important parameters in imaging technologies, could be simultaneously studied over increasing imaging depth.

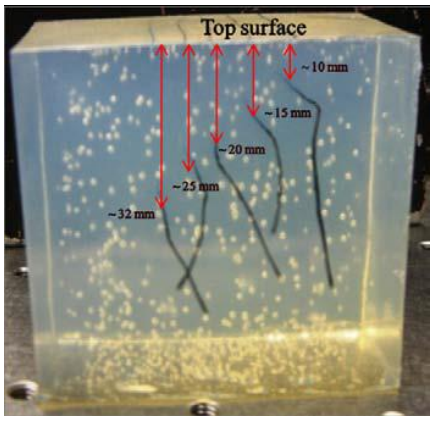

Figure 2.6 The PVCP plastisol sample with five black threads at different depth. A transparent plastisol and black threads optically simulate healthy human breast tissue and tumors respectively [92]. Air pockets have been formed randomly during sample preparation.

The same top surface was scanned by both the PAR and ultrasonic imagers for direct comparison. **Figure 2.7(a)** shows the image taken by the commercial ultrasound imager which used a 128-element 7.2-MHz linear array transducer (Ultrasonix, BC, CA) as a reciever. It was observed that all five targets were successfully imaged with uniform resolution and contrast at various imaging depths. This is because the PVCP model contained no particular acoustic reflector within the body, thus avoiding undesired effects from acoustic attenuation. The only source of noise was the air pockets located near the top surface since they acted as acoustic reflectors. The image taken by the PAR imager of the same sample (**Figure 2.7(b))** showed that a competitive image could be generated over the range of imaging depth studied. At lower imaging depth (< 25mm), the PAR image actually showed superior resolution and contrast to its ultrasound counterparts. As the imaging depth got bigger than 25mm, however, it started to show slightly deteriorated resolution and contrast due to its intrinsic disadvantage of light attenuation. The laser beam broadened and was attenuated to a greater degree as it penetrated deeper into the plastisol which consequently decreased the photon energy density absorbed by the absorbers. In return, a weaker PA signal was generated from the absorbers located deep in the sample. In the PAR image, no air-pockets were detected because they did not absorb photons and therefore did not generate PA signals. Furthermore, the generated PA signals did not interfere with the widespread air pockets because their amplitude was much weaker than its pure ultrasound counterpart [92, 94]. Other artifacts observed in the PAR image could be explained as the electrical noise from the signal processing.

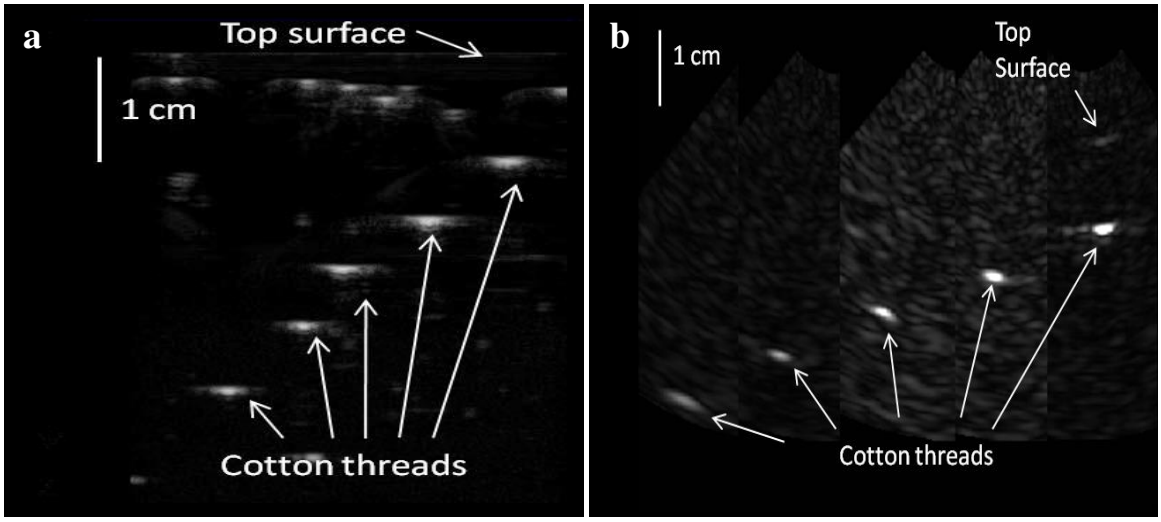

Figure 2.7 **(a)** Pure ultrasound image and **(b)** PAR image of the plastisol sample depicted in **Figure 2.6** [92]. The PAR generated images with superior resolution and contrast at lower depths (< 25mm).

Similar to imaging with the plastisol, the PAR was also employed for *in-vivo* human wrist imaging. As described in **section 1.2**, the targets for this PA imaging were the subcutaneous blood vessels that contain hemoglobin. When the laser power was limited at the safety threshold according to the set MPE [81], the generated FD-PAR correlation signal could successfully construct the image of three subcutaneous blood vessels as shown in **Figure 2.8**.

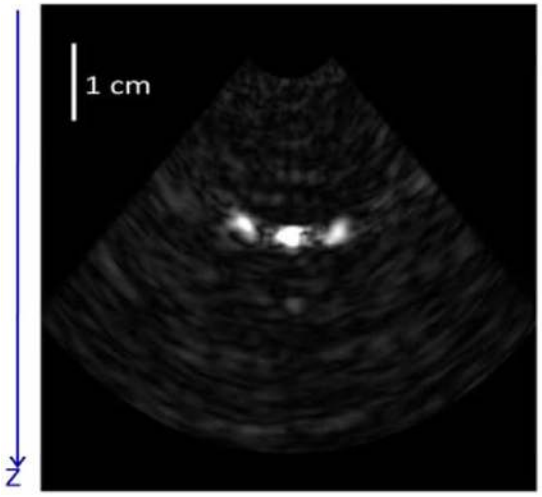

Figure 2.8 PAR image of the human wrist subcutaneous blood vessels [92].

2.3 Conclusions

In this chapter, the development of the FD-PAR imager was briefly reviewed in terms of theoretical formalism and experimental achievements. Encountering a number of disadvantages that the conventional pulsed-based PA system had in the clinical environment, the developed PAR turned out to be a competitive alternative modality for breast cancer detection. The use of a low power and compact CW laser source suggests a portable imaging device that can diagnose a tumor based on their optical properties. Some experimental results with the PVCP plastisol and *in-vivo* human wrist blood vessels were introduced in this chapter, but it must be stated that more thorough studies that prove the potential capability of the PAR system have been continuously conducted and reported in the CADIFT [52, 85-91, 95].

Some studies done in the CADIFT suggest that regardless of the great potential in optical-based tomographic imaging, the FD-PAR alone may not provide enough sensitivity yet for the early-stage breast tumor detection [90]. Breast tumors in their early stage tend to show little or no mechanical discrepancy with the surrounding healthy tissues such that the conventional ultrasound imager shows limited capability in differentiating them. However, it was well-studied that early stage tumors could be possibly differentiated based on their small optical property differences from the surrounding regions; higher total hemoglobin concentration (C_{Hb}) and lower oxy-saturation level (StO_2) [43-45, 55-59, 65-75]. It was, therefore, proposed to further improve the sensitivity and specificity of the existing PAR imager by means of ultrasensitive imaging of blood concentrations and oxy-saturation level located in tumors. Details of the development of a novel differential PAR modality, Wavelength-Modulated Differential Photoacoustic Spectroscopy (WM-DPAS), will be introduced in the following chapters.

Chapter 3

Wavelength-Modulated Differential Photoacoustic Spectroscopy (WM-DPAS): Theory of a High-Sensitivity Methodology for the Detection of Early-Stage Tumors in Tissues

A newly developed theory of the novel WM-DPAS modality addresses angiogenesis and hypoxia monitoring, two hallmarks of human malignancies. As briefly described in **section 1.2.4**, during breast carcinogenesis, excess angiogenesis tends to increase the total hemoglobin concentration (C_{Hb}) *in-situ* while at the same time hypoxia lowers oxy-saturation percentage (StO_2) *in-situ* [65-75, 99]. The optical properties of blood depend sensitively on these physiological and biochemical parameters, and therefore have been the focus of a number of studies that aim to optically detect subsurface malignancy [99-103]. The WM-DPAS modality is expected to detect very small changes in C_{Hb} and StO_2, thereby identifying pre-malignant tumors before they are anatomically apparent. Throughout this chapter, the WM-DPAS theory will be introduced in detail. A corresponding computer simulation with values of the optical parameters taken from normal, pre-malignant, and malignant colon cancer tissue measurement [99] follow.

3.1 WM-DPAS theoretical development

A recent publication from the CADIFT reported the effects of various waveform modulations (sine-wave, square-wave and pulse train) on the SNR of the FD-PAR [89]. When the overall energy content of all three chirps was the same (laser irradiance: 36.8W/cm^2 and chirp duration: 1ms), the correlation peak produced by the square modulation profile turned out to be distinctively higher than those produced by the others due to the differences in the frequency spectrum of the excitation signal involved in PA generation [89]. Furthermore, unlike general imaging modalities, spectroscopic scanning does not require depth information of the targets. Accordingly the development of the WM-DPAS system relied on two out-of-phase single frequency square-wave modulated (50% duty cycle) optical waveforms, instead of chirp

modulations applied for aforementioned depth-resolved FD-PAR imaging. The following sub-chapters describe the WM-DPAS theoretical formalism developed by *Prof.* Andreas Mandelis.

3.1.1 Single-ended PA signal evolution equations

Generation of the PA signal from the tissue chromophores depends on a number of factors at both the optical and absorber ends. Assuming that a single period of a square-wave modulated optical waveform from laser A is absorbed by a semi-infinite subsurface absorber with absorption coefficient, μ_a, at depth L_1 below the surface of the scattering medium (effective attenuation coefficient, μ_{eff}), the generated single-ended PA signal $P_{sA}(t)$ can be expressed as,

$$P_{sA}(t) = C_A\left[H\left(\frac{\tau_0}{2}-t\right) - e^{-\mu_{aA}v_a t} + e^{-\mu_{aA}v_a\left(t-\frac{\tau_0}{2}\right)}H\left(t-\frac{\tau_0}{2}\right)\right]; 0 \le t \le \tau_0 \quad (6)$$

$$C_A = \frac{I_{0A}\beta_a v_a e^{-\mu_{effA}L_1}}{C_p}, H(y) = \begin{cases}1; y > 0\\ 0; y \le 0\end{cases} \quad (6\text{-}1)$$

where C_A and $H(y)$ are a constant factor for laser A's wavelength and the Heaviside step function respectively as described in Eq. (6-1), I_{0A} is the optical intensity of laser A in W/m^2, β_a is the thermoelastic expansion coefficient in K^{-1}, v_a is the speed of sound in the absorber in m/s, C_p is the specific heat of the target in J/kg·K, and τ_0 is the modulation period [105]. In reality, multiple periods of optical waveforms are used, so the accumulated signal contributions from previous periods to the present period must be considered. As the single-ended PA signal from each of the previous periods can be represented as:

$$P_{sA-0}(t) = C_A\left[H\left(\frac{\tau_0}{2}-t\right) - e^{-\mu_{aA}v_a t} + e^{-\mu_{aA}v_a\left(t-\frac{\tau_0}{2}\right)}H\left(t-\frac{\tau_0}{2}\right)\right]; 0 \le t \le \tau_0$$

$$P_{sA-1}(t) = C_A\left[e^{-\mu_{aA}v_a\left(t+\tau_0-\frac{\tau_0}{2}\right)} - e^{-\mu_{aA}v_a(t+\tau_0)}\right]; 0 \le t \le \tau_0$$

$$P_{sA-2}(t) = C_A\left[e^{-\mu_{aA}v_a\left(t+2\tau_0-\frac{\tau_0}{2}\right)} - e^{-\mu_{aA}v_a(t+2\tau_0)}\right]; 0 \le t \le \tau_0$$

⋮ **Nth period**

$$P_{sA-N}(t) = C_A\left[e^{-\mu_{aA}v_a\left(t+\frac{2N-1}{2}\tau_0\right)} - e^{-\mu_{aA}v_a(t+N\tau_0)}\right]; 0 \le t \le \tau_0$$

the total signal from laser A, $P_A(t)$, can be expressed as:

$$P_A(t) = C_A\left\{H\left(\frac{\tau_0}{2} - t\right) + \sum_{N=0}^{\infty}\left[e^{-\mu_{aA}v_a\left(t+\frac{2N-1}{2}\tau_0\right)}H\left(t + \frac{2N-1}{2}\tau_0\right) - e^{-\mu_{aA}v_a(t+N\tau_0)}\right]\right\}; \quad (7)$$

$$0 \le t \le \tau_0$$

The PA signal which is generated when the single period of square-wave modulated waveform from laser B is absorbed by the same sample can be similarly represented as Eq. (6), but a 180° phase shift with respect to the modulation waveform of laser A should be taken into account in a differential system; that is:

$$P_{sB}(t) = C_B\left\{e^{-\mu_{aB}v_a t} - e^{-\mu_{aB}v_a\left(t+\frac{\tau_0}{2}\right)} + \left[1 - e^{-\mu_{aB}v_a\left(t-\frac{\tau_0}{2}\right)}\right]H\left(t - \frac{\tau_0}{2}\right)\right\}; 0 \le t \le \tau_0 \quad (8)$$

$$C_B = \frac{I_{0B}\beta_a v_a e^{-\mu_{effB}L_1}}{c_{pa}}, H(y) = \begin{cases}1; y > 0\\ 0; y \le 0\end{cases} \quad (8\text{-}1)$$

where C_B is a constant factor for laser B's wavelength and I_{0B} is the optical intensity of laser B in W/m^2 [105]. When the contributions of the previous periods are taken into account, the total signal from laser B, $P_B(t)$, is:

$$P_B(t) = C_B\left\{\sum_{N=0}^{\infty}\left[e^{-\mu_{aB}v_a(t+N\tau_0)} - e^{-\mu_{aB}v_a\left(t+\frac{2N+1}{2}\tau_0\right)}\right] + \left[1 - e^{-\mu_{aB}v_a\left(t-\frac{\tau_0}{2}\right)}\right]H\left(t - \frac{\tau_0}{2}\right)\right\}; \quad (9)$$

$$0 \le t \le \tau_0$$

To adjust the phase shift of the PA signal from laser B to an angle other than 180°, a time delay $\pm dt$ can be added to Eq. (9) as:

$$P_B(t) = C_B\left\{\sum_{N=0}^{\infty}\begin{matrix}\left[e^{-\mu_{aB}v_a(t+dt+N\tau_0)} - e^{-\mu_{aB}v_a\left(t+dt+\frac{2N+1}{2}\tau_0\right)}\right]\\ +\left[1 - e^{-\mu_{aB}v_a\left(t+dt-\frac{\tau_0}{2}\right)}\right]H\left(t + dt - \frac{\tau_0}{2}\right)\end{matrix}\right\}; 0 \le t \le \tau_0 \quad (10)$$

When these two PA signals from laser A and laser B superimpose, the differential PA signal equation can be simply derived by adding Eqs. (7) and (9 or 10) as:

$$P_{AB}(t) = P_A(t) + P_B(t) \quad (11)$$

3.1.2 Biomedical applications

The WM-DPAS theory assumes two lasers of different wavelengths (λ_A = 680-nm and λ_B = 808-nm) where two waveforms are square-wave modulated at around 180° phase difference. Two specific wavelengths have been chosen based on the hemoglobin (*Hb*) extinction coefficient spectrum (**Figure 3.1**) that, at 680-nm, molar extinction coefficients of oxy- and deoxy-*Hb* show a noticeable difference while they overlap at 808-nm, the isosbestic point. As such the PA signal is much more sensitive to changes in blood optical parameters at 680-nm while being insensitive at 808-nm. When they are modulated out of phase, existing system noise or any other background absorption would be significantly suppressed from the system, but the difference between the two signals would be amplified. Therefore, differential PA signals from those two wavelengths allow one to detect very small changes in the carcinogenesis benchmarks with great sensitivity. The theoretical development of the WM-DPAS for blood oxygenation and deoxygenation sensing follows.

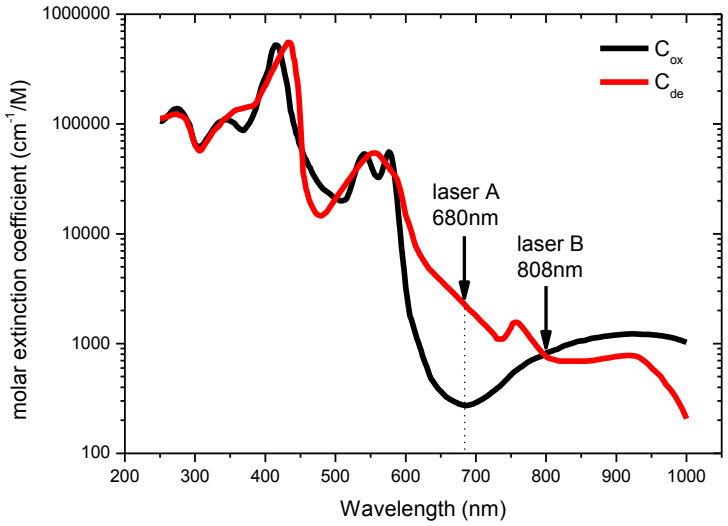

Figure 3.1 *Hb* molar extinction coefficient spectrum of human with arrows indicating two wavelengths of interest for the WM-DPAS system; re-plotted from data obtained by [79].

3.1.2.1 *Hb* detection principles: C_{ox} quantification

The *Hb* absorption coefficient, μ_a, is a function of wavelength and of oxy- and deoxy-*Hb* concentration (C_{ox} and C_{de}). It can be described as:

$$\mu_a(\lambda, C_{ox}, C_{de}) = \ln(10)\, e_{ox}(\lambda) C_{ox} + \ln(10)\, e_{ox}(\lambda) C_{de} \quad (12)$$

where e_{ox} and e_{de} are extinction coefficients of oxy- and deoxy-*Hb* at wavelength λ. Since C_{Hb} is the sum of C_{ox} and C_{de} [55], Eq. (12) can be rearranged as:

$$\mu_a(\lambda, C_{Hb}, C_{ox}) = \ln(10)\, e_{de}(\lambda) C_{Hb} + \ln(10)\, [e_{ox}(\lambda) - e_{de}(\lambda)] C_{ox} \quad (13)$$

Therefore, for the λ_A = 680-nm laser,

$$\mu_{aA}(C_{Hb}, C_{ox}) = \ln(10)\, e_{de}(\lambda_A) C_{Hb} + \ln(10)\, [e_{ox}(\lambda_A) - e_{de}(\lambda_A)] C_{ox} \quad (14)$$

However, for the λ_B = 808-nm laser, the term $[e_{ox}(\lambda_B) - e_{de}(\lambda_B)]$ vanishes since it is at the isosbestic point where $e_{ox}(\lambda_B) = e_{de}(\lambda_B)$ [105, 106]. Therefore, the equation for laser B becomes:

$$\mu_{aB}(C_{Hb}, C_{ox}) = \ln(10)\, e_{de}(\lambda_B) C_{Hb} \quad (15)$$

Since $P_A \propto \mu_{aA}$ and $P_B \propto k\mu_{aB}$ (each of the single-ended PA signal is proportional to the absorption coefficient of the sample at the specific wavelengths), Eqs. (14) and (15) can be combined to represent the differential PA signal as:

$$P_{AB} \propto (\mu_{aA} - k\mu_{aB}) = \ln(10)\, [e_{de}(\lambda_A) - k e_{de}(\lambda_B)] C_{Hb} + \ln(10)\, [e_{ox}(\lambda_A) - e_{de}(\lambda_A)] C_{ox} \quad (16)$$

where P_{AB} is a differential PA signal, μ_{aA} and μ_{aB} are the absorption coefficients of the absorber at specific wavelength *A* (680-nm) and *B* (808-nm) respectively, and *k* is the constant determined by the modulated amplitude ratio *R* (A_A/A_B) and phase difference *dP* ($P_A - P_B$) of the two lasers [105, 106]. In Eq. (16), the constant *k* can be adjusted as $k e_{de}(\lambda_B) = e_{de}(\lambda_A)$ so that the term $[e_{de}(\lambda_A) - k e_{de}(\lambda_B)]$ becomes 0. In this way, the differential PA signal is a sole function of C_{ox} [105, 106].

3.1.2.2 Pre-malignant tumor detection

When it comes to pre-malignant tumor detection, it is important to recognize a clear relationship between *Hb*-dependent biochemical parameters and tissue malignancy. When breast tissues become cancerous, C_{Hb} and StO_2 monotonically increase and decrease, respectively, and those trends can be used for clinical purposes. However, absolute C_{ox} does not show any expected behavior as it may increase or decrease during carcinogenesis depending on a number of conditions. For cancer diagnostic purposes, therefore, we need the differential PA signal as a

function of C_{Hb}. The constant k in Eq. (16) needs to be adjusted so that P_{AB} will be dependent primarily on C_{Hb}, being free of any non-monotonic effects of C_{ox}. The pre-malignant tumor detection modality does not require making a precise quantification of any of *Hb* parameters, but rather the constant k needs to be properly tuned so that the P_{AB} signal fluctuates sensitively only at the suspected pre-malignant tumor site.

3.2 WM-DPAS Simulation

Since a female human breast is a highly heterogeneous and dynamic organ, the biochemical parameter ranges of the breast tissue at different health statuses must be derived by statistics [13, 64, 104]. Even though numerous studies have confirmed the monotonic changes of C_{Hb} and StO_2 over the course of breast carcinogenesis [65-75, 99], unfortunately, there are yet no agreed statistical ranges published for different stages of breast cancer. However, as listed in **Table 3.1**, *Wang et al* could extract C_{Hb} and StO_2 of normal, pre-malignant, and malignant colonic tissues in 27 patients using a diffuse reflectance instrument and algorithms based on the optical diffusion equation [99]. These values have been adopted to lay the foundation of the WM-DPAS system. It should be stated that once reliable statistical values for breast cancer become available, the WM-DPAS can be easily "tuned" based on the new values; by adjusting the constant k in Eq. (16). The novel "tunability" feature of the WM-DPAS will be explained in details in the following sections. The following sub-chapters describe the WM-DPAS computer simulations performed by *Dr.* Xinxin Guo in the CADIFT.

Table 3.1 Statistical C_{Hb} and StO_2 ranges of normal, pre-malignant, and malignant colonic tissues [99].

Tissue state	C_{Hb} (μM)	StO_2 (%)
Normal	93.4±17.1	67.2±3.7
Pre-malignant	136.9±23.8	51.3±7.0
Malignant	153.8±38.6	26.4±6.1

3.2.1 Single-ended PA signal

In section 3.1.1, the theoretical development of single-ended PA signal generation was introduced. In **Figure 3.2**, two PA signal waveforms from laser A and laser B were simulated from Eqs. (7) and (9). In simulation, both lasers were square-wave modulated at 3.5-MHz with 10-previous-period contributions. As described in Eq. (9), the PA signal from laser B was further modulated with a 180° phase shift with respect to the modulation waveform of laser A. When they are superimposed on one another, the two signals would cancel each other, resulting in a steady baseline (zero amplitude and no phase signals). The simulation results of single-ended PA signal generation is compared with the corresponding experimental results in **section 5.1**.

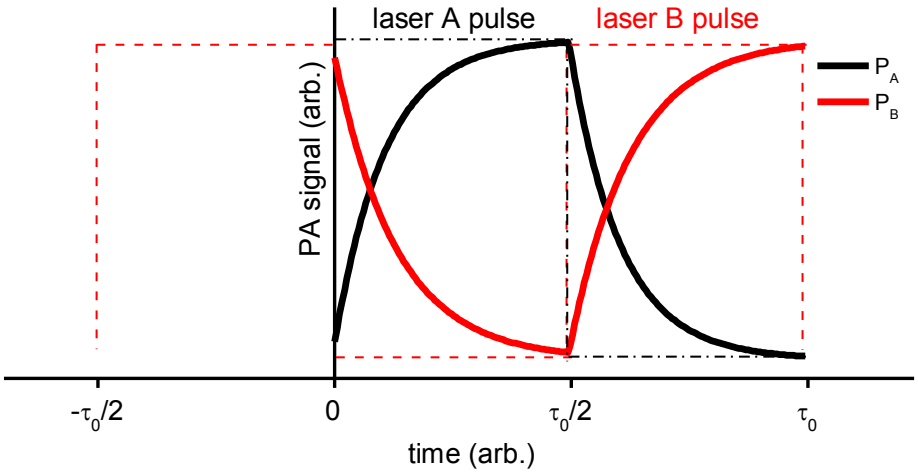

Figure 3.2 Simulation: periods of the PA signal generated from laser A and laser B. The two lasers were square-wave modulated out-of-phase at 3.5-MHz. A contribution of the 10 previous periods was taken into account for the generation of these PA signals.

3.2.2 WM-DPAS pre-malignant detection: quick screening methodology

Using the foregoing theoretical formalism, a corresponding WM-DPAS simulation was carried out with values of optical parameters taken from normal, pre-malignant, and malignant colon cancer tissue measurements [99]. In the simulation, 680-nm and 780-nm lasers were square-wave modulated nearly-out-of-phase (~180°) at 3.5-MHz. Specifically, the 780-nm laser was selected due to its high market availability at the time of simulation, but it should be emphasized that the

system principles are the same because 780-nm is still very close to the isosbestic point of the *Hb* extinction coefficient spectrum. Nevertheless, the 808-nm diode has also become widely available and was exploited for the corresponding WM-DPAS experiments in **chapter 6**.

3.2.2.1 *R* and *dP* effects on differential PA signal

The two parameters (*R* and *dP*), that determine the constant *k* in Eq. (16), were anticipated to have distinct effects on P_{AB}. To study their relationships, P_{AB} of normal, pre-malignant, and malignant colon tissues were simulated over increasing amplitude ratio *R* (A_{680nm}/A_{780nm}) at differently fixed *dP* ($P_{680nm} - P_{780nm}$): 180°, 183° and 186°. Here $R = A_{680nm}/A_{780nm} = 1$ was set for normal tissue as a reference. As shown in **Figure 3.3**, even though both the differential amplitude and phase graphs tend to shift left as the tissue becomes more cancerous, their behaviors were dissimilar in that the differential amplitude showed asymmetrical V-shape behavior while the differential phase showed step-function like behavior over the range of *R* from 0.3 to 1.5. The effects of *dP* on the differential PA amplitude and phase signals were also simulated in **Figures 3.3(a),(c),(e)**, and **3.3(b),(d),(f)** respectively. As *dP* was adjusted away from 180°, the point discontinuity of the differential amplitude signal got more rounded and was raised upward. When the same phase shift was applied to the differential phase signals, they lost their step-function-like behaviour but rather obtained more linearity over the range of *R*.

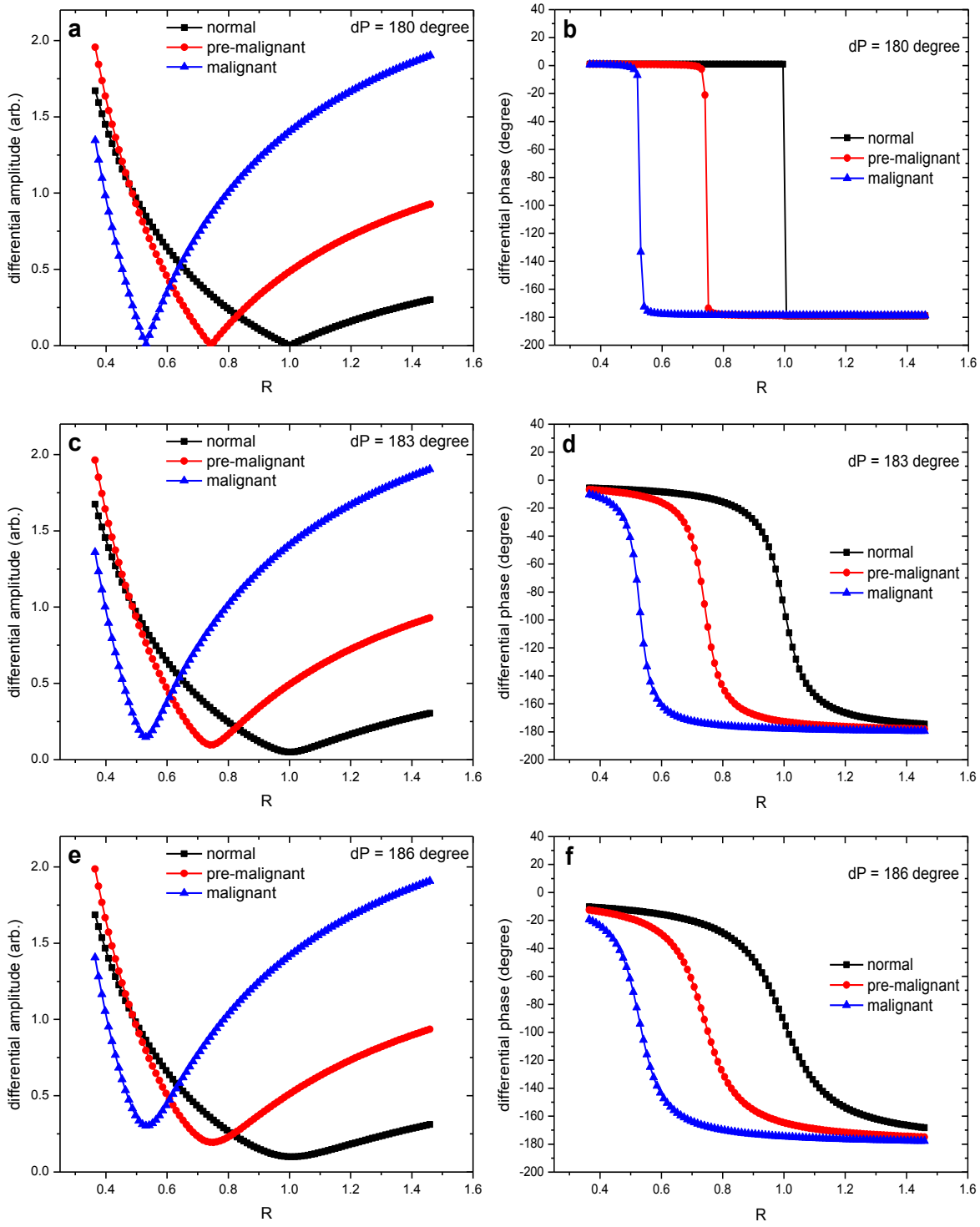

Figure 3.3 Simulation: **(a)** differential amplitude *R*-scan when $dP = 180^{o}$. **(b)** differential phase *R*-scan when $dP = 180^{o}$. **(c)** differential amplitude *R*-scan when $dP = 183^{o}$. **(d)** differential phase *R*-scan when $dP = 183^{o}$. **(e)** differential amplitude *R*-scan when $dP = 186^{o}$. **(f)** differential phase *R*-scan when $dP = 186^{o}$. Here $R = 1$ was set for the normal tissue as a reference.

3.2.2.2 System sensitivity tunability for pre-malignancy detection

Looking at the different behavior of the differential amplitude and differential phase signals, it was assumed that the step-function-like shape of the differential phase signal may provide the WM-DPAS system with the potential to sensitively differentiate pre-malignant tumors from others based on small optical property differences. The idea was to represent the differential phase signal over increasing C_{Hb} or decreasing StO_2 using the major advantage of the WM-DPAS; sensitivity tunability to particular sample parameters leading to signal enhancement at pre-set C_{Hb} or StO_2 ranges.

In **Figure 3.3(b)**, an extreme phase shift over nearly ~180° was observed for the normal, pre-malignant, malignant tissues when the system's R was tuned at near 1.0, 0.76, and 0.54 respectively. In other words, the system R could be arbitrarily tuned to a certain value so that the system sensitivity towards the pre-malignant tissue is maximized. When dP = 180° in **Figure 3.3(b)**, a drastic phase change took place over a small range of R for each sample that, contradictorily, showed rarely any sensitivity to differentiate pre-malignant tumors from the others. However, when dP was adjusted away from 180° as shown in **Figure 3.3(d), (f)**, the system enjoyed an increase in sensitivity while compromising its specificity to some degree. Therefore, when both R and dP are properly tuned, the system sensitivity and specificity for pre-malignant tumor detection could be optimized.

While in **Figure 3.3** only three extreme cases of tissue state were considered for the differential signal simulation, **Figure 3.4** arbitrarily employed more tissue samples with much smaller difference in their C_{Hb} and StO_2. Since it was observed that the system suffers from extremely low sensitivity for pre-malignancy detection at dP = 180°, here, $R = A_{680nm}/A_{780nm} = 1$ and $dP = P_{680nm} - P_{780nm} = 181°$ were set at $C_{ox} = 5\%$ as a reference. The system then could be tuned to R = 1.47 (and dP = 181°) at which the pre-malignant sample exhibited the greatest phase change by nearly 180°. Once the system was tuned to certain R and dP, as shown in **Figure 3.5**, the differential phase signals could be expressed as a function of C_{Hb} and StO_2, two main indicators of breast carcinogenesis. This way the WM-DPAS system would allow very sensitive differential phase measurement when the tissue health state becomes pre-malignant. The WM-DPAS sensitivity to differentiating the pre-malignant tumor is indicated by the dashed square in **Figure**

3.5. Here again, the optical properties of colon cancer were used for the simulation. However, the WM-DPAS tunability suggests that once the statistical agreement is made for the optical properties of breast tissue at different cancer stages, the system's *R* and *dP* can be subjectively tuned so that the maximum differential phase shift occurs between normal and malignant states of breast cancer.

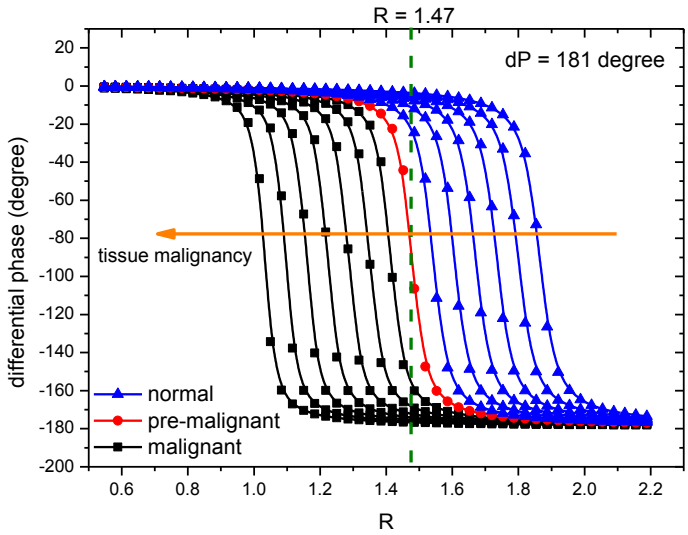

Figure 3.4 Simulation: differential phase *R*-scan of tissues with increasing C_{Hb} (or decreasing StO_2) when $dP = 181°$. The pre-malignant tumor (red circle) shows the drastic phase change at $R = 1.47$ as indicated with the dashed green line.

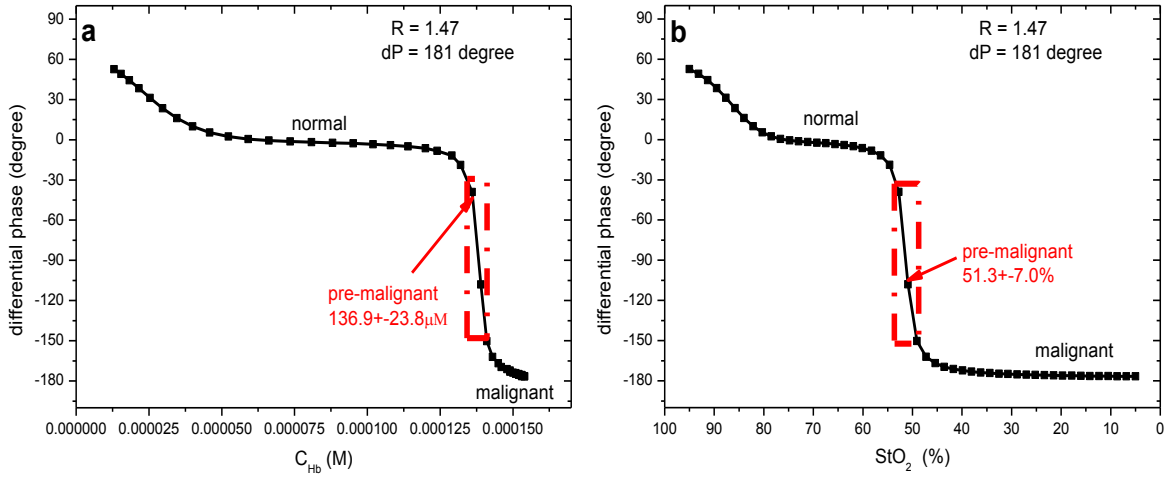

Figure 3.5 Simulation: differential phase over **(a)** C_{Hb} and **(b)** StO_2 when $R = 1.47$ and $dP = 181°$. A drastic phase change happens at C_{Hb} and StO_2 of the pre-malignant tissue when the system is properly tuned. The pre-malignant sample is indicated by the red arrow.

3.2.2.3 Comparison to single-ended PA signal

As shown in **section 3.2.2.2**, the WM-DPAS simulation results proved its capability to differentiate the pre-malignant tumors by the drastic phase change at the specific C_{Hb} and StO_2. For comparison with the differential system, **Figure 3.6** shows the single-ended PA signals as a functions of StO_2 at 680-nm and 780-nm wavelengths. In a single-ended modality, a noticeable phase change does not appear near the pre-malignant tumor. Furthermore, the single-ended modality does not have a tuning capability which makes it unsuitable for pre-malignant cancer detection purposes.

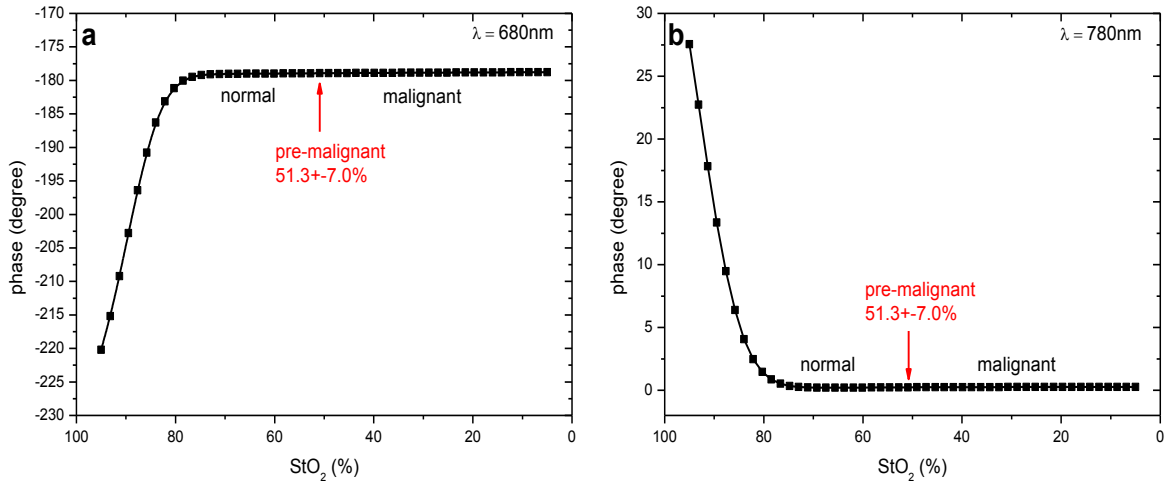

Figure 3.6 Simulation: **(a)** 680-nm and **(b)** 780-nm single-ended PA phase over StO_2. Differently from the tuned WM-DPAS system, single-ended modes could not sensitively differentiate pre-malignancy from others based on the phase shift. The pre-malignant sample is indicated by the red arrow.

3.3 Potential capability of the WM-DPAS system: C_{Hb} and StO_2 quantification

When the system's R and dP are tuned appropriately, a quick pre-malignant tumor screening becomes possible due to the existence of the phase transition. This screening method does not provide precise values of C_{Hb} or StO_2 of the tissue, but rather simply indicates pre-malignancy. In the case of monitoring or quantifying those Hb parameters, the WM-DPAS can also be utilized, provided it is tuned correspondingly.

Even though it is not thoroughly investigated in the presented simulation, possibly at a certain *R* and *dP* combination, a linear relationship is expected between the differential amplitude (or phase) signals and either of the two carcinogenesis benchmarks; C_{Hb} and StO_2. Well-developed linearity between the differential signals and those *Hb* parameters will allow one to accurately quantify C_{Hb} or StO_2 of the tissue at any stage, providing clinicians or patients with extra invaluable information about the tumor status. In other words, the WM-DPAS system has great capability to utilize two complementary channels to meet different clinical needs; either sensitive pre-malignancy screening or *Hb* biochemical parameter monitoring/quantification. Such a potential capability of the WM-DPAS system has been investigated throughout experiments and will be presented in **chapter 6**.

3.4 Conclusions

As a means of enhancing the sensitivity and specificity of the existing FD-PAR system, the development of the novel WM-DPAS system has been suggested. The theoretical formalism for both single-ended and differential PA signal generation was introduced and corresponding simulation results were presented. Throughout the chapter, sensitivity tunability of the WM-DPAS was emphasized that this modality could successfully differentiate pre-malignant tumors based on their small optical property differences from the surrounding healthy tissues. The potential use of the WM-DPAS for quantitative measurements was also briefly established.

Chapter 4

WM-DPAS system preparation: Instrumentation, system set-up and system testing

Upon the development of the WM-DPAS theoretical formalism, a corresponding computer simulation has confirmed the potential capability of the system for early breast cancer detection. This chapter will be dedicated to introducing the development of the initial WM-DPAS system from the perspective of instrumentation assembly, system set-up and testing. The same system was used for both the single-ended PA and WM-DPAS experiments that are covered in more detail in **Chapter 5 and 6**, respectively.

4.1 Instrumentation

4.1.1 Laser box assembly

Two laser diodes with λ_A = 680-nm (LDX-3230-680) and λ_B = 808-nm (LDX-3415-808; RPMC, MO, USA) have been purchased and integrated with a customized laser driver (VFM5-25; MESSTEC, BY, DE) on a single aluminum heat sink. The 680-nm and 808-nm diode lasers have maximum optical power (out-of-fiber) of ~1.4W and ~3.2W respectively. From the manufacturer's test result in **Figure 4.1**, the laser driver showed a rise time of 18.92ns which is sufficient for sine-wave modulation up to nearly 25-MHz. Since the WM-DPAS system requires square-wave modulation in the range of 0.3~5.0-MHz, this driver was acceptable for our needs.

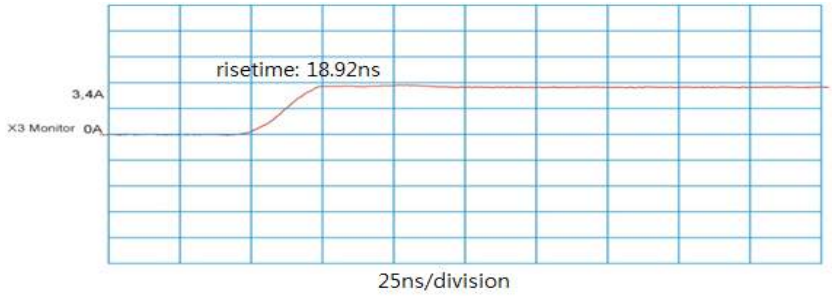

Figure 4.1 The driver test result from MESSTEC. The shown rise time of 18.92ns is sufficient for modulation up to nearly 25-MHz (much higher than the required 5-MHz modulation).

All the components were assembled into a complete laser box in the CADIFT. A few electrical switches were installed for safe laser switch on-off and an extra fan was mounted to enhance air flow inside the box. As shown in **Figure 4.2**, the WM-DPAS laser system could be built in a reasonably compact size (275 X 170 X 100mm) at an approximate cost of CAD$6k. Compared to the conventional pulsed-laser system in the CADIFT (Continuum Nd:YAG; ~US$60k, 775 X 178 X 190mm), this small and cost-effective system is undoubtedly advantageous for the clinical environment.

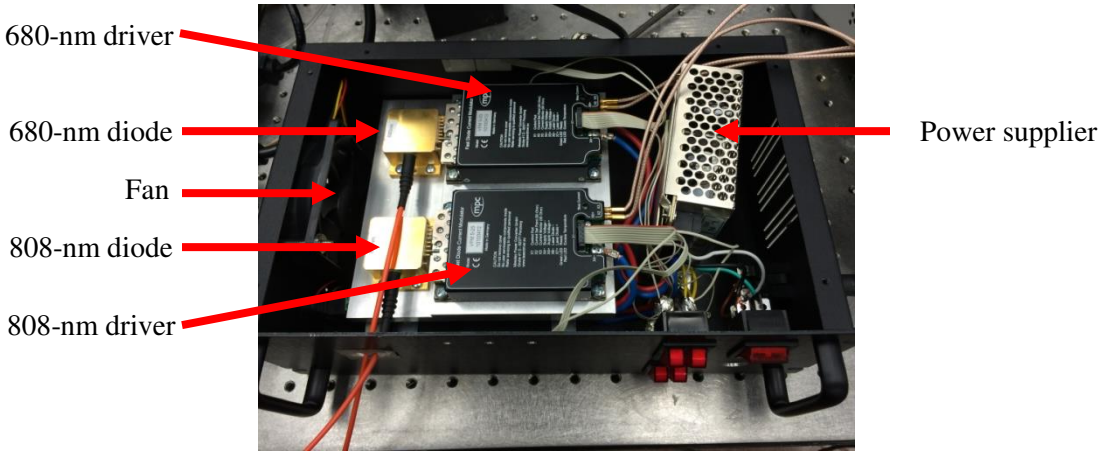

Figure 4.2 Assembled WM-DPAS laser system. Both 680-nm and 808-nm RPMC lasers are finely modulated by the identical MESSTEC drivers.

4.1.2 Laser box accessories

In the WM-DPAS system, the amplitude and phase of two optical waveforms need to be finely modulated. Using two conventional single-channel signal modulators could have been an option, but it could not guarantee fixed constant phase difference (*dP*) between two waveforms which is necessary for reliable WM-DPAS measurements. For that reason, a dual-channel function generator (33522B; Agilent, CA, USA) was employed for the system with which the system *dP* could be fixed at an arbitrary value during the experiments with less than ±0.01° deviation.

To ensure laser optical power stability, the diode temperature needs be finely controlled. Unfortunately, the heat sink and the installed fan were not enough to stabilize the diode temperature over time that the diode performance in terms of optical power stability did not reach the expectation. Thereby, a TEC controller (Arroyo 5305; Arroyo Instruments, CA, USA)

was added to the system to fix the system temperature over time. Since the two RPMC diodes already had TECs mounted in the package, the addition of the TEC controller could fix the diode temperature arbitrarily at 20°C (with less than ±0.01°C deviation) during the experiments. The optical stability of the diode with and without the TEC controller is compared in the following **section 4.3.2**.

4.2 WM-DPAS experimental set-up

The WM-DPAS system requires the two laser beams of different wavelengths to be directed to the same spot on the sample. As depicted in **Figure 4.3** on the next page, the system involves two protected silver mirrors with 25.4mm diameter (PF10-03-P01; Thorlabs, NJ, USA) for beam coincidence. Each mirror provided fine movement in all (X, Y and Z) directions. Other than mirrors, a single-element 1.0-MHz focused ultrasonic transducer (V314; Olympus Panametrics, CA, USA) and sample holder had been installed that also had freedom of movement in all directions, allowing the fine alignment of the system in general. A convex lens was also placed in front of the 808-nm diode beam to ensure an identical beam size of the two lasers. In **Figure 4.3**, the blood chamber (CFCAS0004; IBI Scientific, IA, USA) is shown as an example of the optical target, but in the actual experimental set-up, it can be easily replaced by other samples whenever necessary. Samples were placed at the focal distance of the transducer (1.9 inch).

The two laser beams that were collimated into 0.8mm diameters by the same collimators (F230SMA-B; Thorlabs, NJ, USA) were directed to the identical location on the sample with about a 20^0 incidence angle via the aforementioned mirrors. This angle was observed to maximize the system SNR from the experiment described in **Appendix 2**. As light traveled to the target, the beam size of two lasers were dilated to about ~15mm. In this set-up, any stray reflection from the sample surface may leak a small portion of either beam into the other fiber tip which may eventually damage the diodes. Fortunately, the reflected beams were highly scattered through the course of several reflections, so the beam power was quite negligible (~0.1mW) at the other fiber end. However, to ensure diode safety, two filters (FES0750 and FEL0750; Thorlabs, NJ, USA) were installed right in front of each collimator. Filter FES0750, installed in front of the 680-nm diode, only allows 680-nm light to be transmitted while completely blocking

808-nm light; thereby protecting the 680-nm diode. Similarly, filter FEL0750, installed in front of the 808-nm diode, blocks 680-nm light completely and protects the 808-nm diode. A continuously variable neutral density filter with OD 0.04 – 1 (64-381; Edmund, NJ, USA) was also used to sweep the 808-nm laser beam for the differential R-scan. Using the full OD range, the system R (A_{680nm}/A_{808nm}) could be varied from ~0.2 to ~1.8. As depicted in **Figure 4.3**, a transducer head and the absorber (the blood chamber in this case) were submerged in de-ionized water for acoustic coupling. ND filter and the two mirrors were also placed in the water to minimize the heat accumulation on the optics. The received PA signal was amplified 40-dB by the pre-amplifier (5662; Olympus Panametrics, CA, USA) and analyzed by either the locally-programmed *Labview* software lock-in amplifier or the hardware lock-in amplifier (SR822; Stanford Research System, CA, USA).

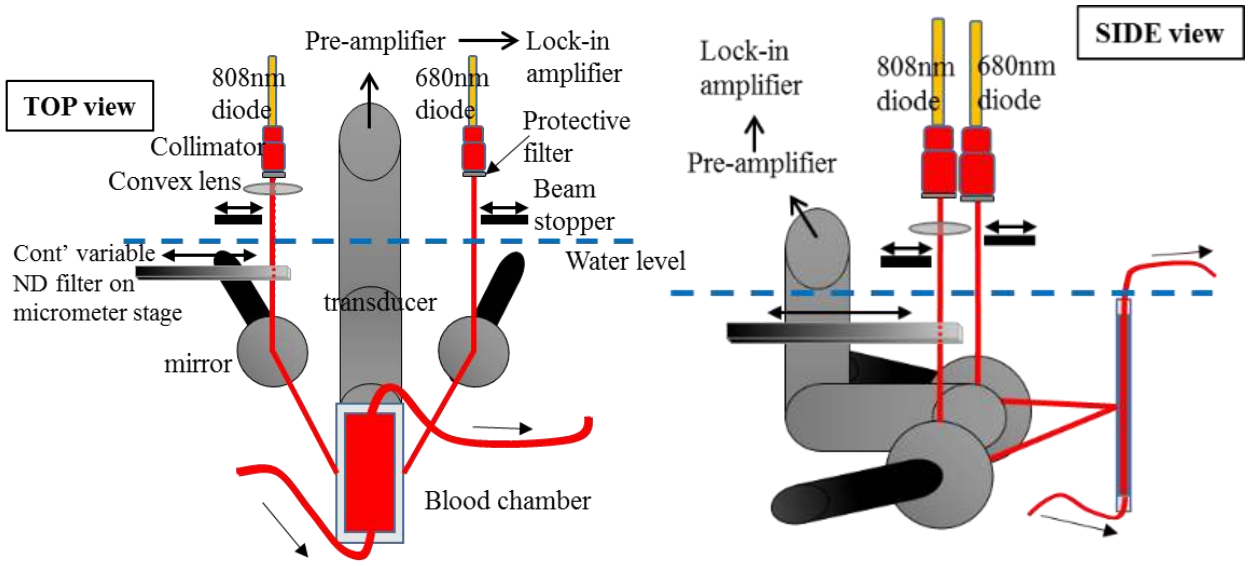

Figure 4.3 Assembled WM-DPAS set-up. The two laser beams are directed to the identical spot of the sample using mirrors. A continuously variable ND filter sweeps the 808-nm beam for the R-scan. The sample can be easily replaced by others.

4.3 System testing

4.3.1 Optical waveforms

Upon the assembly of the WM-DPAS laser box, their optical behaviors were tested. When the 680-nm diode was square-wave modulated at 1-MHz and 5-MHz modulation frequencies, its optical waveforms were detected by a photodiode (DET10A; Thorlabs, NJ, USA). The detected signals were then compared with the function generator and driver output signals in **Figure 4.4**. At both modulation frequencies, the optical waveforms showed reasonable square-wave shapes required for the reliable WM-DPAS experiments.

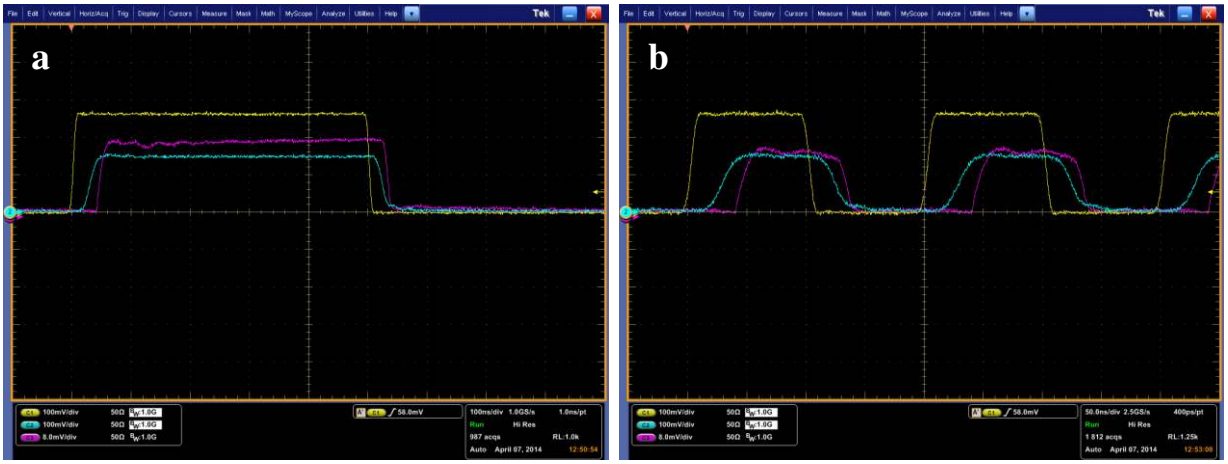

Figure 4.4 The function generator input voltage was fixed at 400mV while the 680-nm beam was square-wave modulated at **(a)** 1-MHz and **(b)** 5-MHz. Yellow: Function generator, Blue: Driver, and Purple: 680-nm diode optical waveform.

Unfortunately, during the system testing, the 808-nm diode system failed and had to be sent back to the manufacturer for assessment and repair. In the meantime, a local LLS laser with the same 808-nm wavelength (LLS8800; Laser Light Solution, NJ, USA) was temporarily adopted for the further measurements. Since the LLS laser had the same wavelength as the failed RPMC 808-nm laser, planned WM-DPAS experiments could be carried out with no delay. Prior to directing the two laser beams of different wavelengths to the sample, their optical waveforms were also monitored with the photodiode. As shown in **Figure 4.5(a)** for the 680-nm laser and **Figure 4.5(b)** for the 808-nm laser, each laser was square-wave modulated out-of-phase at 0.3-MHz and their optical power was adjusted to a similar level. When they were turned on at the same time,

the two beams almost cancelled each other out, producing a steady baseline as seen in **Figure 4.5(c)**. The baseline was not as steady as expected because two different "diode + driver" sets were used (RPMC diode + MESSTEC driver and LLS diode + LLS driver) and their waveform stabilities showed small variations when observed on the oscilloscope (not shown). We expect that the repaired RPMC 808-nm diode system will show much closer beam stability to the RPMC 680-nm system since they will both be modulated by identical MESSTEC drivers. This, in turn, will improve the differential waveform shape. All optical waveforms detected by the photodiode were displayed on an oscilloscope (DPO7104; Tektronix, OR, USA).

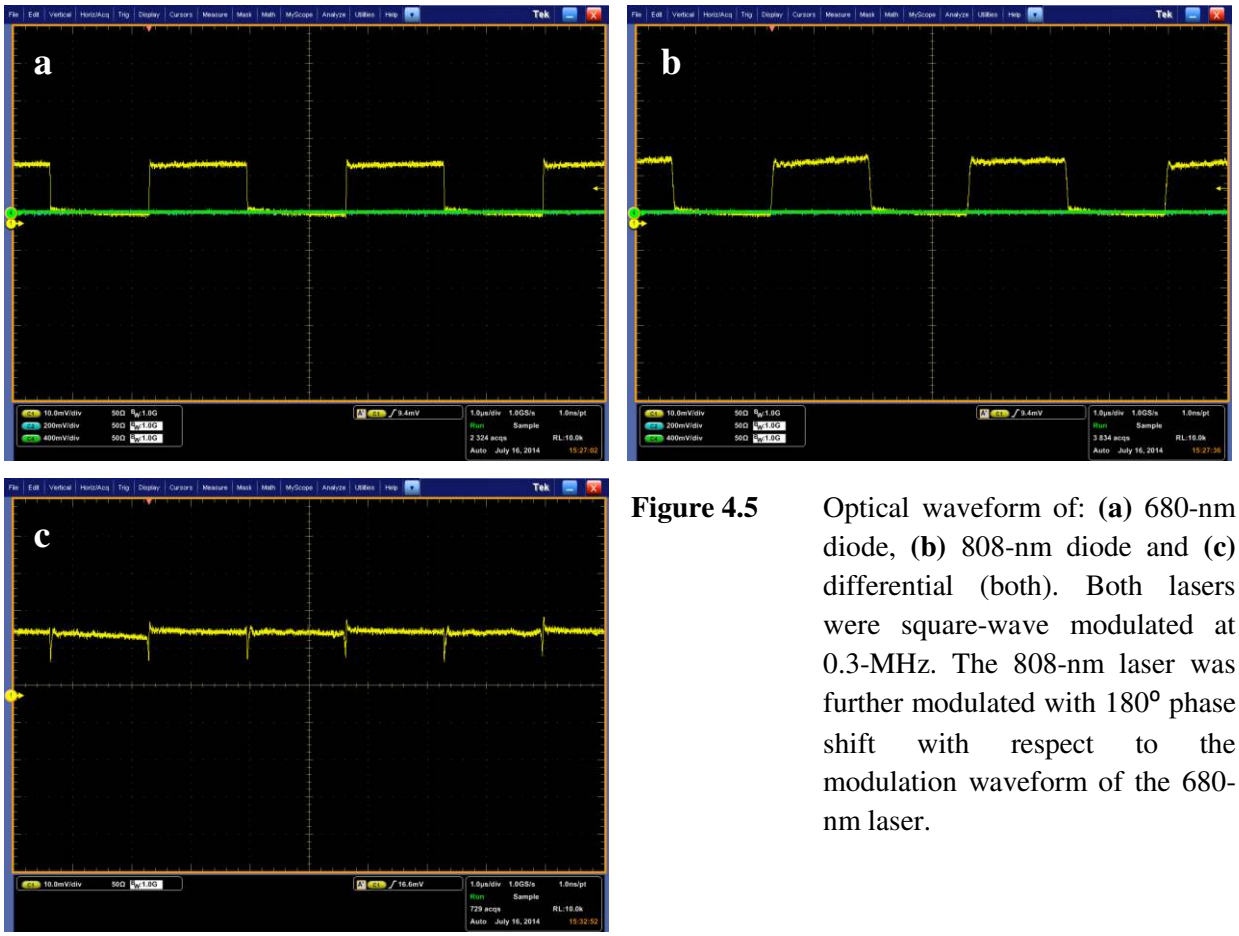

Figure 4.5 Optical waveform of: **(a)** 680-nm diode, **(b)** 808-nm diode and **(c)** differential (both). Both lasers were square-wave modulated at 0.3-MHz. The 808-nm laser was further modulated with 180° phase shift with respect to the modulation waveform of the 680-nm laser.

4.3.2 Optical power stability

A reliable differential PA signal arises from the stable optical input. Without the TEC controller, the optical waveform was acceptable but the optical power of the 680-nm diode was constantly falling over time as shown in **Figure 4.6**. Consequently, the received differential PA signal did

not get stabilized even after 30 minutes of sample exposure to the laser. However, the optical power stability is enhanced to a great extent as the installed TEC controller kept the diode temperature fixed arbitrarily at 20°C during the laser operation. Without the TEC controller, the maximum power the laser could reach was about 1.2W and the power degraded to about 1.15W over time. However, with the TEC controller integrated in the system, not only the stability, but also the maximum power (nearly 1.36W) showed evident improvement. The LLS 808-nm laser already had its own TEC controller installed in the system and showed great stability over time (not shown).

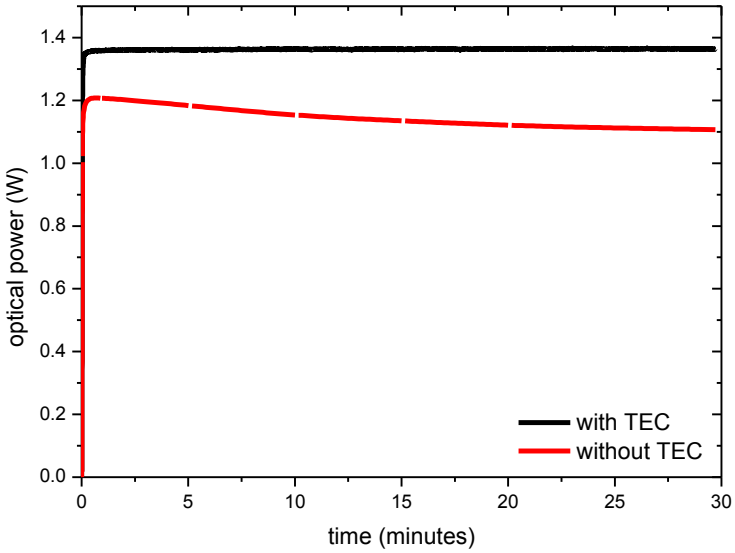

Figure 4.6 Optical power stability of the 680-nm diode over time. Without the TEC controller, the optical power continuously fell. Installation of the TEC controller significantly enhanced the optical power stability.

4.4 Conclusions

The developed WM-DPAS theory and simulation must be verified experimentally to prove its capability for early breast-tumor detection. For that purpose, the initial WM-DPAS laser source was assembled and its performance was tested in terms of optical waveform and power. In the course of development, a few accessories such as filters and a TEC controller needed to be added to the system to enhance the system sensitivity and stability. In this chapter, the experimental system configuration for the differential measurement was also introduced. Single-ended PA and

WM-DPAS experiments performed using the described WM-DPAS system set-up is presented in the following chapters.

Chapter 5

Preliminary WM-DPAS experiments: Study of the single-ended PA responses

To understand the PA signals of the novel differential system, single-ended PA responses need to be studied thoroughly beforehand since differential signals arise from the individual single-ended signals [106]. System parameters must be identified and optimized in the single-ended mode so that once they are applied together for the differential measurement, the system behaves as predicted and simulated as presented in **Chapter 3**. In this chapter, single-ended PA studies are investigated as a preliminary WM-DPAS measurement and compared to a limiting case of the developed theoretical formalism.

Although the WM-DPAS system is expected to be operating at a single modulation frequency between 1 and 5-MHz for the optimized probing sensitivity and depth, the waveforms were usually square-wave modulated at 0.3-MHz in the following experiments due to its high SNR. While the system suffered from high RF (radio-frequency) noise from the laser driver at higher modulation frequencies (> 1-MHz), the waveforms at a relatively low modulation frequency generated reliable PA responses. However, it should be noted that the system needs to be further optimized to operate sensitively at higher modulation frequencies.

5.1 Single-ended PA waveforms

Obtaining the correct PA waveform is important in terms of validating the developed WM-DPAS theory as the differential signal would arise from these waveforms [106]. An experimental time-domain PA waveform was traced and compared to the theoretical prediction introduced in **section 3.1.1** in the limit of single-laser square-wave excitation.

5.1.1 Experimental set-up for waveform analysis

The PA waveform analysis was performed using a single-ended 808-nm diode laser as an optical source and a black anodized metal as a PA source. As depicted in **Figure 5.1**, the 808-nm laser was square-wave modulated at 0.3-MHz by the function generator (33522B; Agilent, CA, USA) and directed to the black-anodized metal immersed in water. The generated PA signal was detected with a single-element 1.0-MHz focused transducer (V314; Olympus Panametrics, CA, USA) and then processed with locally programmed lock-in amplifier and oscilloscope *Labview* software followed by amplification. Slightly modified from the experimental configuration described in **Figure 4.3**, the blood chamber was replaced by the black anodized metal. The metal was polished thoroughly with a generic sand paper to ensure a flat surface onto which the laser beam can be illuminated. With the 680-nm diode turned off, the 808-nm diode alone was operated for this study at a fixed 1.4W power. The semi-infinite black anodized metal was an ideal sample for such waveform analysis since it has a high absorption coefficient and undergoes no deformation during laser irradiation.

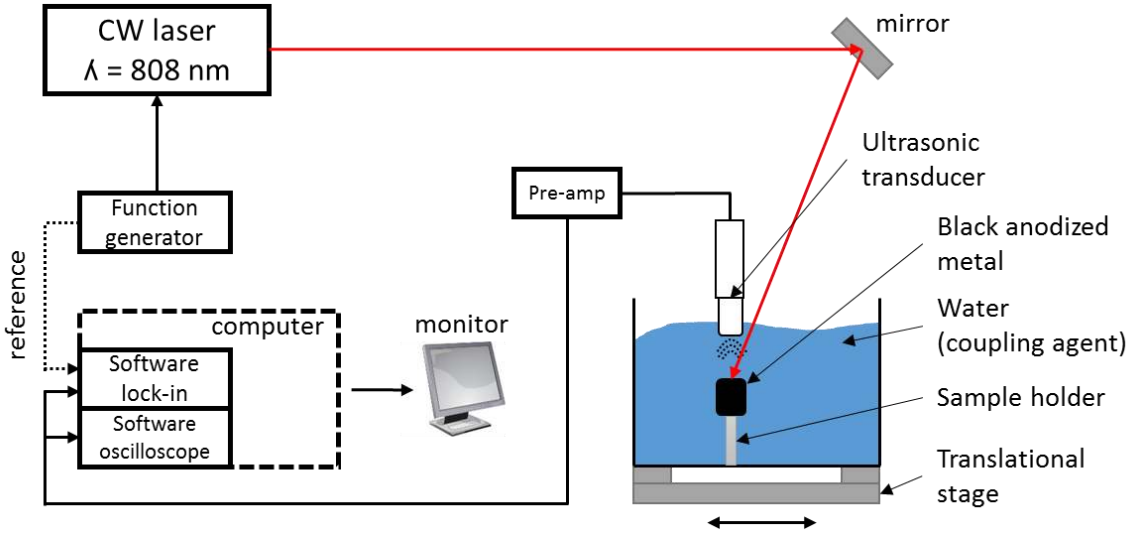

Figure 5.1 Single-ended PA experimental set-up schematic diagram. A locally developed software time-domain waveform tracer reconstructed the waveform for comparison with the prediction.

5.1.2 Results and discussion

The theory of single-ended PA signal generation was explained in Eqs. (6) and (6-1) in **chapter 3**. From these equations, the theoretical waveform was simulated and compared to the obtained experimental result in **Figure 5.2(a)**. As predicted, the generated single-ended PA signal showed an asymmetrical triangular shaped waveform with a point discontinuity at the same 0.3-MHz frequency. Such a waveform was expected because the square-waveform modulated optical input carries an optical intensity only at the first half of its period as shown in **Figure 5.2(b)**. Therefore, when the metal absorbed photons during the first half, it gradually generated the corresponding PA signal with a certain rise time. However, as the optical intensity dropped to zero during the second half of the period, the PA signal fell to the baseline at the same rate as the first half. Acknowledging that the experimental square-wave modulation was not as clear as the theoretical optical modulation as compared in **Figure 5.2(b)**, **Figure 5.2(a)** showed an excellent agreement between the theoretical waveform and the experimental response in the limit of single-laser square-wave excitation. Some parameters assumed for best-fitting the experimental response waveform to the theory include v_a = 1.57E5cm/s and μ_a = 9cm^{-1}, where v_a is the speed of sound in the absorbing medium and μ_a is the absorption coefficient of the anodized metal.

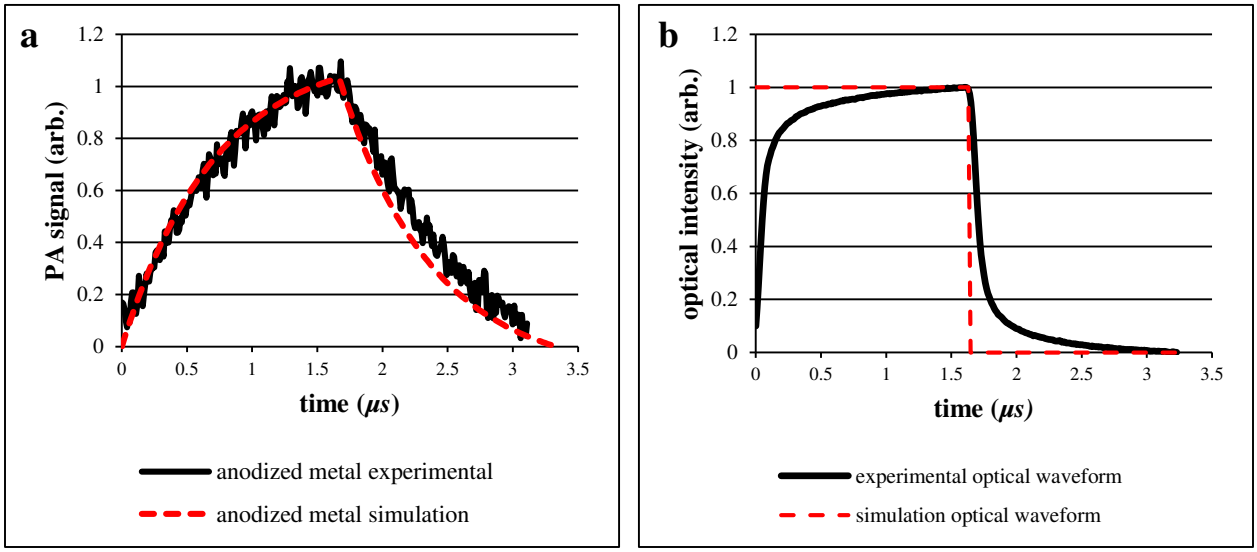

Figure 5.2 A period of **(a)** single-ended PA signal waveforms and **(b)** square-wave modulated input optical waveforms. In both cases, experimental results were compared to the corresponding theoretical prediction in the limit of single-laser square-wave excitation.

5.2 Single-ended PA responses from sample with varied absorption coefficients

As described in the earlier chapters, the properly tuned WM-DPAS system could be highly sensitive to changes in C_{Hb} and StO_2 which altogether alter the absorption coefficient of hemoglobin (*Hb*). Before analyzing complex blood responses, the single-ended PA response was studied using black paint solution with increasing absorption coefficient. Such a study was necessary to test the repeatability and stability of the built instrumentation before moving on to the more complex differential modes of sample excitation.

5.2.1 Black paint experimental set-up

The single-ended 680-nm diode laser was square-wave modulated at 0.3-MHz by a function generator (33522B; Agilent, CA, USA) and a single-element 1-MHz focused ultrasonic transducer (V314; Olympus Panametrics, CA, USA) was employed as a detector. The detected PA signal was then processed by a locally programmed lock-in amplifier *Labview* software followed by amplification as described in **Figure 5.1**. The experimental configuration in **Figure 4.3** was modified to have a customized water container in place of the blood chamber. The front wall of the water container had a small window which was covered by a thin plastic film (generic food wrap) as shown in **Figure 5.3**. The thin plastic film provided an excellent PA measurement window while preventing the black paint solution from mixing up with the coupling agent.

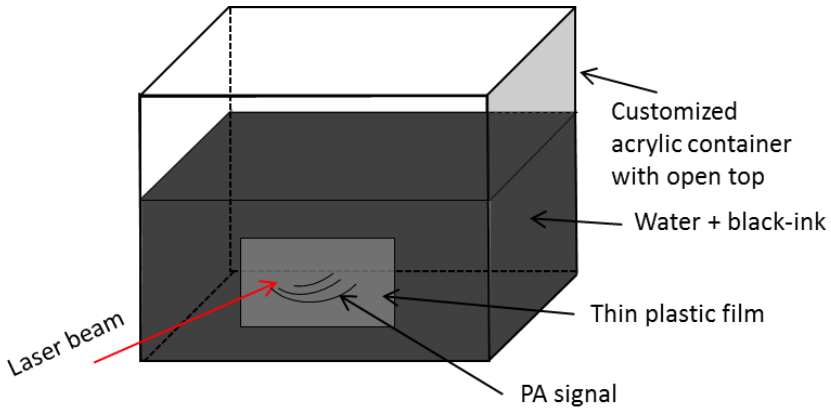

Figure 5.3 A customized black ink solution container. The contents were separated from the surrounding coupling agent (de-ionized water) while a thin plastic film provided an excellent optical measurement window with better impedance matching than the surrounding acrylic wall.

When increasing the absorption coefficient of the solution, a few drops of water-soluble black ink (7011; Trodat, OOE, AU) were added to the solution through the open top of the container, and were thoroughly mixed with a glass rod to ensure sample homogeneity. A small portion of the solution was transferred to a 2mm thick glass cuvette (I-G-2; Starna cells, CA, USA). The 808-nm laser beam was then directed to one surface of the cuvette and the transmitted optical power was detected by a power meter (PM200; Thorlabs, NJ, USA) on the opposite side of the cuvette. Using the Beer-Lambert law shown in Eq. (17) [107], where I is the transmitted laser power, I_0 is the original laser power, and L is the thickness of the optical cuvette,

$$\mu_a = \ln\frac{I}{I_0}\Big/_{-L} \tag{17}$$

the absorption coefficient of each sample was calculated. Throughout the experiment, six samples with different absorption coefficients (0.45, 2.10, 4.246, 7.70, 10.26 and 12.72-cm^{-1}) were tested with the assembled set-up.

5.2.2 Results and discussion

With the described experiment set-up, both the PA lock-in amplitude and phase signal showed clear trends over the range of absorption coefficient from 0.45 to 12.72cm^{-1}, forming a relationship between the PA signal and the black paint absorption coefficients at 0.3-MHz modulation frequency. As shown in **Figure 5.4**, the lock-in amplitude showed a logarithmic-shaped trend and the lock-in phase showed a linear trend.

Since the absorption spectrum of the commercial black ink was not known, further analysis was meaningless. However, such an experiment was necessary, as both the amplitude and phase showed negligible standard deviation (≤ 1% of the actual signal) at each data point, suggesting high repeatability and stability of the built WM-DPAS system.

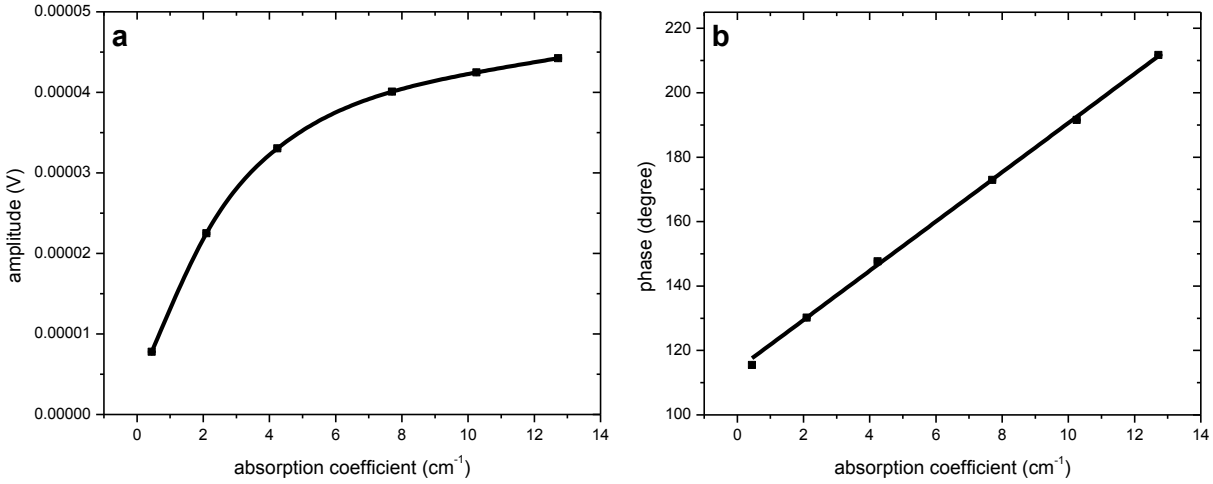

Figure 5.4 The 680-nm single-ended PA lock-in **(a)** amplitude and **(b)** phase responses over increasing absorption coefficients of the black paint solution.

5.3 Single-ended *in-vivo* mouse imaging: initial WM-DPAS animal study

The ultimate application of the WM-DPAS system will be integrated into the developed FD-PAR imager. Therefore, in parallel to the WM-DPAS development, single-ended 680-nm and 808-nm diode lasers were used to initiate a differential *in-vivo* animal imaging experiment. Even though the principle of the introduced WM-DPAS system has not yet been applied, the following *in-vivo* imaging experiment demonstrated the possibility of performing spectroscopic PA probing and imaging using two laser modulations with mismatched coded excitations. Such *simultaneous* illumination of the lasers is the basic concept of the WM-DPAS system and is important for *in-vivo* imaging that involves moving fluids such as blood, or moving body parts due to heart beating or breathing. Therefore, this study successfully laid the foundation of future WM-DPAS *in-vivo* studies.

5.3.1 Animal protocol and tumor model

The protocol for the mouse experiments has been approved by the University of Toronto (protocol#: 20010465). A 23.5g female immune-deficient nude mouse (CD-1) was ordered from Charles River (MA, USA). While the animal was housed in a special animal housing facility of

the Faculty of Medicine (Division of Comparative Medicine (DCM), University of Toronto, ON, CA) under sterile conditions with 12-hour light-dark cycle and sterilized standard laboratory diet& water, human hypopharyngeal head-and-neck carcinoma FaDu cells from ATCC (American Type Culture Collection; VA, USA) were cultured in minimum essential medium (MEM F-15) supplemented with 10% fetal bovine serum (FBS) by our collaborator Dr. Willa Shi (Ontario Cancer Institute and University Health Network, ON, CA) at Princess Margaret Hospital (ON, CA). Cultured cells were harvested in culture flasks, detached using trypsin/Ethylenediaminetetraacetic acid (EDTA) treatment, and washed with phosphate buffer saline (PBS). Cell number was determined using a Casy cell counter (Schärfe System GmbH, Reutlingen, Germany) before injection. Prepared FaDu cells were then centrifuged, diluted and dissolved in the culture medium. After the prepared cells were transferred to DCM, 5.0E6 cells in 30-μL medium were injected to the left thigh of the mouse at 3mm depth (targeting the caudal thigh muscle) by a DCM technician using a 25-gauge needle. Tumor growth was monitored during the weekdays with a digital caliper.

5.3.2 Mouse imaging experimental set-up

After 21 days from the injection, the tumor growth was clear enough to be visible to the naked eye, and the DCM technician announced the growth end-point (~4mm). **Figure 5.5** shows the mouse bearing a full-grown tumor on its left thigh indicated by the dashed circle. The animal was then transferred to the CADIFT facility for non-invasive PA scanning under anesthesia with vaporized isoflurane gas (1.4 L/min O_2 and 1 L/min isoflurane). An infra-red (IR) lamp borrowed from DCM and aquarium heater (06105; Aqueon, WI, USA) were also used to keep the animal body temperature at a constant bio-level based on the protocol.

Figure 5.5 A picture of the mouse bearing a full grown tumor. The tumor site is indicated by the dashed circle.

The experimental set-up was prepared as described in **Figures 5.6 and 5.7**. Under anesthesia with isoflurane gas, the bottom half of the animal (including the tumor-bearing thigh) was submerged in the pre-warmed water. The 680-nm laser was modulated with an up-sweeping sinusoidal chirp from 0.3 to 1.3-MHz from the dual-channel function generator (33522B; Agilent, CA, USA) at a 1.3W power (close to its maximum) while the 808-nm diode laser was modulated with a down-sweeping sinusoidal chirp from 1.3 to 0.3-MHz from the same function generator at a 3.0W power (close to its maximum). For both cases, the chirp duration was 1ms and 50 chirps were averaged to increase the SNR. The two laser beams were collimated to 0.8mm but extended to ~ 8mm when they simultaneously reached the mouse thigh. To accurately image the tumor at the thigh muscle, the two laser fibers and the transducer were moved along the thigh for an A-scan (2-dimensional linear scan). A 64-element 2.8-MHz phased array transducer (SA4 2/24; Ultrasonix, BC, CA) was used to detect the back-propagating PA signal from the tumor while its head was submerged in the water for acoustic coupling. Received PA signals were amplified by a set of pre-amplifiers (28082; HD communications, NY, US) and reconstructed with a locally developed *Labview* program. Upon the completion of PA screening, a direct comparison could be made with a commercial ultrasound imager (Ultrasonix, BC, CA) since the same transducer was compatible in both the PAR and Ultrasonix systems; the transducer head position was fixed in the water tank, but only the zero force insertion (ZIF) connection was freely moved between the PAR and Ultrasonix imagers. Once the scans were done, the animal was euthanized by an

isoflurane over-dose and cervical dislocation. The deceased animal was placed in a biobag for disposal by DCM. All animal handling in the laboratory was performed according to DCM guidelines.

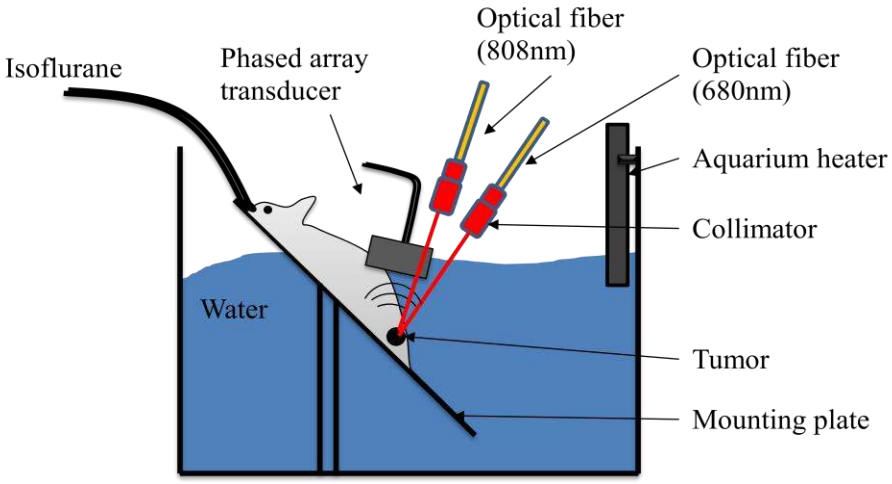

Figure 5.6 Schematic diagram of the *in-vivo* mouse imaging experiment.

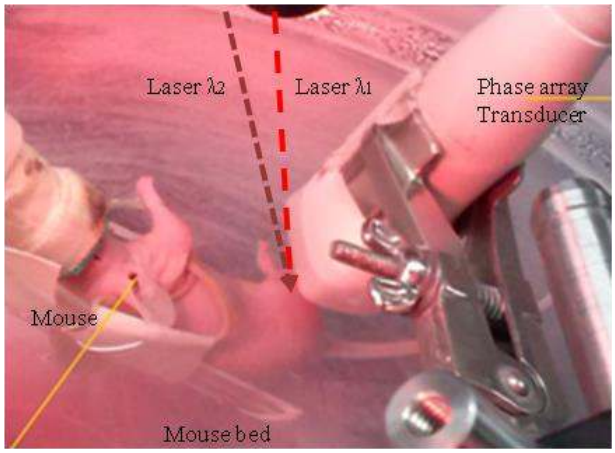

Figure 5.7 A picture of the *in-vivo* mouse imaging experiment [108].

5.3.3 Results and discussion

When the animal's tumor-bearing thigh was imaged by the pure ultrasound imager, as shown in **Figure 5.8**, the tumor was rather hard to differentiate as the surrounding body parts such as bones and fat also acted as an acoustic reflector. The tumor site did not show enough contrast with the background to clearly indicate the presence of the tumor. Knowing the location of the

tumor site, however, the tumor could still be identified in the obtained ultrasound image with limited information (indicated with the dashed circle).

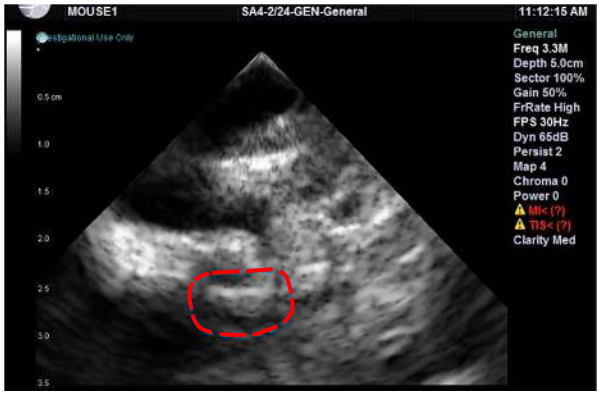

Figure 5.8 Pure *in-vivo* ultrasound image of the mouse thigh bearing a full-grown tumor. The tumor could not be differentiated easily from the background [108].

Figure 5.9(a) shows the PA image generated using the 808-nm laser (emitted alone) when the laser and transducer were scanned over the same tumor site. **Figures 5.9(b) and (c)** show the PA images generated by the 808-nm and 680-nm lasers (emitted together) over the same tumor region. Comparing to the shown pure ultrasound image, in all the PA images in **Figure 5.9**, the tumor site showed much better contrast against the surrounding region. In general, the images from the 808-nm laser (**Figures 5.9(a) and (b)**) showed clearer tumor site larger than the 680-nm image. This is because the optical power of the 808-nm laser was stronger than that of the 680-nm laser in the experiment. In addition, according to the *Hb* extinction coefficient spectrum shown in **Figures 1.4 and 3.1**, the 680-nm laser beam is absorbed more strongly by de-oxygenated *Hb* at the tumor than the 808-nm laser beam; therefore, most of the 680-nm beam is thought to be absorbed close to the tumor surface while the 808-nm light penetrates deeper. This may explain why **Figure 5.9(c)** shows a comparatively thinner image of the tumor.

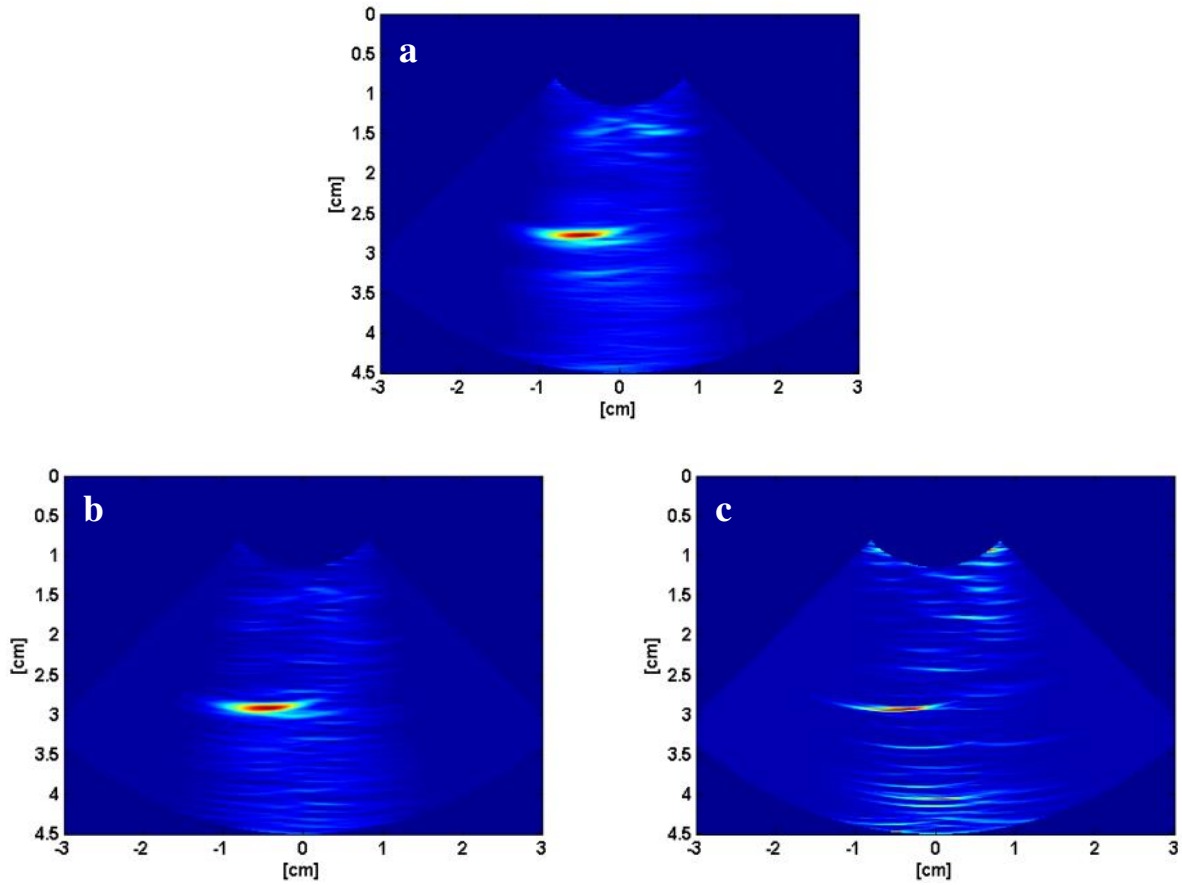

Figure 5.9 Single-ended PA images of the tumor-bearing mouse thigh by **(a)** the 808-nm laser alone, **(b)** the 808-nm laser while both lasers were on, **(c)** the 680-nm laser while both lasers were on [108].

It was demonstrated that, by using mismatched coded excitations, the PA response from each wavelength could be separated out from the combined signal with minimal interference. Since the aforementioned surrounding body parts did not act as strong light absorbers at either 680-nm or 808-nm wavelengths, the PA images were free from the corresponding artifacts. Some other signals were also picked up in the images possibly due to the presence of other light absorbers near the imaging area (i.e. other blood vessels). Since the 680-nm laser is more sensitive to deoxygenated blood than the 808-nm laser, other signals observed in Figure 5.9(c) could be veins. The system was still highly sensitive to increased C_{Hb} due to excessive angiogenesis or decreased StO_2 due to hypoxia at the tumor site, and the tumor could be easily identified at ~2.7cm below the transducer surface. Comparing to the ultrasound image, the PA images exhibited better resolution and superior contrast.

5.4 Conclusions

The development of the WM-DPAS system requires thorough single-ended preliminary PA studies. In this chapter, the single-ended PA responses at 680-nm and 808-nm wavelengths were analyzed under various conditions. The results altogether suggested agreement with the introduced PA theoretical formalisms and demonstrated the capability of future *in-vivo* WM-DPAS spectroscopic studies.

Chapter 6

Initial WM-DPAS study on *in-vitro* blood circulation system

From a biological point of view, tumors are wrapped by an extraordinary amount of cancerous leaky blood vessels (capillary vessels) due to excessive angiogenesis [43, 55-59, 65-75]. Therefore, when the laser illuminates the tumor site during PA probing or imaging, the PA signal is generated based on the optical properties of hemoglobin (*Hb*) in the collection of blood vessels around the tumor. When studying such a system, an artificial blood circulation system which simulates the human vasculature can be used as an excellent alternative methodology to the regular *in-vivo* approaches involving live animals or human participants. This *in-vitro* system is advantageous for the initial study because it allows a macro-scale optimization and tight control of *Hb* optical properties.

6.1 WM-DPAS *in-vitro* study

6.1.1 Experimental set-up: Blood circulation system and *Hb* deoxygenation

During the system assembly, 500-mL bottles of fresh and sterile heparinized sheep blood (CL2581-500H; ON, CA) were purchased every two weeks from Cederlane. While they were stored at a 4°C temperature in the laboratory fridge, the blood bottles that passed the expiration date (3 weeks after the date of collection) were not used due to coagulation. Before use, each fresh bottle was shaken well to ensure the homogeneity of the blood and then 60mL of blood was transferred to a 100-mL commercial blood bag with two standard size openings (JB1302; Baxter, IL, USA) using a syringe. This blood bag, originally containing 0.9% sodium chloride solution, was emptied, cleaned with deionized water, and dried thoroughly before storing the blood. After the transfer, the air inside the bag was squeezed out to ensure a complete vacuumed system inside the bag as seen in **Figure 6.1**.

Once the blood source was prepared, the *in-vitro* blood circulation system was assembled as depicted in **Figure 6.2** (without the connection to the blood source yet) and a peristaltic pump (5201; Heidolph, BY, DE) introduced one sucking and one pushing end of the tube at 15-rpm. Then, the sucking end of the tube was carefully connected to one opening of the blood bag without introducing any air into the system. The sheep blood was allowed to continuously circulate through the system while the pushing end of the tube was placed in a disposal flask. As all the air in the system was pushed out by the flowing blood, the pushing end of the tube was carefully connected to the other opening of the blood bag while the pump was still running. A completed vacuumed blood circulating system was capable of circulating the blood for 7 to 8 hours without any coagulation. The room temperature was kept at 20°C at all times.

Figure 6.1 Prepared blood bag (blood source) containing the sheep blood. Air was completely removed to prevent any coagulation during the experiment. Generic paper clamps were also placed as shown as an extra safeguard to ensure no contact between blood and air.

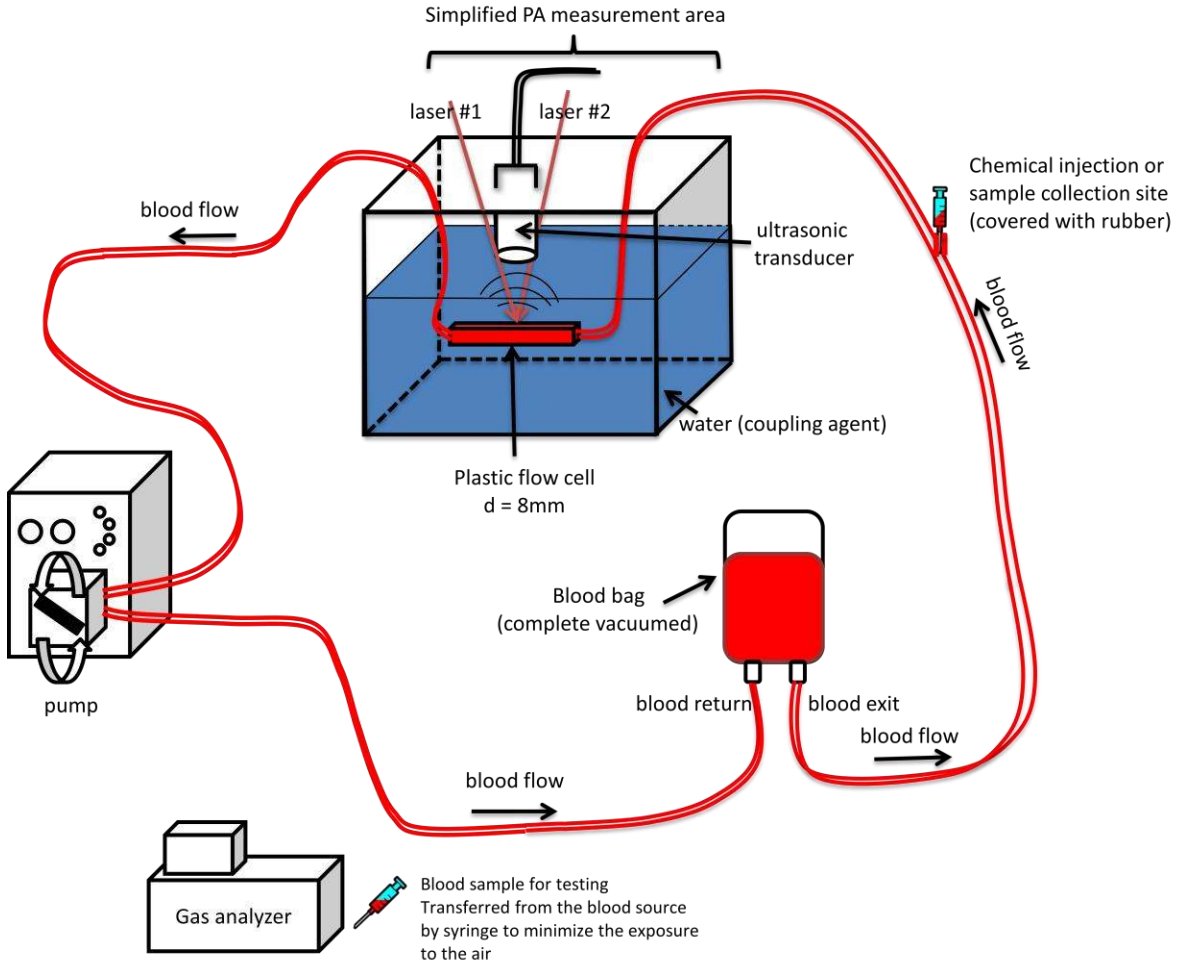

Figure 6.2 Schematic diagram of the blood circulation system. This system is isolated from the air to prevent any blood coagulation during the experiment. In this diagram, the PA measurement area is simplified. A detailed configuration of the PA measurement area is described in **Figure 4.3**.

Blood deoxygenation was achieved using Sodium dithionite ($Na_2O_4S_2$; Sigma-Aldrich, MO, USA). Based on the published protocol [109], a specific amount of chemical powder was diluted in ~1.5mL of fresh sheep blood and the diluted solution was slowly injected into the circulation system using a syringe. After allowing 10 minutes for system stabilization, about 0.3mL of the blood sample was taken out of the system using a new syringe while the pump was temporarily turned off. The blood sample was then uploaded to a B-cassette (OPTImedical, GA, USA) and blood parameters including C_{Hb} and StO_2 of the specific blood sample were confirmed by the commercial blood gas analyzer (CCA-TS; OPTImedical, GA, USA). The used heparinized blood

was then diluted with tap water and disposed down the sanitary drains (as confirmed by the institute biosafety officer, no regulatory requirements for disposal lay on the sterile sheep blood).

6.1.2 Experiment procedures

Two diodes (λ_A = 680-nm and λ_B = 808-nm) were directed to the surface of an 8-mm plastic flow cell (CFCAS0004; IBI Scientific, IA, USA) for the differential PA measurement as described in **Figure 6.2**. A detailed PA measurement area is shown in **Figure 4.3**. For the initial study, the plastic flow cell, shown in **Figure 6.3**, was an ideal blood holder because of its flat surface. Previous single-ended experiments revealed that PA signals sensitively fluctuate when the sample surface is uneven. Also, the two collimated beams extended to ~15mm when they reached the sample surface. Therefore the thin plastic tube with small diameter (~7mm) was inadequate to cover the entire beam size. An alternative option of reducing the beam size using lenses was also considered, but disregarded as concentrated beam power could damage the sample over time.

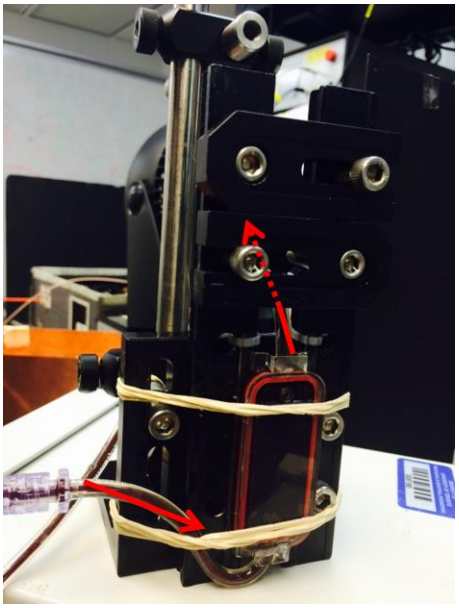

Figure 6.3 A plastic flow cell containing circulating blood. The blood flow is indicated by the red arrows. A thin plastic cover ensures surface flatness which is required for stable PA signal.

The 680-nm and 808-nm lasers were square-wave modulated out-of-phase at a fixed 0.3-MHz by a dual-channel function generator (33522B; Agilent, CA, USA). As described in **section 4.2**, the 1.0-MHz focused transducer was used as a detector. The received PA signal was amplified 40-dB by the pre-amplifier (5662; Olympus Panametrics, CA, USA) and analyzed by the hardware lock-in amplifier (SR822; Stanford Research System, CA, USA). While both lasers were illuminating the sample surface, a continuously variable neutral density filter with OD 0.04 – 1 (64-381; Edmund, NJ, USA) was used to sweep the 808-nm laser beam intensity for the differential R-scan in the range of 0.2 to 1.8. The filter position was controlled by a microscopic stage with 0.01-mm resolution. At each scanning position, not only the differential signal, but also the 680-nm and 808-nm single-ended signals were obtained for comparison. The actual WM-DPAS experimental set-up is depicted in **Figure 6.4**.

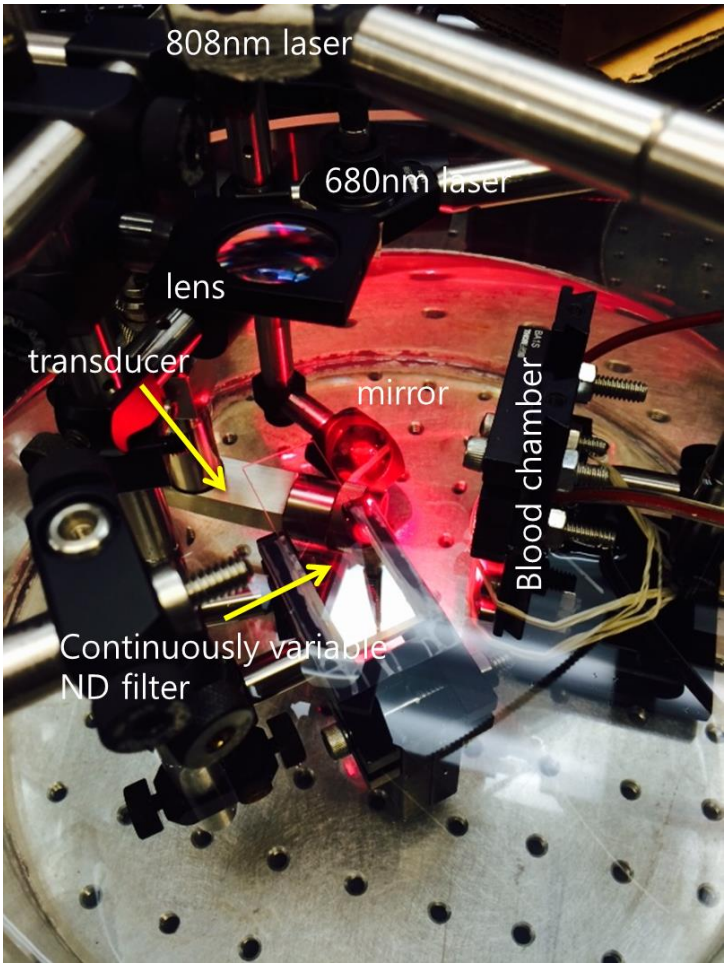

Figure 6.4 A picture of the WM-DPAS measurement area.

6.1.3 Results and discussion

6.1.3.1 WM-DPAS *R*-scan at $dP = 180.08^0$

Figure 6.5(a) shows how the PA signals from each laser changed as the 808-nm laser power decreased. As the filter moved to a higher OD, the PA amplitude from the 808-nm laser decreased accordingly while that from the 680-nm laser did not change much. These were the expected behaviors for the PA amplitude signals, confirming that the optical power of two different lasers caused no cross-talk PA amplitudes. It was further expected that the PA phase signals from the 680-nm and 808-nm diodes would be independent from changes in the 808-nm laser power. The phase difference between the two lasers (*dP*) was fixed at 180.08° during the measurement with 0.25° fluctuations as shown in **Figure 6.5(b)**.

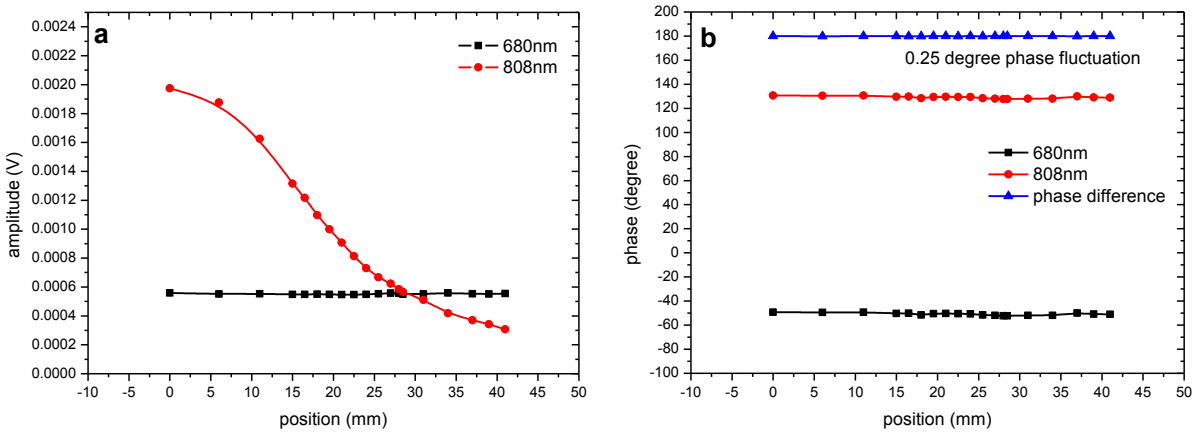

Figure 6.5 Single-ended PA **(a)** amplitude and **(b)** phase signal traces when the continuous ND filter swept the 808-nm laser beam. Lasers were square-wave-modulated at 0.3-MHz with about 180.08° phase difference.

Simulating tissue carcinogenesis, five blood samples of decreasing StO_2 (increasing C_{Hb}) were tested as shown in **Figure 6.6**. As treated with the chemical, StO_2 decreased from 97.1% to 67% while C_{Hb} increased from 8.19E-3 to 1.05E-2M and the color got visibly darker. Among these two benchmarks of breast carcinogenesis, this study focused more on StO_2, but it should be noted that C_{Hb} also could be utilized in a similar way for the same purposes as described in **Chapter 3**. **Figure 6.7** shows the experimental and theoretical differential PA signals as a function of increasing *R* at *dP* = 180.08°. The experimental response showed excellent agreement to the

corresponding theoretical best-fitting in the range of StO_2 studied (*adjusted R-square values* greater than 99.5%). In **Figure 6.7**, for more accurate experimental data fitting to the theory, *Hb* molar extinction coefficient spectrum of adult sheep (shown in **Appendix 3**) was used instead of that of humans. Some parameters used for the best-fitting in **Figure 6.7** include v_a = 1.57E5cm/s, e_{oxA} = 159cm^{-1}/M, e_{deA} = 704cm^{-1}/M, e_{oxB} = 243cm^{-1}/M and e_{deB} = 239cm^{-1}/M, where v_a is the speed of sound in the medium, and e_{ox} and e_{de} are the molar extinction coefficients of oxy- and deoxy- sheep blood at the specific wavelengths, respectively (**Appendix 3**). Based on the laser manufacturers' data, λ_A = 678-nm and λ_B = 804-nm were used for the best-fitting procedure.

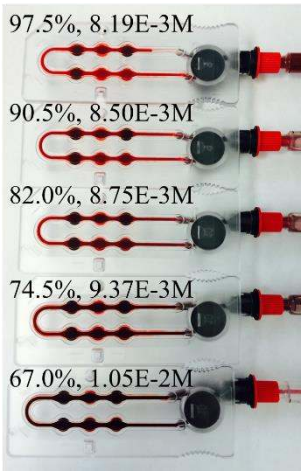

Figure 6.6 Loaded blood samples for blood gas analyzer analysis. As StO_2 decreased, clear color change was observed as expected.

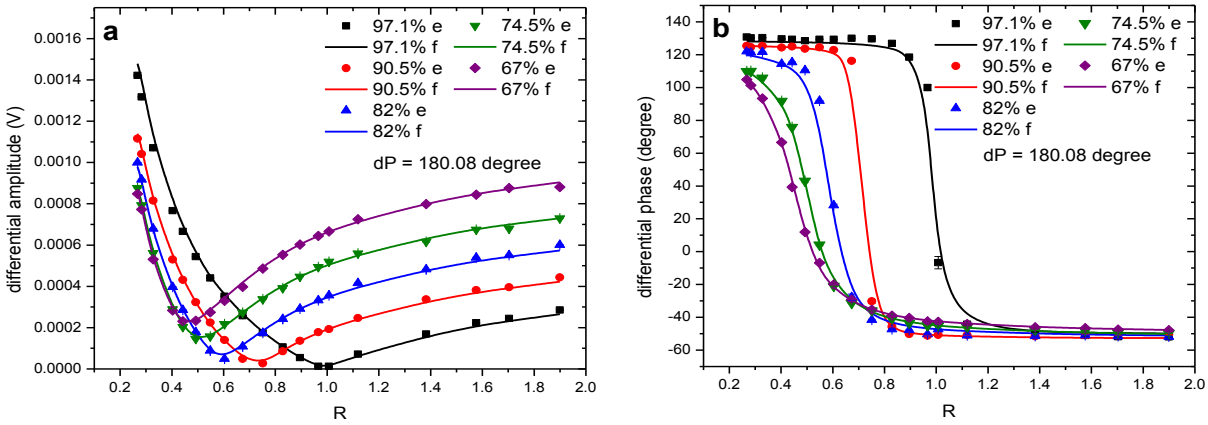

Figure 6.7 PA differential **(a)** amplitude and **(b)** phase signals over increasing *R*. System *dP* was 180.08°. The two lasers were square-wave modulated at 0.3MHz. e – Experimental, f – Best-fitting.

For the differential PA phase signals in **Figure 6.7(b)**, an optimal *R* needs to be chosen (or tuned) based on the optical properties of the tissue to be differentiated for quick pre-malignancy screening purposes. In this case, the sample with oxygenation level 82% (blue) was arbitrarily assumed to be the "pre-malignant" tissue. Consequently, the system was tuned at $R = 0.60$ at which the "pre-malignant" tissue underwent the greatest phase change in **Figure 6.7(b)**. Once the system was tuned at $R = 0.60$ and $dP = 180.08^{o}$, as shown in **Figure 6.8(b)**, the differential phase could be expressed as a function of StO_2. The differential system showed about 149.29^{o} phase change as StO_2 decreased from 97.1% to 67% and a drastic differential phase change happened at near 82% (pre-malignant). On the other hand, the single-ended 680-nm and 808-nm measurements showed only 6.43^{o} and 2.23^{o} phase change respectively over the same range of *Hb* deoxygenation. In **Figure 6.8(a)**, the single-ended 680-nm response appeared to be more sensitive than the 808-nm response over the same range of deoxygenation as expected from the *Hb* extinction coefficient spectrum shown earlier. However, the single-ended 680-nm system was still approximately 23 times less sensitive than the differential system. This suggests that the differential phase of the WM-DPAS system can be used to sensitively detect the pre-malignant tumors based on their optical properties.

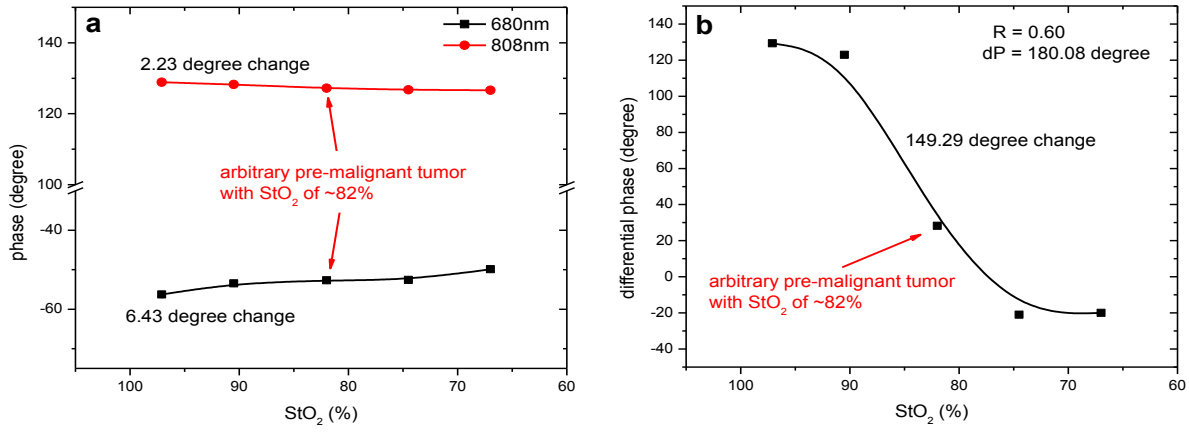

Figure 6.8 PA phase responses of **(a)** the single-ended and **(b)** differential measurements at $R = 0.60$ and $dP = 180.08^{0}$ over decreasing *Hb* oxygenation level. The differential system showed about 149.29^{0} phase change at optimal *R*, 0.60, while the single-ended system showed only 6.43^{0} (at 680-nm) and 2.23^{0} (at 808-nm) phase changes as StO_2 decreased from 97.1% to 67%. The arbitrary pre-malignant tumor is indicated by the red arrow.

To better understand the sensitivity and specificity of the system at R = 0.6 and dP = 180.08° for arbitrary pre-malignancy screening, a similar experiment with more samples was performed as shown in **Figure 6.9**. Due to instrumental limitations, however, the same dP could not be achieved, but a relatively close value of dP = 180.19° was used instead. Here, StO_2 was more resolved by testing 7 different samples from 97.5% and 39.8% and the system showed excellent reproducibility, still being sensitive at near 82% level. With more data points, a clearer step-function-like shape was obtained which showed about 140° phase shift over only a 10% StO_2 decrease while relatively no phase shifts were observed at higher (healthy) and lower ends (malignant) of the graph. Once more it should be underlined that the sample with an 82% oxygenation level was arbitrarily chosen to be pre-malignant in this study. However, as described in **Chapter 3**, the WM-DPAS tunability suggests that once the statistical StO_2 range of breast pre-malignancy becomes available, the system R can be tuned so that the maximum differential phase transition happens at that specific range (sensitivity tunability property).

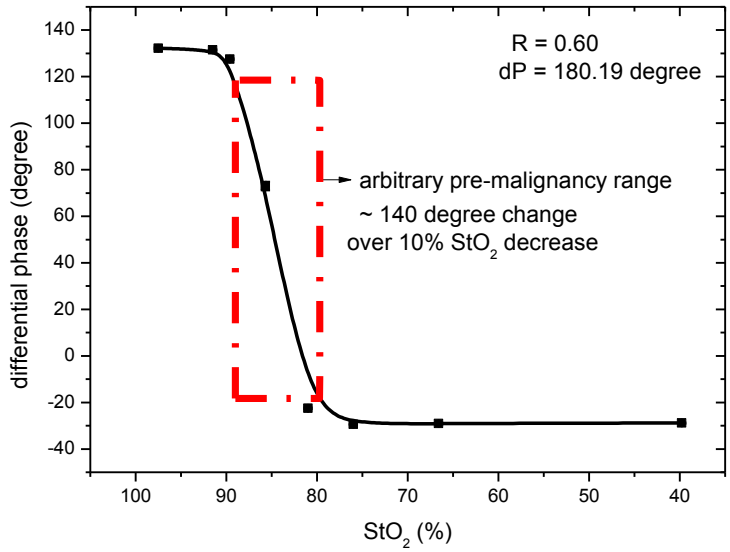

Figure 6.9 PA differential phase signal change as StO_2 decreased from 97.5% to 39.8% when R = 0.60 and dP = 180.19°. The system showed drastic phase shift over 10% StO_2 decrease as indicated by the dashed square.

In a clinical environment, once breast pre-malignancy is detected by the described quick pre-malignancy screening method, the WM-DPAS may also provide clinicians or patients with extra

invaluable information about the tumor: actual values of C_{Hb} and StO_2. For the differential PA amplitude in **Figure 6.7(a)**, R = 0.97 was chosen as optimal since it showed about 4885.12% monotonic phase change as StO_2 decreased from 97.1% to 67% (**Figure 6.10(b)**). On the other hand, the single-ended 680-nm and 808-nm measurements showed only 142.8% and 16.09% phase change respectively over the same range of *Hb* deoxygenation (**Figure 6.10(a)**). The single-ended 680-nm response was more sensitive than the 808-nm response over the same range of deoxygenation and this agreed with the prediction based on the *Hb* extinction coefficient spectrum in **Figures 1.4 and 3.1**. However, the single-ended 680-nm system was still about 34 times less sensitive than the differential system. A strong linearity found at this R and dP combination suggest the potential of using the differential amplitude signals of the WM-DPAS system to quantify the carcinogenesis benchmarks with outstanding resolution.

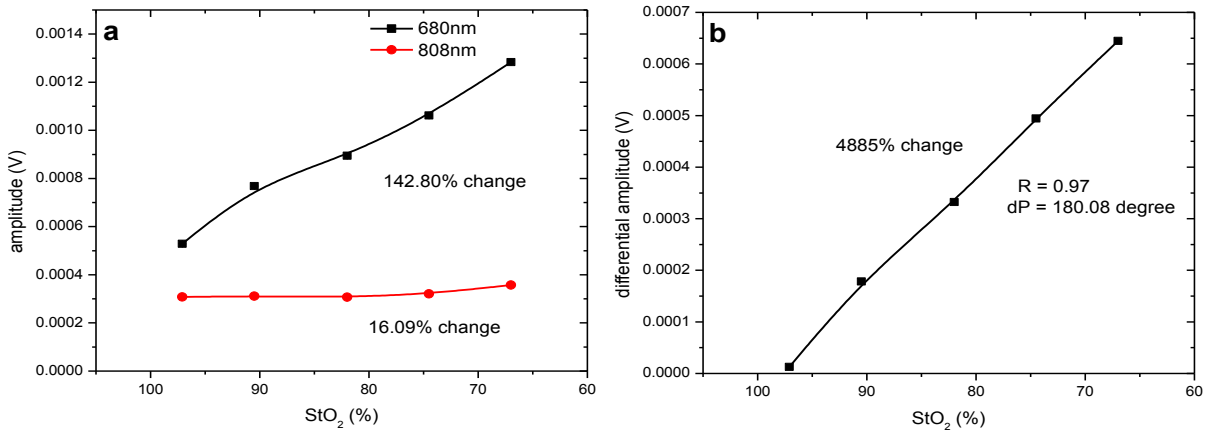

Figure 6.10 PA amplitude responses of **(a)** the single-ended and **(b)** differential measurements at R = 0.97 and dP = 180.08° over decreasing *Hb* oxygenation level. The differential system showed 4885.12% amplitude change at optimal R, 0.97, while the single-ended systems showed only 142.8% (at 680-nm) and 16.09% (at 808-nm) amplitude changes as StO_2 decreased from 97.1% to 67%.

The differential phase signals were also analyzed to find the linearity for the same C_{Hb} and StO_2 quantification purposes and such a capability was also proved through the same set of experiments. When the system was tuned at R = 0.40 and the same dP = 180.08°, the differential phase signal showed better correlation with StO_2 as seen in **Figure 6.11** (compared to **Figure 6.8(b)**). Its sensitivity was also superior to the single-ended results as it showed about 63.12°

phase change as StO_2 decreased from 97.1% to 67%. This suggests that the WM-DPAS system can be tuned differently to meet a variety of clinical needs. However, it was expected that the linearity and sensitivity shown in **Figures 6.10(b) and 6.11** could still be optimized further; therefore *dP* tuning was investigated in the next section to better demonstrate the capability of the WM-DPAS system to quantitatively screen *Hb* properties at different stages of breast cancer. A summary of the experimental results obtained at $dP = 180.08^{o}$ is provided in **Table 6.1**.

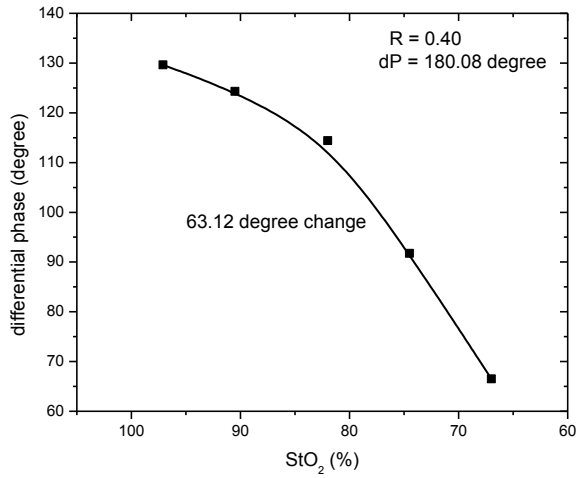

Figure 6.11 PA phase response of differential measurement at $R = 0.40$ and $dP = 180.08^{o}$. By tuning the system at different *R*, a near-linear trend was achievable.

Table 6.1 Differential signal analysis when $dP \approx 180^{o}$.

	differential phase	**differential phase**	**differential phase**	**680nm phase**	**808nm phase**	**differential amplitude**	**680nm amplitude**	**808nm amplitude**
Purpose	Pre-malignancy detection	Pre-malignancy detection	monitoring	x	x	monitoring	x	x
R	0.60	0.60	0.40	x	x	0.97	x	x
dP	180.19^{o}	180.08^{o}	180.08^{o}	x	x	180.08^{o}	x	x
PA signal change	$\sim 140^{o}$ change over the "pre-malignant" StO_2 region	$\sim 150^{o}$ change over the entire StO_2 range of study	63.12^{o}	6.43^{o}	2.43^{o}	4885.12%	142.80%	16.09%
***StO_2* range**	98%-40%	97%-67%	97%-67%	97%-67%	97%-67%	97%-67%	97%-67%	97%-67%
Unit PA signal change	Not applicable	Not applicable	2.10^{o} /%StO_2	0.21^{o} /%StO_2	0.08^{o} /%StO_2	162.84% /%StO_2	4.76% /%StO_2	0.54% /%StO_2
Figure	**6.9**	**6.8(b)**	**6.11**	**6.8(a)**	**6.8(a)**	**6.10(b)**	**6.10(a)**	**6.10(a)**

6.1.3.2 WM-DPAS *R*-scan at $dP = 184.80^0$

Similar to the previous experiment, the differential R-scan was achieved by adjusting the 808-nm optical power using the continuously variable neutral density filter while having the 680-nm optical power fixed. However, *dP* was tuned at 184.80° this time to investigate the effect of *dP* on the WM-DPAS signals. **Figure 6.12** shows the experimental and theoretical differential PA signals as a function of increasing *R* at *dP* = 184.80°. Both the differential amplitude and differential phase exhibited trends similar to the theoretical predictions and simulations in **Figure 3.3** as StO_2 decreased from 94.7% to 74.6%; when *dP* was modulated slightly away from 180°, the differential amplitude and phase signals over increasing *R* lost the low-end point discontinuity and steep phase shift, respectively. All the fitting results were highly agreeable with the *adjusted R-squared values* near 99.5% except for the sample with 74.6% StO_2 which showed the *adjusted R-squared value* of 97.9%. Such discrepancy shown between experimental and fitting results for the StO_2 = 74.6% sample ($R > 1.0$) is possibly due to the optical power drift during the operation. Some parameters used for the best-fitting include v_a = 1.57E5cm/s, e_{oxA} = 159cm^{-1}/M, e_{deA} = 704cm^{-1}/M, e_{oxB} = 243cm^{-1}/M and e_{deB} = 239cm^{-1}/M, where v_a is the speed of sound in the medium, and e_{ox} and e_{de} are the molar extinction coefficients of oxygenated and deoxygenated sheep blood at the specific wavelengths, respectively (**Appendix 3**). Based on the laser manufacturers' data, λ_A = 678-nm and λ_B = 804-nm were used for the best-fitting procedure.

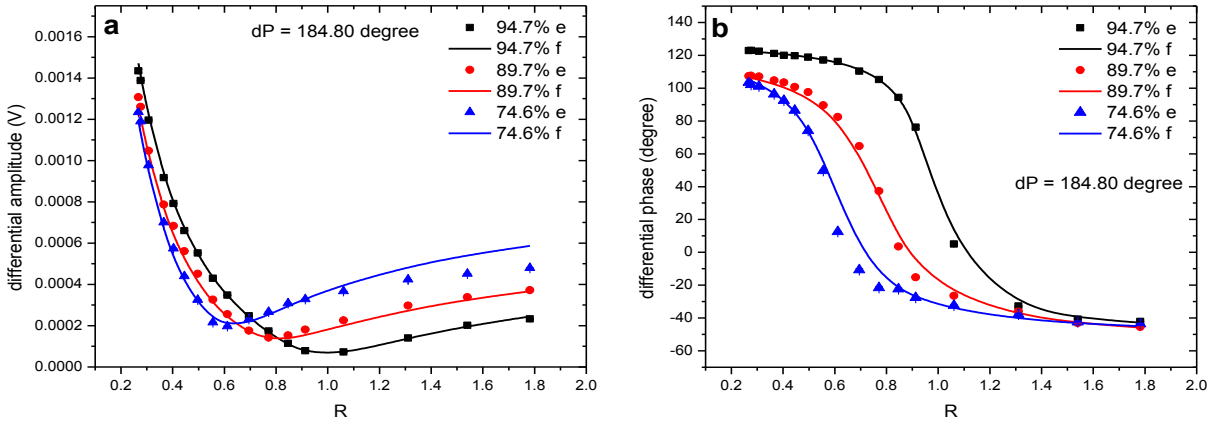

Figure 6.12 PA differential **(a)** amplitude and **(b)** phase signals over increasing *R*. System *dP* was 184.80°. The two lasers were square-wave modulated at 0.3MHz. e – Experimental, f – Best-fitting.

At dP = 184.80°, a drastic phase shift was no more observed at any R in the range of 0.2 – 1.8 when the differential phase was represented as a function of StO_2. However, enhanced sensitivity and linearity were achieved as shown in **Figure 6.13(b)**. At R = 0.61, WM-DPAS exhibited about 103.77° of linear signal change as StO_2 decreased from 94.7% to 74.6%. This number was significant in comparison to the single-ended results in **Figure 6.13(a)** in which the single-ended 680-nm and 808-nm measurements showed only 6.66° and 3.33° signal change, respectively, over the same range of *Hb* deoxygenation. Furthermore, this value became even more significant when it was compared to the differential phase result at dP = 180.08° in **Figure 6.11** which showed about 36° phase shift over a similar StO_2 range from ~95% to 74.6%.

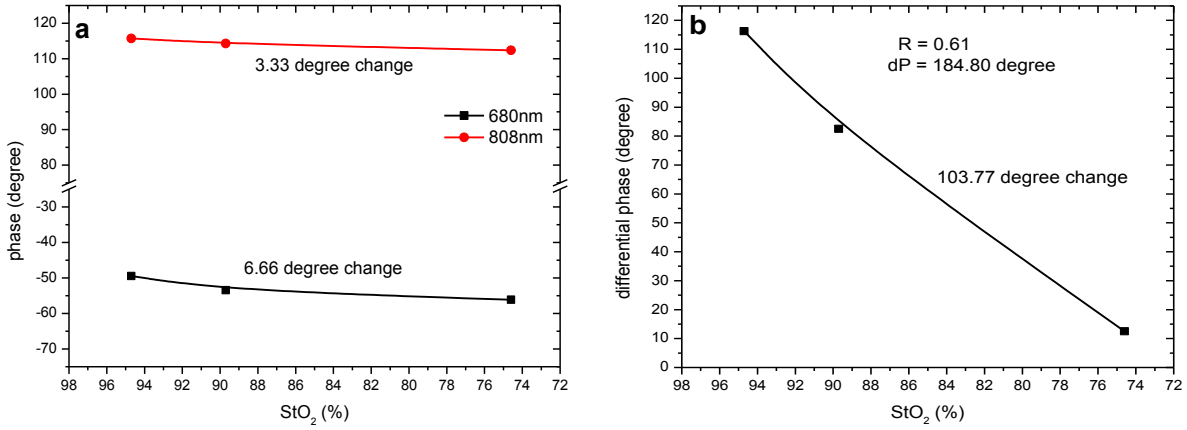

Figure 6.13 PA phase responses of **(a)** the single-ended and **(b)** differential measurements at R = 0.61 and dP = 184.80° over decreasing *Hb* oxygenation level. The differential system showed about 103.77° phase change at optimal R, 0.61, while the single-ended system showed only 6.66° (at 680-nm) and 3.33° (at 808-nm) phase changes as StO_2 decreased from 94.7% to 74.6%.

For the differential PA amplitude in **Figure 6.14(b)**, R = 0.91 was chosen as optimal since it showed the highest linearity and sensitivity (317.50% signal change) as StO_2 decreased from 94.7% to 74.6%. Such sensitivity was approximately 6.37 and 104.33 times better than the single-ended 680-nm and 808-nm signals respectively over the same range of *Hb* deoxygenation. However, when it was compared to the differential amplitude result at dP = 180.08° in **Figure 6.10(b)**, it exhibited decrease of ~10 folds in unit sensitivity per $\%StO_2$ and linearity. Therefore, it was observed that the differential amplitude signals are not optimal for sensitive malignancy

monitoring purposes when *dP* is adjusted away from 180°. A summary of the experimental results obtained at *dP* = 184.80° is provided in **Table 6.2**. The direct comparison between results at two different *dP* under the same *Hb* deoxygenation range is also made in **Table 6.3**.

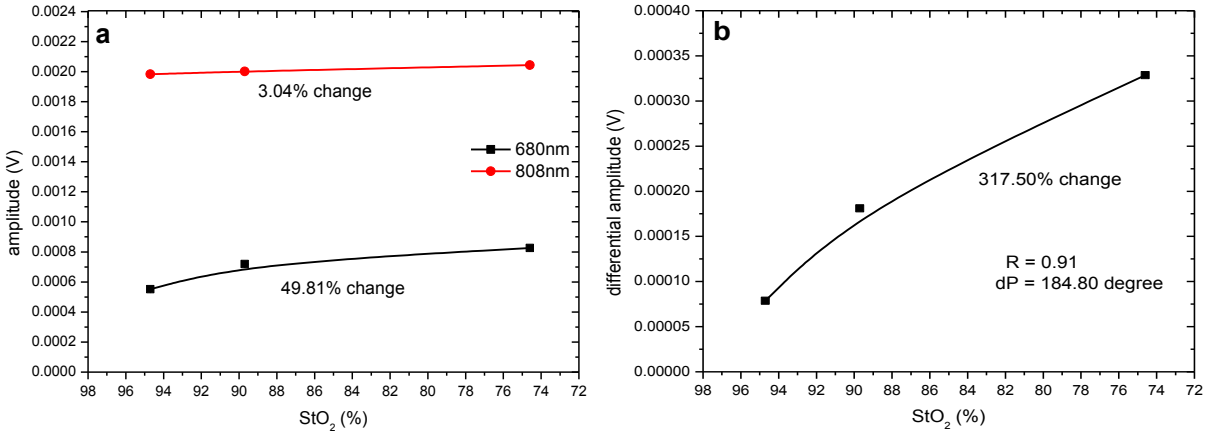

Figure 6.14 PA amplitude responses of **(a)** the single ended and **(b)** differential measurements at *R* = 0.91 and *dP* = 184.80° over decreasing *Hb* oxygenation level. The differential system showed improved sensitivity in comparison to the single-ended modes as StO_2 decreased from 94.7% to 74.6%.

Table 6.2 Differential signal analysis when *dP* ≈ 185°.

	differential phase	**680nm phase**	**808nm phase**	**differential amplitude**	**680nm amplitude**	**808nm amplitude**
Purpose	monitoring	x	x	monitoring	x	x
R	0.61	x	x	0.91	x	x
dP	184.80°	x	x	184.80°	x	x
PA signal change	103.77°	6.66°	3.33°	317.50%	49.81%	3.04%
***StO_2* range**	95%-75%	95%-75%	95%-75%	95%-75%	95%-75%	95%-75%
Unit PA signal change	5.19° /%StO_2	0.33° /%StO_2	0.17° /%StO_2	15.88% /%StO_2	2.49% /%StO_2	0.15% /%StO_2
Figure	**6.13(b)**	**6.13(a)**	**6.13(a)**	**6.14(b)**	**6.14(a)**	**6.14(a)**

Table 6.3 Differential signal sensitivity under various conditions.

	differential phase	**differential phase**	**differential amplitude**	**differential amplitude**
Purpose	monitoring	monitoring	monitoring	monitoring
R	0.61	0.40	0.91	0.97
dP	184.80°	180.08°	184.80°	180.08°
Unit PA signal change	5.19° /%StO_2	2.10° /%StO_2	15.88% /%StO_2	162.84% /%StO_2
Figure	**6.13(b)**	**6.11**	**6.14(b)**	**6.10(b)**

It was successfully demonstrated that the phase signal sensitivity and linearity could be enhanced to a great extent by adjusting the system *dP* away from 180°. Such enhancements provide the system with a greater capability for sensitive quantification of breast cancer carcinogenesis benchmarks which can be provided to clinicians or patients along with quick pre-malignancy screening tests. Fine optimization of the system *R* and *dP* in the future is expected to further improve the signal sensitivity and linearity for a more precise *Hb* parameter quantification.

6.2 Potential use of WM-DPAS: breast carcinogenesis characterization

As mentioned throughout this thesis, there is not yet a clear statistical agreement made for C_{Hb} and StO_2 values of the breast tissues at different health stages. For instance, looking at three independent studies summarized in **Table 6.4**, C_{Hb} values for healthy breast tissues from premenopausal women varied from 27 to 63μM [55, 60, 68]. However, one study found the C_{Hb} value for malignant breast tissues from a premenopausal woman to be 48μM which conflicts with the values from the abovementioned studies [56]. Furthermore, while the human breast optical parameters could vary considerably by a number of factors like menopausal status [13, 55, 60, 64], many studies have neglected such variables which makes their results even more unreliable [57, 62, 67, 72, 73]. The optical nature of breast tissues is complicated and therefore when it comes to accurately characterizing the optical properties of breast carcinogenesis, clinical studies should be carefully designed to incorporate all the heterogeneity factors of a human breast. For example, the health status of study participants can be sub-divided further based on their location of origin, cell grade, and even specific tumor stages.

Table 6.4 A list of non-invasive *in-vivo* breast tissue characterization study.

ref.	Status	Number of patient (pre- or post-menopausal)	C_{Hb} (μM)	StO_2 (%)	method
[55]	Healthy	15 (pre)	27±6	74±6	DOS
		13 (post)	14±4	75±8	
[56]	Healthy	1 (pre)	20±2	N/A	DOS+DCS
	Malignant	1 (pre)	48±7	N/A	
[57]	Healthy	6 (mixed)	4.13±1.9	77.9±7.9	NIRS
	Malignant	1 (N/A)	40±10	71±9	OM
[60]	Healthy	15 (pre)	40.4±2.7	68.9±1.3	OM
		7 (post)	14.4±1.9	83.7±2.5	
[62]	Healthy	50 (N/A)	34.76±17	87.39±4.78	DOS
	Pre-malignant	31 (N/A)	39.29±14.8	85.13±4.4	
	Malignant	9 (N/A)	26.56±20	86.22±10.4	
[64]	Healthy	24 (mixed)	22±8	58±9	DOS
[67]	Healthy	18 (N/A)	14±1	N/A	US guided OTI
	Pre-malignant	16 (N/A)	67±17	N/A	
	Malignant	2 (N/A)	119±1.6	N/A	
[68]	Healthy	1 (pre)	63±2	70±5	OTI
		1 (post)	22±2	67±7	
[70]	Healthy	1 (post)	16.1±1.8	73.9±8	DOS
	Malignant	1 (post)	41±3	68±8	
[71]	Healthy	1 (post)	21.8±3	82.1±2	MRI guided DOS
	Malignant	1 (post)	56±7	66±0.2	
[72]	Healthy	14 (N/A)	18±5	69±6	MRI guided DOS
	Pre-malignant	9 (N/A)	60±10	67±2	
	Malignant	5 (N/A)	130±100	60±9	
[73]	Healthy	5 (N/A)	N/A	70.8±1.7	DOS
	Malignant	118 (N/A)	N/A	69±5.3	

(DOS: diffuse optical spectroscopy, DCS: diffuse correlation spectroscopy, NIRS: NIR spectroscopy, OM: optical mammography, OTI: optical tomographic imaging)

In numerous independent studies, however, the trends of a monotonic increase in C_{Hb} and a monotonic decrease in StO_2 were clearly observed during breast carcinogenesis and many prominent researchers including Shah *et al* have successfully demonstrated C_{Hb}- or StO_2-based *in-vivo* breast tumor detection using optical spectroscopy modalities [29, 30, 43, 44, 56, 59, 62, 68-73]. In other words, the C_{Hb} and StO_2 values from different studies did not agree with each other, but most *in-vivo* optical studies individually confirmed the aforementioned trends during breast carcinogenesis as expected from the biological point of view [56, 57, 67, 70-73].

Therefore, it appears that today's technical modalities or approaches in general are limited to some degree in accurately quantifying C_{Hb} and StO_2.

In **section 6.1.3**, the capability of the developed WM-DPAS system to sensitively quantify C_{Hb} and StO_2 was experimentally demonstrated. As summarized in **Table 6.3**, when the system *R* and *dP* were tuned properly, the differential phase and amplitude signals showed ~5.19° and ~162.84% linear signal change over every % change in StO_2. Such enhanced sensitivity is outstanding when it is compared to the other non-invasive techniques that have been mainly used for the quantitative measurement of StO_2 as described in **Table 6.5**. Additionally, instead of relying on the single amplitude channel like the existing modalities, the WM-DPAS system utilizes two complementary amplitude and phase channels, further enhancing reliability of C_{Hb} and StO_2 measurements. They can be further optimized in the future, followed by appropriate clinical studies, which should consider the heterogeneity of a human breast, so as to accurately characterize and quantify those controversial breast carcinogenesis parameters.

Table 6.5 Signal sensitivity comparison of various non-invasive StO_2 quantification modalities.

ref.	method	channel	Unit signal change	target
This study	WM-DPAS; CW laser with 680-nm and 808-nm diodes	amplitude	**162.84%** /%StO_2	*In-vitro* sheep blood
		phase	**5.19°** /%StO_2	
[102]	PACT; pulsed laser with 680-nm modulation	amplitude	2.51% /%StO_2	*In-vivo* mouse
[103]	PAS; pulsed laser with 760-nm modulation	amplitude	1.06% /%StO_2	*In-vivo* human blood
[110]	PAM; pulsed laser with 570-nm modulation	amplitude	0.12% /%StO_2	*In-vivo* Phantom (cornstarch + gelatin)
[111]	Optical sensor with 665-nm LED emission	amplitude	2.86% /%StO_2	*In-vivo* rat and cow blood

(PACT: photoacoustic-computed tomography, PAS: photoacoustic spectroscopy, PAM: photoacoustic microscopy)

6.3 Conclusions

The new modality, WM-DPAS, experimental realization was implemented with an *in-vitro* sheep blood circulation system and corresponding experimental results were presented. The pre-malignancy screening capability of the WM-DPAS system was demonstrated: when the system dP is set close to 180°, R can be arbitrarily tuned so that the differential phase varies sensitively near the pre-malignancy region. At the same dP close to 180°, the novel tunability of the system allowed both the differential amplitude and phase signals to be used independently for StO_2 quantification purpose as well with great sensitivity. Furthermore, when the system dP was tuned slightly away from 180°, enhancement in sensitivity and linearity were observed particularly in differential phase at its optimal R. These two complementary channels, the differential amplitude when dP close to 180° and the differential phase when dP away from 180°, can be used together to sensitively quantify the breast tumor carcinogenesis benchmarks with high degree of reliability.

The tunability of the WM-DPAS system must be emphasized. As described throughout this chapter, conventional single-ended methodologies did not provide any flexibility between cancer detection and monitoring. Once developed into a portable clinical device, the WM-DPAS system R and dP can be easily tuned to provide both quick pre-malignancy screening and the actual values of C_{Hb} and StO_2 whenever necessary.

Chapter 7

Summary

In this thesis, the introduction of WM-DPAS was theoretically and experimentally investigated for early breast tumor detection and carcinogenesis monitoring. The WM-DPAS modality is unique with its tunability feature in that the system parameters (*R* and *dP*) can be arbitrarily adjusted to meet a variety of clinical needs.

As an extension of the existing FD-PAR system, the WM-DPAS uses low power CW optical sources at specific wavelengths. Two wavelengths, 680-nm and 808-nm, were chosen based on the *Hb* extinction coefficient spectrum to sensitively screen or monitor the *Hb* parameters for early breast tumor detection. Since they utilize the same instrumentation, the developed WM-DPAS system is expected to be easily co-registered with the existing FD-PAR imager, enhancing one another's sensitivity and specificity further.

Upon the development of the WM-DPAS theoretical formalism, the single-ended PA signals were analyzed first to validate the model under various conditions. The initial WM-DPAS *in-vitro* experiments followed and successfully demonstrated its great sensitivity and specificity for early breast tumor detection and malignancy monitoring.

In the experiments, optical waveforms were usually modulated by square-waveform at 0.3-MHz since it showed the highest SNR. However, higher modulation frequency (> 1-MHz) needs to be achieved in the future for improved tumor imaging axial and spatial resolution. The system must be optimized in terms of reducing or removing the RF noises at high optical modulation frequencies to keep the SNR high. With the optimized system, a corresponding animal study can be followed to demonstrate WM-DPAS's capability of sensitive pre-malignancy detection in *in-vivo* setting.

As suggested in **Chapter 6**, the WM-DPAS may also be used to accurately characterize C_{Hb} and StO_2 at different stages of breast cancer. While it appears that today's technical modalities or approaches in general are inadequate for accurate characterization of breast carcinogenesis

parameters, the WM-DPAS system was able to do so with outstanding sensitivity. Appropriate clinical studies, which carefully consider heterogeneity factors of a human breast, can be designed and followed using the developed WM-DPAS modality to accurately characterize those controversial breast carcinogenesis parameters.

References

[1] P. Beard, "Biomedical photoacoustic imaing," *Interface Focus*, **1**, 601 – 631 (2011).

[2] M. Xu and L. V. Wang, "Photoacoustic imaging in biomedicine," *Rev. Sci. Instrum.,* **77**, 041101 (2006).

[3] V. Ntziachristos, J. Ripoll, L. V. Wang, and R. Wiessleder, "Looking and listening to light: the evolution of whole-body photonic imaging," *Nat. Biotechnol.,* **23**, 313 – 320 (2005).

[4] V. E. Gusev and A. A. Karabutov, *Laser Optoacoustics*. New York: AIP, 1993.

[5] A. G. Bell, "On the production and reproduction of sound by light," *Am, J. Sci.,* **20**, 305 – 324 (1880).

[6] J. Tyndall, "Action of an intermittent beam of radiant heat upon gaseous matter," *Proc.R. Soc.,* **31**, 307 – 317 (1881).

[7] T. H. Maiman, "Stimulated optical radiation in Ruby," *Nature,* **187**, 493 – 494 (1960).

[8] E. L. Kerr and J. G. Atwood, "The laser illuminated absorptivity spectrophone: a method for measurement of weak absorptivity in gases at laser wavelengths," *Appl. Opt*., **7**, 915 – 921 (1968).

[9] A. C. Tam, "Applications of photoacoustic sensing techniques," *Rev. Mod. Phys.,* **58**, 381 – 431 (1986).

[10] D. C. Fork and S. K. Herbert, "The application of photoacoustic techniques to studies of photosynthesis," *Photochem. Photobiol.,* **57** (1), 207 – 220 (1993).

[11] F. Gosselin, M. D. Renzo, T. H. Ellis, and W. D. Lubell, "Photoacoustic FTIR spectroscopy, a non-destructive method for sensitivie analysis of solid-phase organic chemistry," *J. Org. Chem.,* **61**, 7980 – 7981 (1996).

[12] F. A. McDonald, "Photoacoustic effect and the physics of waves," *Am. J. Phys.,* **48** (1), 41 – 47 (1980).

[13] S. Thomsen and D. Tatman, "Physiological and Pathological Factors of Human Breast Disease That Can Influence Optical Diagnosis," *Ann. N. Y. Acad. Sci.,* **838**, 171 – 193 (1998).

[14] P. J. Stephens, D. J. McBride, M. L. Lin, I. Varela, E. D. Pleasance, J. T. Simpson, L. A. Stebbings, C. Leroy, S. Edkins, L. J. Mudie, C. D. Greenman, M. Jia, C. Latimer, J. W. Teague, K. W. Lau, J. Burton, M. A. Quail, H. Swerdlow, C. Churcher, R. Natrajan, A. M. Sieuwerts, J. W. Martens, D. P. Silver, A. Langerod, H. E. Russnes, J. A. Foekens, J. S. Reis-Filho, L. van'tVeer, A. L. Richardson, A. L. Borresen-Dale, P. J. Campbell, P. A. Futreal and M. R. Stratton, "Complex landscapes of somatic rearrangement in human

breast cancer genomes," *Nature,* **462** (7276), 1005–1010 (2009).

[15] M. J. Higgins and J. Baselga, "Targeted therapies for breast cancer," *J. Clin. Invest*., **121** (10), 3797 – 3803 (2011).

[16] L. L. Campbell and K. Polyak, "Breast Tumor Heterogeneity: Cancer Stem Cells or Clonal Evolution?" *Cell Cycle*, **6** (19), 2332 – 2338 (2007).

[17] K. Polyak, "Heterogeneity in breast cancer," *J. Clin. Invest.,* **121** (10), 3786 – 3788 (2011).

[18] H. J. G. Bloom and W. W. Richardson, "Histological grading and prognosis in breast cancer: A study fo 1409 cases of which 359 have been followed for 15 years," *Br. J. Cancer*., **11** (3), 359 – 377 (1957).

[19] H. Fujii, R. Szumel, C. Marsh, W. Zhou and E. Gabrielson, "Genetic progression, histological grade, and allelic loss in ductal carcinoma in situ of the breast," *Cancer. Res*., **56**, 5260 – 5265 (1996).

[20] R. Yancik, L. G. Ries and J. W. Yates, "Breast cnacner in aging women. A population-based study of contrasts in stage, surgery, and survival," *Cancer*, **63** (5), 976 – 981 (1989).

[21] C. M. Mansfield, L. T. Komarnicky, G. F. Schwartz, A. L. Rosenberg, L. Krishnan, W. R. Jewell, F. E. Roasto, M. L. Moses, M. Haghbin and J. Taylor, "Ten-year results in 1070 patients with stages I and II breast cancer treated by conservative surgery and radiation therapy," *Cancer*, **75** (9), 2328 – 2336 (1995).

[22] M. Omne-Pontén, L. Holmber and P. O. Sjödén, "Psychosocial adjustment among women with breast cancer stages I and II: six-year follow-up of consecutive patients," *J. Clin. Oncol.,* **12** (9), 1778 – 1782 (1994).

[23] C. I. Li, K. E. Malone and J. R. Daling, "Differences in breast cancer stage, treatment and survival by race and ethinicity," *Arch. Inter. Med.,* **163** (1), 49 – 56 (2003).

[24] D. C. Allred and S. K. Mohsin, "Biological Features of Premalignant Disease in the Human Breast," *J. Mammary Gland Biol*., **5** (4), 351 – 364 (2000).

[25] G. Arpino, R. Laucirica, and R. M. Elledge, "Premalignant and In Situ Breast Disease: Biology and Clinical Implications," *Ann. Intern. Med.*, **143**, 446 – 457 (2005).

[26] D. C. Allred, S. K. Mohsin, and S. A. W. Fuqua, "Histological and biological evolution of human premalignant breast disease," *Endocr-relat. Cancer*, **8**, 47 – 61 (2001).

[27] G. N. Hortobagyi, F. C. Ames, A. U Buzdar, S. W. Kau, M. D. McNeese, D. Paulus, V. Hug, F. A. Holmes, M. M. Romsdahl, G. Fraschini, C. M. McBridge, R. G. Martin and E. Montague, "Management of Stage III Primary Breast Cancer With Primary Chemotherapy, Surgery, and Radiation Therapy," *Cancer*, **62**, 2507 – 2516 (1988).

[28] B. Fisher, J. Bryant, N. Wolmark, E. Mamounas, A. Brown, E. R. Fisher, D. L.

Wickerham, M. Begovic, A. DeCillis, A. Robidoux, R. G. Margolese, A. B. Cruz, J. L. Hoehn, A. W. Lees, N. V. Dimitrov and H. D. Bear, "Effect of preoperative chemotherapy on the outcome of women with operable breast cancer," *J. Colin. Oncol.,* **16** (8), 2672 – 2685 (1998).

[29] V. R. Kondepati, H. M. Heise and J. Backhaus, "Recent applications of near-infrared spectroscopy in cancer diagnosis and therapy," *Anal. Bioanal. Chem*., **390**, 125- 139 (2008).

[30] R. L. P. Veen, H. J. C. M. Sterenborg, A. W. K. S. Marinelli, and M. Menke-Pluymers, "Intraoperatively assessed optical properties of malignant and healthy breast tissue used to determine the optimum wavelength of contrast for optical mammography," *J. Biomed. Opt.,* **9** (6), 1129 – 1136 (2004).

[31] American Cancer Society, *Cancer Facts & Figures 2014*, Atlanta: American Cancer Society (2014).

[32] B. Nettles-carlson, "Early Detection of Breast Cancer," *J. Obstet. Gynecol. Neonatal. Nurs.,* **18**, 373–381 (1989).

[33] F. Aaron and D. B. Downey, "3-D ultrasound imaging: A review," *IEEE. Eng. Med. Biol.,* **15** (6), 41 – 51 (1996).

[34] A. Karellas and S. Vedantham, "Breast cancer imaging: A perspective for the next decade," *Med. Phys*., **35** (11), 4878 – 4889 (2008).

[35] F. A. Duck, *Physical Properties of Tissue: A Comprehensive Reference Book*. New York: Academic Press (1990).

[36] World Health Organization, *Training in Diagnostic Ultrasound: Essentials, Principles and Standards*, WHO Technical Report Series 875 (1998).

[37] R. Damadian, "Tumor detection by nuclear magnetic resonace," *Science*, **171** (3976), 1151 – 1153 (1971).

[38] S. J. El Yousef, R. J. Alfidi, R. H. Duchesneau, C. A. Hubay, J. R. Haaga, P. J. Bryan, J. P. LiPuma, and A. E. Ament, "Initial experience with nuclear magnetic resonance NMR imaging of the human breast," *J. Comput. Assist. Tomogr.* **7** (2), 215 – 218 (1983).

[39] R. J. Ross, J. S. Thompson, K. Kim, and R. A. Bailey, "Nuclear magnetic resonance imaging and evaluation of human breast tissue: preliminary clinical trials," *Radiology*, **143** (1), 195 – 205 (1982).

[40] C. K. Kuhl, S. Schrading, C. C. Leutner, N. Morakkabati-Spitz, E. Wardelmann, R. Fimmers, W. Kuhn, and H. H. Schild, "Mammography, Breast Ultrasound, and Magnetic Resoance Imaging for Surveillance of Woman at High Familial Risk for Breast Cancer," *J. Clin. Oncol.,* **23** (33), 8469 – 8476 (2005).

[41] N. H. Peters, I. H. Borel Rinkes, N. P. Zuithoff, W. P. Mali, K. G. Moons, and P. H. Peeters, "Meta-analysis of MR imaging in the diagnosis of breast lesions," *Radiology*, **246** (1), 116 – 124 (2008).

[42] D. Saslow, C. Boetes, W. Burke, S. Harms, M. O. Leach, C. D. Lehman, E. Morris, E. Pisano, M. Schnall, S. Sener, R. A. Smith, E. Warner, M. Yaffe, K. S. Andrews, and C. A. Russell, "American Cancer Society guidelines for breast screening with MRI as an adjunct to mammography," *Ca-Cancer J. Clin.,* **57** (2), 75 – 89 (2007).

[43] J. Wang, S. Jiang, Z. Li, R. M. diFlorio-Alexander, R. J. Barth, P. A. Kaufman, B. W. Pogue, and K. D. Paulsen, "*In vivo* quantitative imaging of normal and cancerous breast tissue using broadband diffuse optical tomography," *Med. Phys*., **37** (7), 3715 – 3723 (2010).

[44] V. Ntziachristos and B. Chance, "Probing physiology and molecular function using optical imaging: applications to breast cancer," *Breast Cancer Res,* **3**, 41 – 46 (2001).

[45] R. Choe, S. D. Konecky, A. Corlu, K. Lee, T. Durduran, D. R. Busch, S. Pathak, B. J. Czerniecki, J. Tchou, D. L. Fraker, A. DeMichele, B. Chance, S. R. Arridge, M. Schweiger, J. P. Culver, M. D. Schnall, M. E. Putt, M. A. Rosen, and A. G. Yodh, "Differentiation of benign and malignant breast tumours by in-vivo three-dimensional parallel-plate diffuse optical tomography," *J. Biomed. Opt.* **14** (2), 024020 (2009).

[46] A. G. Yodh and B. Chance, "Spectroscopy and imaging with diffusing light," *Phys. Today*, **48**, 34 – 40 (1995).

[47] R. L. Egan, "Experience with mammography at a tumor institution," *Am. J. Roentgenol.* **75**, 894 – 900 (1960).

[48] S. Ganai and D. J. Winchester, "Screening mammography," *Cancer,* **117** (4), 3062 – 3063 (2011).

[49] E. L. Thurfjell and J. A. Lindgren, "Breast cancer survival rates with mammographic screening: similar favorable survival rates for women younger and those older than 50 years," *Radiology,* **201** (2), 421 – 426 (1996).

[50] L. Taber, B. Vitak, H. H. Chen, M. F. Yen, S. W. Duffy, and R. A. Smith, "Beyond randomized controlled trials: organized mammographic screening substantially reduces breast carcinoma mortality," *Cancer*, **91** (9), 1724 – 1731 (2001).

[51] N. T. Brewer, T. Salz, and S. E. Lillie, "Systematic review: the long-term effects of false-positive mammograms," *Ann. Intern. Med.,* **146** (7), 502 – 510 (2007).

[52] S. Telenkov, A. Mandelis, B. Lashkari, and M. ForchtJ, "Frequency-domain photothermoacoustics: Alternative imaging modality of biological tissues", *Appl. Phys.,* **105**, 102029 (2009).

[53] R. A. Kruger, D. R. Reinecke, and G. A. Kruger, "Thermoacoustic computed tomography-technical considerations," *Med. Phys*., **26**, 1832 – 1837 (1999).

[54] C. G. A. Hoelen and F. F. M. de Mul, "Image Reconstruction for Photoacoustic Scanning of Tissue Structures," *Appl. Opt.,* **39** (31), 5872 – 5883 (2000).

[55] N. Shah, A. E. Cerussi, D. Jakubowski, D. Hsiang, J. Butler, and B. J. Tromberg, "Spatial variations in optical and physiological properties of healthy breast tissue," *J. Biomed. Opt.,* **9** (3), 534 – 540 (2004).

[56] C. Zhou, R. Choe, N. Shah, T. Durduran, G. Yu, A. Durkin, D. Hsiang, R. Mehta, J. Butler, A. Cerussi, B. J. Tromberg, and A. G. Yodh, "Diffuse optical monitoring of blood flow and oxygenation in human breast cancer during early stages of neoadjuvant chemotherapy," *J. Biomed. Opt.,* **12** (5), 051903 (2007).

[57] S. Fantini, S. A. Walker, M. A. Franceschini, M. Kaschke, P. M. Schlag, and K. T. Moesta, "Assessment of the size, position, and optical properties of breast tumors *in vivo* by noninvasive optical methods," *Appl. Opt.* **37**, 1982 – 1989 (1998).

[58] B. J. Tromberg, N. Shah, R. Lanning, A. Cerussi, J. Espinoza, T. Phan, L. Svaasand, and J. Butler, "Non-invasive in vivo characterization of breast tumors using photon migration spectroscopy," *Neoplasia*. **2**, 1 – 15 (2000).

[59] B. Chance, S. Nioka, J. Zhang, E. F. Conant, E. Hwang, S. Briest, S. G. Orel, M. D. Schnall, and B. J. Czerniecki, "Breast cancer detection based on incremental biochemical and physiological properties of breast cancer: a six-year, two-site study," *Acad. Radiol.* **12**, 925 – 933 (2005).

[60] A. E. Cerussi, A. J. Berger, F. Bevilacqua, N. Shah, D. Jakubowski, J. Butler, R. F. Holcombe, B. J. Tromberg, "Sources of Absorption and Scattering Contrast for Near-Infrared Optical Mammography," *Acad. Radiol.,* **8**, 211 – 218 (2001).

[61] P. Vaupel, K. Schlenger, C. Knoop and M. Hockel, "Oxygenation of Human Tumors: Evaluation of Tissue Oxygen Distribution in Breast Cancers by Computerized O2 Tension Measurements," *Cancer Res*., **51**, 3316 – 3322 (1991).

[62] X. Cheng, J. Mao, D. B. Kopans, R. H. Moore and M. Chorlton, "Breast cancer detection by mapping hemoglobin concentration and oxygen saturation," *Appl. Optics*, **42** (31), 6412 – 6421 (2003).

[63] F. Hu, K. Vishwanath, J. Lo, A. Erkanli, C. Mulvey, W. T. Lee and N. Ramanujam, "Rapid Determination of Oxygen Saturation and Vascularity for Cancer Detection," *PLoS. ONE*, **8** (12): e82977 (2013).

[64] S. Srinivasan, B. W. Pogue, S. Jiang, H. Dehghani, C. Kogel, S. Soho, J. J. Gibson, T. D. Tosteson, S. P. Poplack and K. D. Paulsen, "Interpreting hemoglobin and water concentration, oxygen saturation, and scattering measured in vivo by near-infrared breast tomography," *P. Natl. A. Sci. USA*., **100** (21), 12349 – 12354 (2003).

[65] D. Grosenick, H. Wabnitz, K. T. Moesta, J. Mucke, M. Moller, C. Stroszczynski, J. Stobel, B. Wassermann, P. M. Schlag and H. Rinneberg, "Concentration and oxygen

saturation of haemoglobin of 50 breast tumours determined by time-domain optical mammography," *Phys. Med. Biol*., **49**, 1165 – 1181 (2004).

[66] H. Jiang, N. V. Iftimia, Y. Xu, J. A. Eggert, L. L. Fajardo and K. L Klove, "Near-Infrared Optical Imaging of the Breast with Model-based Reconstruction," *Acad. Radiol*., **9**, 186 – 194 (2002).

[67] Q. Zhu, M. Huang, N. Chen, K. Zarfos, B. Jagjivan, M. Kane, P. Hedge and S. H. Kurtzman, "Ultrasound-Guided Optical Tomographic Imaging of Malignant and Benign Breast Lesions: Initial Clinical Results of 19 Cases," *Neoplasia*, **5**, 379 – 388 (2003).

[68] T. O. McBridge, B. W. Pogue, E. D. Gerety, S. B. Poplack, U. L. Osterberg and K. D. Paulsen, "Spectroscopic diffuse optical tomography for the quantitative assessment of hemoglobin concentration and oxygen saturation in breast tissue," *Appl. Optics*, **38** (25), 5480 – 5490 (1999).

[69] H. Dehghani, B. W. Pogue, S. P. Poplack and K. D. Paulsen, "Multiwavelength three-dimensional near-infrared tomography of the breast: initial simulation, phantom, and clinical results," *Appl. Optics*, **42** (1), 135 – 145 (2003).

[70] D. B. Jakubowski, A. E. Cerussi, F. Bevilacqua, N. Shah, D. Hsiang, J. Butler and B. J. Tromberg, "Monitoring neoadjuvant chemotherapy in breast cancer using quantitative diffuse optical spectroscopy: a case study," *J. Biomed. Opt*., **9** (1), 230 – 238 (2004).

[71] N. Shah, J. Gibbs, D. Wolverton, A. Cerussi, N. Hylton and B. J. Tromberg, "Combined diffuse optical spectroscopy and contrast-enhanced magnetic resonance imaging for monitoring breast cancer neoadjuvant chemotherapy: a case study," *J. Biomed. Opt*., **10** (5): 051503-1 (2005).

[72] V. Ntziachristos, A. G. Yodh, M. D. Schnall and B. Chance, "MRI-Guided Diffuse Optical Spectroscopy of Malignant and Benign Breast Lesions," *Neoplasia*, **4** (4), 347 – 354 (2002).

[73] N. Nakamiya, S. Ueda, T. Shigekawa, H. Takeuchi, H. Sano, E. Hirokawa, H. Schimada, H. Suzuki, M. Oda, A. Osaki and T. Saeki, "Clinicopathological and progonostic impact of imaging of breast cancer angiogenesis and hypoxia using diffuse optical spectroscopy," *Cancer Sci*., **105** (7), 833 – 839 (2014).

[74] S. B. Fox, D. G. Generali, and A. L. Harris, "Breast tumour angiogenesis," *Breast Cancer Res*., **9** (6), 216 (2007).

[75] B . P. Schneider and K. D. Miller, "Angiogenesis of Breast Cancer," *J. Clin. Oncol.,* **23** (8), 1782 – 1790 (2005).

[76] J. Folkman, "Tumor angiogenesis: therapeutic implications," *N. Engl. J. Med.,* **285**, 1182 – 1186 (1971).

[77] G. Deng, Y. Lu, G. Zlotnikov, A. Thor, and H. S. Smith, "Loss of heterozygosity in normal tissue adjacent to breast carcinomas," *Science*, **274**, 2057 – 2059 (1996).

[78] A. Guidi, L. Fischer, J. Harris, and S. Schnitt, "Microvessel density and distribution in ductal carcinoma in situ of the breast," *J. Natl. Cancer. Inst*., **86**, 614 – 619 (1994).

[79] R. Splinter and B. A. Hooper, *An Introduction to Biomedical Optics*. Boca Raton: CRC press (2006).

[80] P. LeBoulluec, H. Liu, and B. Yuan, "A cost-efficient frequency-domain photoacoustic imaging system," *Am. J. Phys.*, **81**, 712 – 717 (2013).

[81] American National Standard, ANSI Z136.1-1993

[82] T. J. Allen, E. Z. Zhang, J. G. Laufer, P. C. Beard, "Use of a pulsed fiber laser as an excitation source for photoacoustic tomography," *Proc. SPIE,* **7899**, 78991V (2011).

[83] S. Telenkov, R. Alwi, A. Mandelis, W. Shi, E. Chen and A. Vitkin, "Frequency domain photoacoustic correlation (radar) imaging: a novel methodology for non-invasive imaging of biological tissues," *Proc. of SPIE,* **8223***,* 82231J (2012).

[84] Y. Fan, A. Mandelis, G. Spirou, I. A. Vitkin, "Development of a laser photothermoacoustic frequency-swept system for subsurface imaging: theory and experiment," *J. Accoust. Soc. Am.,* **116** (6), 3523 – 3533 (2004).

[85] S. Telenkov and A. Mandelis, "Fourier-domain biophotoacoustic subsurface depth selective amplitude and phase imaging of turbid phantoms and biological tissue," *J. Biomed. Opt.,* **11** (4), 044006 (2006).

[86] S. Telenkov and A. Mandelis, "Signal-to-noise analysis of biomedical photoacoustic measurements in time and frequency domains," *Rev. Sci. Instrum*., **81**, 124901 (2010).

[87] S. Telenkov and A. Mandelis, "Photoacoustic Sonar: Principles of operation, imaging and signal-to-noise analysis in time and frequency domains," *Proc. of SPIE*, **7899**, 78990Y-1 (2011).

[88] S. Telenkov and A. Mandelis, "Photothermoacoustic imaging of biological tissues: maximum depth characterization comparison of time and frequency-domain measurements," *J. Biomed. Opt.*, **14** (4), 044025 (2009).

[89] S. Telenkov, R. Alwi, and A. Mandelis, "Photoacoustic correlation signal-to-noise ratio enhancement by coherent averaging and optical waveform optimization," *Rev. Sci. Instrum.*, **84**, 104907 (2013).

[90] B. Lashkari and A. Mandelis, "Comparison between pulsed laser and frequency-domain photoacoustic modalities: Signal-to-noise ratio, contrast, resolution, and maximum depth detectivity," *Rev. Sci. Instrum*., **82**, 094903 (2011).

[91] B. Lashkari and A. Mandelis, "Linear frequency modulation photoacoustic radar: Optimal bandwidth and signal-to-noise ratio for frequency-domain imaging of turbid media," *J. Acoust. Soc. Am.*, **130** (3), 1313 – 1324, (2011).

[92] S. Telenkov, R. Alwi, A. Mandelis, and A. Worthington, "Frequency-domain photoacoustic phased array probe for biomedical imaging application," *Opt. Lett*., **36** (23), 4560 – 4562 (2011).

[93] C. E. Cook and M. Bernfeld, *Radar Signals: an Introduction to Theory and Application.* Boston: Artech House (1993).

[94] V. Zharov and V. Letokhov, *Laser Optoacoustic Spectroscopy.* Berline: Springer-Verlag (1986).

[95] R. Alwi, "Biophotoacoustic Radar: Study of Tissue Phantoms, Tissues, Contrast Agent and Comparison to Ultrasound Imaging for Deep Subsurface Imaging," *M.A.Sc thesis*, University of Toronto (2012).

[96] R. Cubeddu, A. pifferi, P. Taroni, A. Torricelli and G. Valentini, "A solid tissue phantom for photon migration studies," *Phys. Med. Biol.,* **42,** 1971 – 1979 (1997).

[97] K. Zell, J. I. Sperl, M. W. Vogel, R. Niessner and C. Haisch, "Acoustical properties of selected tissue phantom materials for ultrasound imaging," *Phys. Med. Biol*., **52**, N475 – N484 (2007).

[98] M. E. Komlosh, F. Horkay, R. Z. Freidlin, U. Nevo, Y. Assaf and P. J. Basser, "Detection of microscopic anisotropy in gray matter and in a novel tissue phantom using double Pulsed Gradient Spin Echo MR," *J. Magn. Reson.,* **189** (1), 38 – 45 (2007).

[99] H. Wang, J. Jiang, C. Lin, J. Lin, G. Huang and J. Yu, "Diffuse reflectance spectroscopy detects increased hemoglobin concentration and decreased oxygenation during colon carcinogenesis from normal to malignant tumors," *Opt. Express*, **17** (4), 2805 – 2817 (2009).

[100] A. Roggan, M. Friebel, K. Dörschel, A. Hahn and G. Müller, "Optical Properties of Circulating Human Blood in the Wavelength Range 400 – 2500 nm," *J. Biomed. Opt.*, **4** (1), 36 – 46 (1999).

[101] J. P. Ritz, A. Roggan, C. T. Germer, C. Isbert, G. Müller and H. J. Buhr, "Continuous Changes in the Optical Properties of Liver Tissue During Laser-Induced Interstitial Thermotherapy," *Laser. Surg. Med.,* **28**, 307 – 312 (2001).

[102] J. Xia, A. Danielli, Y. Liu, L. Wang, K. Maslov and L. V. Wang, "Calibration-free quantification of absolute oxygen saturation based on the dynamics of photoacoustic signals," *Opt. Lett.,* **38** (15), 2800 – 2803 (2013).

[103] J. Laufer, D. Delpy, C. Elwell and P. Beard, "Quantitative spatially resolved measurement of tissue chromophore concentration using photoacoustic spectroscopy: application to the measurement of blood oxygenation and haemoglobin concentration," *Phys. Med. Biol.,* **52**, 141 – 168 (2007).

[104] P. O'Connell, V. Pekkel, S. A. W. Fuqua, C. K. Osborne, G. M. Clark and D. C. Allred, "Analysis of Loss of Heterozygosity in 399 Premalignant Breast Lesions at 156 Genetic Loci," *J. Natl. Cancer I.,* **90** (9), 697 – 703 (1998).

[105] S. Choi, A. Mandelis, X. Guo, B. Lashkari, S. Kellnberger and V. Ntziachristos, "Wavelength-Modulated Differential Photoacoustic Spectroscopy (WM-DPAS) for noninvasive early cancer detection and itssue hypoxia monitoring," (to be submitted).

[106] S. Choi, A. Mandelis, X. Guo, B. Lashkari, S. Kellnberger and V. Ntziachristos, "Wavelength-modulated Differential Photoacoustic Spectroscopy (WM-DPAS): Theory of a High-sensitivity Methodology For The Detection of Early-stage Tumors In Tissue," *Int. J. Thermophys.*, doi: 10.1007/s10765-014-1710-5 (2014).

[107] L. V. Wang and H. Wu, *Biomedical Optics: Principles and Imaging*. Hoboken: Wiley& Sons (2007).

[108] B. Lashkari, S. Choi, M. E. Khosroshahi, E. Dovlo and A. Mandelis, "Simultaneous Dual-wavelength Photoacoustic Radar Image Generation Using Waveform Engineering with Mismatched Frequency Modulated Excitation," *Opt. Lett.* (To be submitted).

[109] K. Briley-Sæbø and A. Bjørnerud, "Accurate de-oxygenation of ex-vivo whole blood using sodium dithionite," *Proc. Intl. Soc. Mag. Reson. Med*., **8**, 2025 (2000).

[110] Y. Jiang, A. Forbrich, T. Harrison and R. J. Zemp, "Blood oxygen flux estimation with a combined photoacoustic and high-frequency ultrasound microscopy system: a phantom study," *J. Biomed. Opt.*, **17** (3), 036012 (2012).

[111] K. Kwon and S. Park, "An optical sensor for the non-invasive measurement of the blood oxygen saturation of an artificial heart according to the variation of hematocrit," *Sensor. Actuator*., **43**, 49 – 54 (1994).

[112] G. M. Spirou, A. A. Oraevsky, I. A. Vitkin, W. M. Whelan, "Optical and acoustical properties at 1064 nm of polyvinyl chloride-plastisol for use as a tissue phantom in biomedical optoacoustics," *Phys. Med. Biol.* **50**, N141-N153 (2005).

[113] W. G. Zijlstra, A. Buursma and O. W. van Assendelft, *Visible and Near Infrared Absorption Spectra of Human and Animal Haemoglobin: Determination and Application*. Boston: VSP (2000).

Appendix 1

PVCP phantom preparation

A phantom that optically simulates human breast tissue is prepared using an oil-based liquid called Polyvinyl chloride plastisol (PVCP; M-F Manufacturing Co., TX, USA). Phantom absorption (μ_a) and reduced optical scattering (μ_s') coefficients can be arbitrarily adjusted using liquid black plastisol color (BPC; M-F Manufacturing Co., TX, USA) and Titanium dioxide (TiO_2) power (Sigma Aldrich, MO, USA) respectively. The phantom preparation procedure follows below:

1. Pour a proper amount of PVCP, BPC, and TiO_2 power to the foil dish based on the desired optical properties of the phantom [112].
   - $\mu_a = (12.818 \pm 0.001)A_{BPC}\text{-cm}^{-1}$ where A_{BPC} is the BPC percent volume concentration.
   - $\mu_s' = (2.6 \pm 0.2)S_{TiO_2} + (1.4 \pm 0.1)\text{-cm}^{-1}$ where S_{TiO_2} is the TiO_2 volume concentration in mg/mL.
2. Continuously stir the solution with a glass rod for 10 minutes to ensure solution homogeneity.
3. Place the foil dish containing the mixed solution on the electric heating plate (03403-30; Cole-Parmer Instrument Company, IL, USA). Turn on the heat at 7-7.5.
4. Constantly swirl the heating solution with a glass rod for 25 minutes.
5. After two phase changes, the final solution can be poured into the pre-made mold.
   - original oily liquid → intermediate jelly → final liquid
   - A mold can be easily made based on one's needs using generic aluminum sheets.
   - Other materials like a glass bowl can also be used as a mold.
6. At the desired depth, stop pouring the solution and let it solidifies for about 5 minutes. Then put the pre-made inclusions with higher absorption coefficients. Fill the rest part of the mold with the solution to cover up the inclusions.
   - Pour the solution slowly to avoid creating any air bubbles.
7. Allow it to cool down and let it solidify for 10 minutes before use. An example of the final phantom is shown in **Figure 2.2**.

Appendix 2

WM-DPAS experimental set-up optimization

In the WM-DPAS experimental set-up depicted in **Figure 4.3**, the angle between the laser beam and the transducer was observed to affect the system SNR to a great degree; therefore it needed to be optimized.

The 808-nm laser (LLS8800; Laser Light Solution, NJ, USA) was directed to the black anodized metal by the protected silver mirror (PF10-03-P01; Thorlabs, NJ, USA). A single-element 1.0-MHz focused ultrasonic transducer (V314; Olympus Panametrics, CA, USA) was scanned at 5 different angles (20°, 35°, 50°, 75° and 90°) at fixed 1.9 inch focal distance from the metal. The laser was sinusoidal chirp modulated in the range of 0.3 to 1.2-MHz and laser power was set at 2.4A. The received signals were analyzed in the same way as described in **section 2.2.2** using a matched filter cross-correlation processing algorithm. The experimental set-up is depicted in **Figure A.1**.

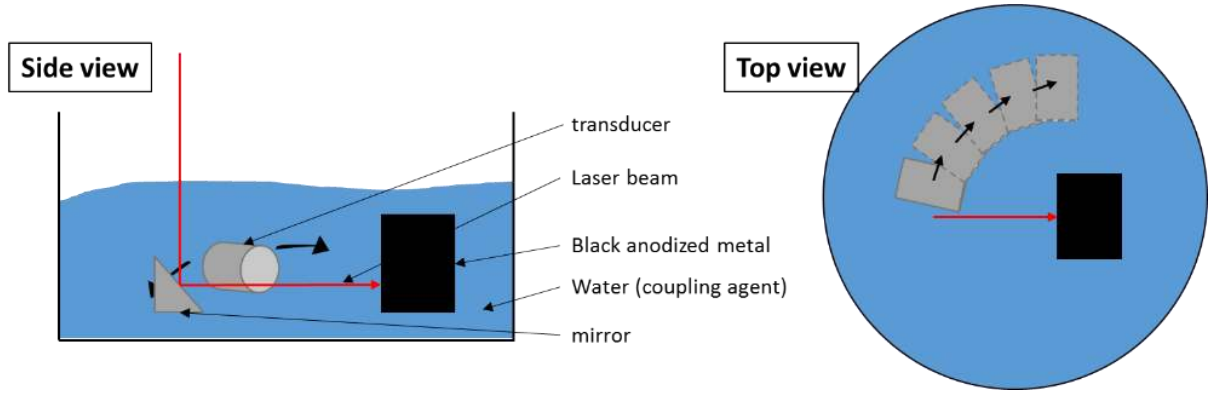

Figure A.1 Experimental set-up for the laser-transducer angle optimization. The transducer was positioned at five different angles at fixed distance from the metal sample.

Since the transducer head started to block the laser path-way at an angle below 20^0, the lowest laser-transducer angle tested was 20^0. As the laser-transducer angle varied from 20^o to 90^0, a magnitude of the correlation signal got smaller as shown in **Figure A.2**. Therefore, under the designed experimental set-up, smaller the angle between the laser beam and the transducer, stronger the SNR.

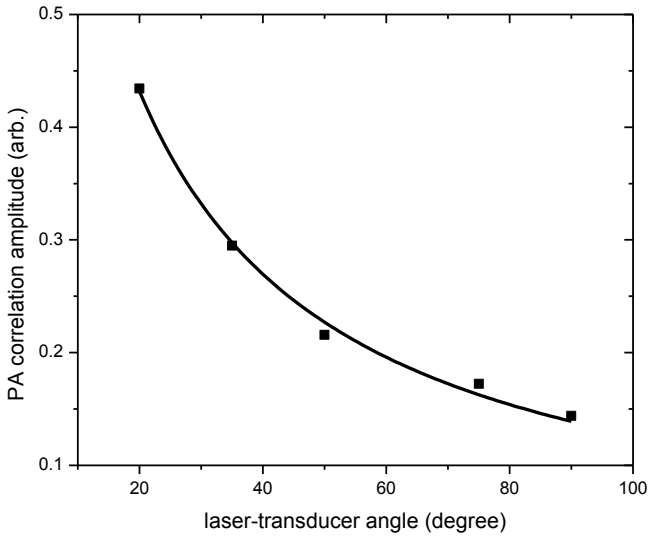

Figure A.2 A decrease in PA correlation amplitude as the laser-transducer angle increases from 20^o to 90^o.

Appendix 3

Molar extinction coefficient spectrum of adult sheep

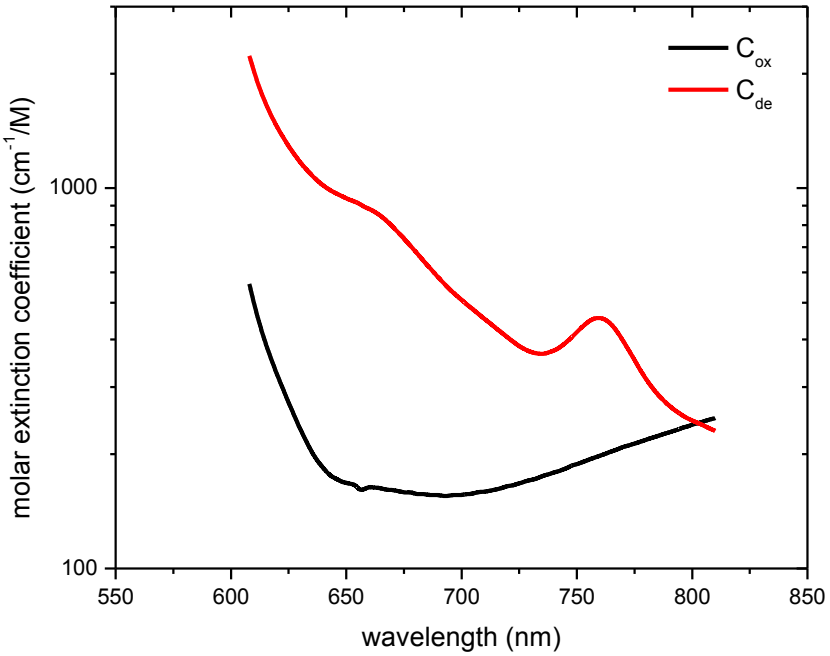

Figure A.3 Deoxy- and oxy-hemoglobin extinction coefficient spectrum of adult sheep; redrawn from data provided by [113]. Similarly to the human blood spectrum, the isosbestic point was observed near 800-nm region (~802-nm).